Cover Page

Report Title: Structure and Dynamics of Fuel Jets Injected into a High-Temperature Subsonic Crossflow: High-Data-Rate Laser Diagnostic Investigation under Steady and Oscillatory Conditions

Type of Report: Final Report

Reporting Period: 1 October 2011 – 30 Septemberer 2014

Principal Authors: Robert P. Lucht and William E. Anderson

Report Date: 23 January 2015

DOE Award Number: DE-FE0007099

Submitting Organization: Purdue University, West Lafayette, IN 47907

Disclaimer:
"This report was prepared as an account of work sponsored by an agency of the United States Government. Neither the United States Government nor any agency thereof, nor any of their employees, makes any warranty, express or implied, or assumes any legal liability or responsibility for the accuracy, completeness, or usefulness of any information, apparatus, product, or process disclosed, or represents that its use would not infringe privately owned rights. Reference herein to any specific commercial product, process, or service by trade name, trademark, manufacturer, or otherwise does not necessarily constitute or imply its endorsement, recommendation, or favoring by the United States Government or any agency thereof. The views and opinions of authors expressed herein do not necessarily state or reflect those of the United States Government or any agency thereof."

Abstract

An investigation of subsonic transverse jet injection into a subsonic vitiated crossflow is discussed. The reacting jet in crossflow (RJIC) system investigated as a means of secondary injection of fuel in a staged combustion system. The measurements were performed in test rigs featuring (a) a steady, swirling crossflow and (b) a crossflow with low swirl but significant oscillation in the pressure field and in the axial velocity. The rigs are referred to as the steady state rig and the instability rig. Rapid mixing and chemical reaction in the near field of the jet injection is desirable in this application. Temporally resolved velocity measurements within the wake of the reactive jets using 2D-PIV and OH-PLIF at a repetition rate of 5 kHz were performed on the RJIC flow field in a steady state water-cooled test rig. The reactive jets were injected through an extended nozzle into the crossflow which is located in the downstream of a low swirl burner (LSB) that produced the swirled, vitiated crossflow. Both H_2/N_2 and natural gas (NG)/air jets were investigated. OH-PLIF measurements along the jet trajectory show that the auto-ignition starts on the leeward side within the wake region of the jet flame. The measurements show that jet flame is stabilized in the wake of the jet and wake vortices play a significant role in this process. PIV and OH–PLIF measurements were performed at five measurement planes along the cross- section of the jet. The time resolved measurements provided significant information on the evolution of complex flow structures and highly transient features like, local extinction, re-ignition, vortex-flame interaction prevalent in a turbulent reacting flow. Nanosecond-laser-based, single-laser-shot coherent anti-Stokes Raman scattering (CARS) measurements of temperature and H_2 concentraiton were also performed.

The structure and dynamics of a reacting transverse jet injected into a vitiated oscillatory crossflow presents a unique opportunity for applying advanced experimental diagnostic techniques with increasing fidelity for the purposes of computational validation and model development. Numerical simulation of the reacting jet in crossflow is challenging because of the complex vortical structures in the flowfield and compounded by an unsteady crossflow. The resulting benchmark quality data set will include comprehensive, accurate measurements of mean and fluctuating components of velocity, pressure, and flame front location at high pressure and with crossflow conditions more representative of modern gas turbine engines.

A proven means for producing combustion dynamics is used for the performing combustion instability experimental study on a reacting jet in crossflow configuration. The method used to provide an unsteady flowfield into which the transverse jet is injected is a unique and novel approach that permits elevated temperature and pressure conditions. A model dump combustor is used to generate and sustain an acoustically oscillating vitiated flow that serves as the crossflow for transverse jet injection studies. A fully optically accessible combustor test section affords full access surrounding the point of jet injection. High speed 10 kHz planar measurements OH PLIF and high frequency 180 kHz wall pressure measurements are performed on the injected reacting transverse jet and surrounding flowfield, respectively, under simulated unstable conditions. The overlay of the jet velocity flowfield and the flame front will be investigated using simultaneous 10 kHz OH PLIF and PIV in experiments to be performed in the near future.

TABLE OF CONTENTS

PAGE

1. COVER PAGE.....1
   Disclaimer.....2
   Abstract.....3
   Table of Contents.....4
   List of Tables.....5
   List of Figures.....6
2. ACCOMPLISHMENTS.....13
3. PRODUCTS.....118
4. PARTICIPANTS.....119
5. IMPACT.....122
6. CHANGES/PROBLEMS.....124
7. SPECIAL REPORTING REQUIREMENTS.....124
8. BUDGETARY INFORMATION.....124

LIST OF TABLES

Table		Page
3.1	Operating conditions and all the flow parameters of RJICF used in the experiment.	16
3.2	Strouhal number, St_{wake} corresponding to the wake vortices frequency for all the test cases.	34
6.1	Nominal (mean) fixed conditions for the combustion dynamics study	70

LIST OF FIGURES

Figure		Page
2.1	Schematic of the staged combustion system test rig indicating the MCZ and optically accessible SCZ	13
2.2	Photograph of the modified window assembly installed in the test rig.	13
3.1	(a) Schematic diagram of the window assembly portion of the test rig with the extended nozzle showing the side view of the RJICF. The green horizontal lines indicate the PIV measurement planes. (b) The flow streamlines indicating the near field wake region of the RJICF along one of the x-y measurement planes.	17
3.2	A three dimensional CAD representation of the high repetition rate PIV system.	18
3.3	A sequence of background subtracted PIV images, in a measurement plane 5 mm from the nozzle exit plane, for the case of J =3 and ϕ_{jet} = 3. The images reveal that the swirling crossflow has a strong influence on the trajectory of the transverse jet, forcing it diagonally downwards in the image.	19
3.4	Comparing the crossflow velocity field measured at planes z = 5 mm, 10 mm, 15 mm, 35 mm, 45 mm and 50 mm. The velocity vectors are overlaid on top of velocity magnitude |V| (0 – 40 m/s). The direction of the velocity vectors observed the measurement planes shown confirms the strong swirling motion present in the crossflow.	21
3.5	Variation of the x- and y- components of velocity of the crossflow measured at planes z = 5 mm, 10 mm, 15 mm, 35 mm, 45 mm and 50 mm, plotted at x/d = 0.5 from the physical location of the center of the injector.(a) time averaged x-component of velocity, (b) time averaged y-component of velocity, (c) standard deviation of the x-component of velocity and (d) standard deviation of the y-component of velocity.	22
3.6	Variation of ω_z along the stream-wise direction indicating the effect of the momentum flux ratio on the magnitude of mean z-component of vorticity at z=5mm for all the non-reacting jet cases. The black dotted lines in the velocity contour plot show the corresponding axial locations.	24

3.7 Computed velocity vectors overlaid on top of x- velocity (row 1), V_x (-20 – 50 m/s), y- velocity (row 2), V_y (-20 – 30 m/s), c) z-vorticity (row 3), ω_z (-6000 – 6000 s^{-1}) and d) flow streamlines (row 4) colored by the velocity magnitude, |V| (0 – 50 m/s) for J = 3 and ϕ_{jet} = 3, measured at z=5 mm, 15 mm and 48 mm. 25

3.8 Streamwise variation of the velocity difference of the x-component of velocity (a) and y-component of velocity (b) obtained by subtracting the velocity field obtained by seeding the jet from the velocity field obtained by seeding the crossflow. 26

3.9 Instantaneous vector field of the non-reacting jet case, J =8, measured at z = 5mm showing the streaklines (left) and the corresponding vector field overlapped on z-vorticity magnitude (right)indicating the temporal evolution of the wake structure. 27

3.10 Instantaneous flow velocity vectors with background false colored by velocity magnitude of J=3 ϕ_{jet} = 3 at z = 5mm, showing the temporal evolution of the most dominant flow structures. 29

3.11 Instantaneous vector field with background false colored by z-vorticity (ω_z) of J=3 ϕ_{jet} = 3 at z = 5mm, to show the dynamics of the flow field. 30

3.12 Turbulent kinetic energy spectra plotted in wave number space for the reacting jet cases J = 3, ϕ_{jet} = 3 and J = 8, ϕ_{jet} = 3. 31

3.13 Turbulent kinetic energy spectra for the non-reacting jet case of J = 8 and the reacting jet cases of J = 8, ϕ_{jet} = 0.9 and ϕ_{jet} = 3, showing the effect of heat release on the flow field at measurement plane z = 5 mm. 32

3.14 The flow field at z= 5 mm for J =3 and ϕ_{jet} = 3, is divided into three regions, upper shear layer (USL) (Region 1), recirculation region (RR) (Region 2) and lower shear layer (LSL) (Region 3). 33

3.15 The power spectral density (PSD) of the fluctuating part of the x-component of velocity (V_x) for the three locations: (a) upper shear layer(USL) (location 1), (b) recirculation region (RR) (location 2) and (c) lower shear layer (LSL) (location 3). The plots indicates presence of a single peak frequency at f = 462 Hz. 33

3.16 Time averaged velocity vectors for reacting jet case of 40% H_2/60% N_2 J=8 measured at z = 10mm. The velocity vectors are overlaid on top of (a) x-velocity, V_x, (b) y-velocity, V_y, and (c) z-vorticity, ω_z, (d) time averaged streamlines colored by velocity magnitude. 36

3.17 Instantaneous velocity vectors for the reacting jet case of 40% H_2/60% N_2, J=8, measured at z = 10mm. The consecutive sequence of velocity vectors are 0.2 msec. The velocity vectors are overlaid on top of (a) x-component of velocity (V_x), (b) z-component of vorticity (ω_z) and (c) instantaneous flow streaklines colored by velocity magnitude. 37

3.18 Power spectral density (PSD) of the fluctuating part of the x-component of velocity (V_x) extracted from the recirculation region for the reacting jet case of 40% H_2/60% N_2 J=8, measured at z = 10 mm. The plot indicates presence of a single peak at a frequency, f = 410 Hz. 38

3.19 Phase averaged flow -streamlines for the reacting jet case of J=8; 40%H_2/60%N_2 case at z = 10mm. 38

4.1 Schematic of the windowed combustor with an extended nozzle. The region shaded with blue color indicates the location of the 283nm laser sheet for OH-PLIF measurements of the flame trajectory and the lines in green indicate the locations of 532nm and 283 nm laser sheet for both PIV and OH-PLIF measurements, respectively. 39

4.2 Time averaged normalized OH-PLIF intensity field for reacting jet cases of J=3 ϕ_{jet} = 3 and J=8 ϕ_{jet} = 3 measured at y = 0 mm, indicating the jet flame trajectory under the influence of swirling crossflow. 40

4.3 Consecutive sequence of single shot OH-PLIF images for the reacting jet case of J =3 ϕ_{jet} = 3, measured at plane y = 0 mm. 41

4.4 Consecutive sequence of single shot OH-PLIF images for the reacting jet case of J =8 ϕ_{jet} = 3, measured at plane y = 0 mm. 42

4.5 Instantaneous OH-PLIF intensity field overlaid on top of the flame front edge for the reacting jet case of J = 3, ϕ_{jet} = 3.0 at plane z = 5 mm. 43

4.6 OH PLIF single-shot images for the reacting jet case of 40% H_2/60% N_2, J=8 ameasured at the jet center plane (y = 0 mm). The sequence of images indicates the initiation of auto-ignition and temporal evolution of the flame front. 45

4.7 Consecutive sequence of OH PLIF images for the reacting jet case of J=8 40% H_2/60% N_2 measured at the jet center plane (y = 0 mm). 46

4.8 Consecutive sequence of OH-PLIF images for the reacting jet case of J =8 40% H2 and 60% N2 measured at plane y = 0 mm 47

4.9 Instantaneous OH PLIF images for the reacting jet case of 40% H_2 60% N_2 J =8 along the cross-section of the jet flame visualized at z = 10mm. The consecutive sequence of OH-PLIF images are 0.2 msec apart. 48

5.1 A three dimensional CAD schematic of the high repetition rate simultaneous PIV/OH-PLIF experimental system. 50

5.2 Photograph of test rig under operation, with the laser sheets going from top window of the combustor 50

5.3 Instantaneous sequence of (a) Reaction fronts overlaid on top of OH-PLIF images– time separation = 0.1 ms. (b) Reaction fronts overlaid against contours of x-velocity and velocity vectors, (c) Reaction fronts overlaid against contours of vorticity, for the reacting jet case of J = 3 ϕ_{jet}= 0.9 at z = 5 mm. 54

5.4 Instantaneous sequence of (a) Reaction fronts overlaid on top of OH-PLIF images– time separation = 0.1 ms. (b) Reaction fronts overlaid against contours of x-velocity and velocity vectors, (c) Reaction fronts overlaid against contours of y-velocity and velocity vectors. (d) Reaction fronts overlaid against contours of vorticity, for the reacting jet case of J = 8 40%H_2/60%N_2 at z = 10 mm. 57

6.1 Combustion dynamics combustor configurations. The transverse jet injection is near the fundamental (near 200 Hz) pressure node (Configuration A) and anti-node (Configuration B). 60

6.2 Cross sections of the optically accessible test section. Top: axial cross section. Bottom: transverse cross section. 61

6.3 OH PLIF optical setup surrounding the optically accessible test section. This setup is for the X-Z cross sections of the transverse jet. 62

6.4 OH PLIF optical setup surrounding the optically accessible test section. This setup is for the X-Y cross sections of the transverse jet. Beam path is denoted by blue arrows. 62

6.5 Optically accessible combustor test section on the test stand. From this perspective, the jet at the orifice exit is out of the page. This setup is for OH PLIF of the X-Z cross sections of the transverse jet. 63

6.6 Transverse jet injector assembly. 64

6.7 High frequency pressure transducer instrumentation port. 65

6.8 Spatial mode shapes for chamber 2L (top), 4L (middle) and 6L (bottom). Instantaneous (averaged) mode shapes are shown on the left (right). Dotted vertical lines represent configuration A and B jet injection locations. For data shown here, the 2L, 4L, and 6L acoustic modes correspond to 195 Hz, 389 Hz, and 579 Hz. X = 0 m represent the dump plane and X = 2.1 m is the chamber exit nozzle. 69

6.9 Dump combustor pressure trace for a typical test sequence for the reacting jet injected in an unsteady crossflow using the combustion dynamics rig configuration. 68

6.10 (a) Schematic diagram of the side view of the jet injection highlighting PLIF planes (purple) and window layout (blue). (b) Schematic diagram of top view of jet injection where the jet is coming out of the page. For both (a) and (b) the crossflow is from left to right. 70

6.11 Pressure phase locked with Figure 8 images, where red vertical lines demarcate the time period of the 16 frames in Figure 6.10. (a) Unfiltered pressure trace. (b) Bandpass filtered pressure at 195 Hz, where plot (c) shows a zoomed in view. (d) Detailed view showing location of Figure 6.11 frame relative to pressure signal. Pressure transducer is located in the crossflow 89 mm upstream of jet injection. 75

6.12 Sixteen consecutive 10 kHz OH PLIF images for plane z = 4.8 mm. The jet orifice is represented by the circle at (0,0), axes scaled by jet diameter, and the crossflow is left to right. 73

6.13 Plane Z = 4.8 mm showing every fourth image for a compression to rarefaction. These images preceed Figure 6.11 images and identified in the bandpass filtered pressure plot. 76

6.14 OH PLIF average at plane Z = 4.8 mm. 77

6.15 Dynamic mode decomposition power spectra for case A for 2000 consecutive frames. (a) Plot highlighting the absence of frequency content above 1 kHz. (b) Shows dominant frequency content present over the given period. 79

6.16 Bandpass filtered pressure at 195 Hz and 382 Hz for pressure transducers located in the crossflow 89 mm upstream of jet injection (a), inside the transverse injector (b), and at the exit nozzle of the combustion chamber (d). Plot (c) shows a PSD of the pressure at the 85 mm location upstream of the injector. 80

6.17 DMD spatial mode for 385 Hz corresponding to frames in Figure 6.11. 81

6.18 DMD spatial mode for 190 Hz corresponding to frames in Figure 6.11. 82

6.19 Bandpass filtered pressure near pressure anti-node of both 195 Hz and 382 Hz crossflow acoustic modes. Red vertical lines 79

demarcate the time period of frame 1 – 28 of Figure 6.16 and Figure 6.17. The pressure measurement is in the crossflow location 70 mm upstream of exit nozzle and square data points are only drawn on one curve for clarity.

6.20 Plane z = 14.8 mm unfiltered OH PLIF images. Every third image shown to capture a full period for the 194 Hz acoustic mode. 86

6.21 OH PLIF average at plane Z = 14.8 mm 84

6.22 (a) Bandpass filtered pressure at antinode of 194 Hz and 384 Hz acoustic pressure mode. Numbered data points correspond to Figure 6.20 frame numbers and are shown on 194 Hz data line only for clarity. (b) DMD power spectra for test case B. (c) Pressure PSD covering data in (a) and located at anti-node of both 194 Hz and 384 Hz. 84

6.23 Test case B DMD spatial mode for 194 Hz. The frame numbers correspond to those in Figure 6.22(a) and Figure 6.20. Every sixth image is shown to capture one period of the 194 Hz cycle. 87

6.24 Test case B DMD spatial mode for 194 Hz. The frame numbers correspond to those in Figure 6.22(a) and Figure 6.20. Every sixth image is shown to capture one period of the 194 Hz cycle. 88

6.25 Unfiltered OH PLIF images of the X-Z cross section. Every third image shown to capture a full period for the 194 Hz acoustic mode. 91

6.26 OH PLIF average for X-Z cross section. Rectangle at upper left represents injector orifice and is centered at (Z/D, X/D) = (0,0). Crossflow is from left to right. 92

6.27 . (a) Pressure PSD covering 2000 frame time duration for which DMD was applied. Pressure is located at anti-node of both 192 Hz and 387 Hz. (b) Bandpass filtered pressure at antinode of 194 Hz and 384 Hz acoustic pressure mode. Numbered data points correspond to Figure 6.26 frame numbers and are shown on 194 Hz data line only for clarity. (c) DMD power spectra for test case C 94

6.28 Test case C DMD spatial mode for 195 Hz. The frame numbers correspond to those in Figure 6.25 and Figure 6.27 (b). 95

6.29 Test case C DMD spatial mode for 365 Hz. The frame numbers correspond to those in Figure 6.25 and Figure 6.27 (b). 96

6.30 (a)-(d) Test case C DMD spatial mode for 455 Hz. The frame numbers correspond to those in Figure 6.25 and Figure 6.27 (b). (e) spectra of the pressure transducer inside the injector calculated for a 0.6 s duration. 97

7.1 Energy level diagram for the H2/N2 dual pump CARS system employed. 99

7.2 Schematic of the CARS laser system inside the laser lab. 100
7.3 Schematic of the CARS laser system inside the test cell. 101
7.4 Photograph of test rig under operation, with the pump, stokes and probe beams going through the window of the SCZ. 101
7.5 Comparison between experimental and theoretical dual-pump CARS spectra for various spatial positions with H_2 CARS signal present. 103
7.6 a) Average temperature contour plot and b) standard deviation in the measured temperature for the reacting jet case of J = 8;ϕ_{jet} = 0.9. 104
7.6 Temperature histograms extracted from the locations marked is circles on average temperature plots for reacting jet case of J=8;ϕ_{jet} = 0.9. 105
7.8 The streamwise variation of a) average temperature and b) temperature standard deviation extracted from the four y-locations for reacting jet case of J=8;ϕ_{jet} = 0.9. 106

2. ACCOMPLISHMENTS

The report details section will be organized along the lines of the tasks and subtasks listed in the PMP.

TASK 1.0: PROJECT MANAGEMENT AND PLANNING

SubTask 1.1: Initial Revision of Project Management Plan
This subtask has been completed and the milestone has been achieved. The PMP was delivered electronically to the NETL Federal Project Manager, Robin Ames.

SubTask 1.2: Quarterly Progress Reports
This is the fourth quarterly progress report.

SubTask 1.3: Final Progress Report
Completed.

TASK 2.0: DETAILED DESIGN AND FABRICATION OF RIG HARDWARE

SubTask 2.1: Complete Preliminary Design of Rig
This subtask has been completed. The necessary components for the modification of the test rig for the DOE RJIC studies have been designed and fabricated. The difference between the old configuration (Configuration 1) and the new configuration (Configuration 2) are shown in Fig. 1. The major difference between the two configurations is that the window dimensions are considerably larger: 98 mm wide x 73 mm high in the new test rig as compared to 63.5 mm wide x 38.1 mm high in the old test rig.

SubTask 2.2: Review Rig Design
This subtask has been completed. The design was reviewed internally at Purdue University and then was discussed during the kickoff Webex conference with NETL personnel on 15 November 2011.

SubTask 2.3: Detailed Design and Fabrication
This subtask has been completed.

SubTask 2.4: Staged Combustion Test Rig

2.4.1 Experimental System

The experimental test rig features a main combustion zone (MCZ) and a secondary combustion zone (SCZ). The MCZ features a low swirl burner (LSB) fueled with premixed natural gas and air. The low-swirl burner for the MCZ is similar to that reported in the literature (Cheng et al. 2000). The MCZ is operated at a pressure of 5.5 bar, an air inlet temperature of 723 K, an equivalence ratio of 0.5, and an air flow rate of 0.39 kg/s. A round-to-square cross section transition is added downstream of the MCZ. The SCZ is contained in a square-cross section assembly with optical access, as shown schematically in Fig. 2.1. The fuel injected transversely into the SCZ autoignites in the swirling vitiated crossflow from MCZ. The fuel is injected from a straight nozzle with an outer diameter of 17 mm and an inner diameter of 10 mm that extends 17 mm into the vitiated flow stream. The SCZ window assembly provides optical access from three sides. One window port is used for the fuel injection into the SCZ. Each window port features a two-window configuration. A thin inner window serves to contain the

flame gases and a thick outer window is used to contain the pressure. The combustor test rig is pressurized with the use of a butterfly valve at the exit of the test rig. The cavity between the inner and outer windows is pressurized by extracting a fraction of the inlet air from the location upstream of the main fuel injection and redirecting it into the cavity to match the 5.5 bar combustion pressure within the window combustor. The inner windows provide an optical viewing area of 100 mm by 73 mm. The window assembly has a square cross-section with dimensions of 107 mm by 107 mm. The design and operation of the test rig is described in detail in an earlier study (Lamont et al. 2012).

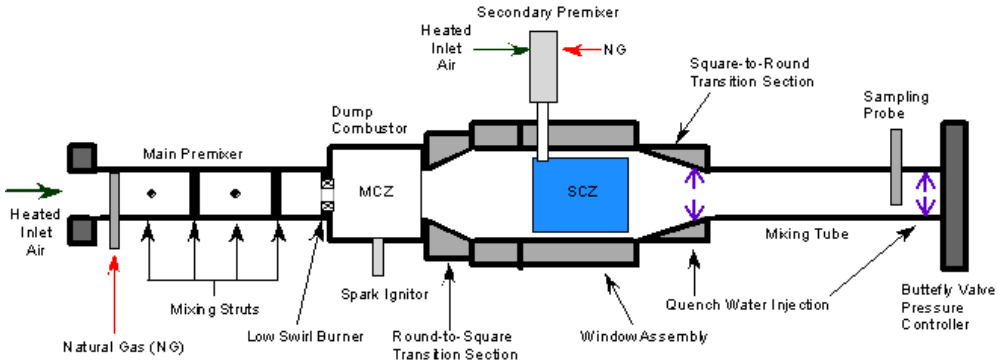

Figure 2.1 Schematic diagram of the staged combustion system test rig indicating the MCZ and optically accessible SCZ

The reacting jet fluid in our study was natural gas premixed with heated air. The fuel-air premixing for the SCZ was accomplished by injecting natural gas and heated secondary air into a mixing plenum. The air entering the mixing plenum was also heated to a temperature of 723 K. The flow rates were monitored in real time to ensure correct flow rates, incoming air temperature, and equivalence ratios. Data acquisition and experimental control was accomplished with LabView program. Figure 2.2 shows the photograph of the modified window combustor installed in the staged combustion test rig.

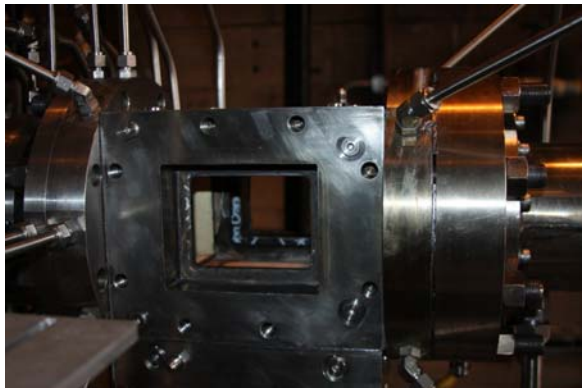

Figure 2.2 Photograph of the modified window assembly installed in the test rig.

TASK 3.0: HIGH-SPEED PIV STUDIES

In the present work, injection of a jet carrying premixed/non-premixed fuel into a high pressure vitiated crossflow is explored as a means of secondary injection. We investigate the role of a reactive jet in crossflow (JICF) to increase thermal efficiency by elevating the turbine inlet temperature with minimal contribution to NO_x formation. High-data-rate, laser-based diagnostics are used to study conditions representative of distributed combustion in modern gas turbine engines. The objective of the research is to obtain an insight into the fuel-air mixing leading to chemical reactions in a jet in crossflow configuration, and to acquire benchmark quality data sets which include comprehensive, accurate measurements of mean and fluctuating components of velocity, and flame structure visualization. Performing high repetition rate (HRR) laser diagnostics is challenging in the difficult environment of a high pressure gas turbine combustors. However, high-resolution spatial and temporal measurements of the turbulent flame structure under high pressure conditions provide significant insight into the complex processes of fuel/air mixing and turbulence-chemistry interactions. These measurements will be very helpful for designing high-efficiency, low-emission combustion systems and for providing high fidelity data for developing accurate turbulence-chemistry models.

A reacting jet in cross-flow (RJICF) configuration features transverse injection of reactive jet fluid into a vitiated cross-flow leading to mixing and chemical reactions. The jet in crossflow (JICF) is an important flow configuration due to its widespread application in energy and propulsion systems (Wooler 1969; Margason 1993). The flow-field associated with the JICF has superior mixing characteristics. The JICF entrains the ambient fluid at a much faster rate than a jet in co-flow. Many early studies on RJICF focused on developing empirical models for the jet trajectory (Gollahalli and Nanjundappa 1995; Huang and Chang 1994; Bandaru and Turns 2000; Hasselbrink and Mungal 2001; Su and Mungal 2004). Some of the recent experimental studies on the RJICF reported in the literature have focused on understanding the associated flow field and the flame structure (Hasselbrink and Mungal 2001; Sullivan et al. 2013; Sullivan et al. 2014; Lamont et al. 2012; Steinberg et al. 2013). With the commercial advent of high-repetition-rate (HRR) laser systems, it is now possible to perform non-intrusive temporally and spatially resolved measurements in reacting flows (Boxx et al. 2012, Boxx et al. 2013; Stohr et al. 2011). Researchers in the field of experimental turbulent combustion have reported HRR particle imaging velocimetry (PIV) based 2D and 3D velocity field measurements and OH-PLIF based flame front visualization. The ability of these techniques to track extremely transient events occurring in turbulent flames has contributed significantly to enhancing our understanding of the underlying physics of flow-flame interactions (Bohm et al. 2009).

In the past decade, PIV has evolved as one of the preeminent techniques to measure velocities in complex fluid systems, viz., high Mach number flow, boundary layer flow, reacting flow, etc., and has helped the development of a deeper insight into turbulence and fluid dynamics (Scarano and Poelma 2009; Westerweel et al. 2013). PIV measurements performed on a RJICF indicated that the flame centerline penetrates slightly further into the cross-flow as compared to an isothermal jet (Hasselbrink and Mungal 2001). It was reported that although the heat release rate alters the instantaneous velocity field, the reacting jet trajectory followed the trajectory of a non-reacting jet rather closely. In a recent study, simultaneous measurement of velocity, OH-PLIF and temperature fields for an auto-igniting jet of hydrogen fuel diluted with nitrogen (70%H_2 / 30% N_2) injected into a high temperature crossflow has been reported (Steinberg et al. 2013). In the study, for a range of jet momentum flux ratios, lifted jet flames with different lifted

branch configurations, viz., straight-edge lifted, merged lifted and hooked-edge lifted branch, were achieved.

A recent DNS study of an auto-igniting hydrogen jet injected into a high temperature crossflow reported that the mean velocity field preserves the most dominant flow feature of the JICF, the counter rotating vortex pair (CVP) (Chan et al. 2014). In another DNS-based study of a reacting JICF configuration, it was found that the flame stabilizes in a low velocity region between the large vortices of the CVP, where the mixture is near-stoichiometric (Grout et al. 2011; Kolla et al. 2012). In an LES-based numerical study on a swirling jet injected into an isothermal crossflow, the swirl number was observed to influence the CVP, in turn affecting the local vorticity and mean strain rate (Denev et al. 2009). It was observed that for higher swirl numbers, the CVP is inclined with respect to the mean crossflow streamlines, indicating a strong influence of the swirling motion. Most of these studies have focused on the role of CVP in flame stabilization in the far downstream, primarily due to the enhanced mixing efficiency offered by the CVP to a JICF.

A JICF flow field consists of several interesting vortical structures. The CVP is the most dominant flow structure. It has been established that the vorticity distortion within the evolving jet shear layer and the pressure difference between the windward and leeward sides of the jet lead to accumulation of vorticity sufficient to form the CVP downstream (Cortelezzi and Karagozian 2001; M'Closkey et al. 2002, New et al. 2006; Muppidi and Mahesh et al. 2007). The presence of this flow structure is responsible for imparting superior mixing far downstream of the jet. In addition to the CVP, flow structures associated with the JICF also include horseshoe vortices, shear layer loop vortices and upright wake vortices. In order to characterize the upright wake vortex dynamics, researchers have focused on wake-specific flow visualization, wake Strouhal number, and wake velocity deficit (Moussa et al. 1977; Fric and Roshko 1994). The wake vortices were reported to be similar to the Karman vortex street found in the wake field of a cylindrical bluff body (Fric and Roshko 1994). It has been reported that the wake Strouhal number varies between 0.07 – 0.15, indicating similarity between the dynamics of the wake field of the transverse jet and a solid cylinder ($St_{wake} = 0.2$ for $2000 < Re < 100000$). However, the source of vorticity in the case of the wake of the JICF is fundamentally different than that for the cylindrical bluff body. The vorticity within the wake region of a transverse jet depends on several important factors. The vortex tube generated within the walls of the extended nozzle is tilted and stretched by the crossflow towards the lee side of the jet resulting in the formation of the upright wake vortices. In addition to this, vorticity generated at the shear layer of the crossflow and jet fluid rolls up into periodically shed vortices. These two vortex sources mainly contribute towards the vorticity within the wake region of the jet. For reacting jets in crossflow, the flow field encounters sharp temperature gradients due to the heat release as a result of fuel-air combustion. This leads to local volumetric expansion in the flow field which causes vorticity generation in these regions of volumetric expansion. There is additional vorticity generation due to the density and dynamic pressure gradients encountered in these regions of heat release which is termed as baroclinic torque.

In this task, high repetition rate (HRR) PIV measurements are discussed. The measurements are used to characterize the wake field of an auto-igniting jet carrying fuel issuing into a swirling, vitiated crossflow at gas turbine relevant conditions. In the case of secondary injection of fuel in a gas turbine combustor, rapid mixing and chemical reaction in the near field of jet injection is desirable.

SubTask 3.1: Development of Test Matrix for Detailed Laser Diagnostic Investigations

In a previous work, a detailed parametric study on the staged combustion system (SCS) (Lamont 2012) was conducted to show the effect of the jet-to-crossflow momentum flux ratio (J), nozzle exit diameter (D) and jet equivalence ratio (ϕ_{jet}) on the pollutant emissions NO_x and CO etc. The fuel jets provide a net rise in temperature, ΔT across the SCZ. In the present study HRR laser diagnostic techniques are employed to characterize the structure and dynamics of the transverse jet interacting with a swirling and vitiated crossflow. A detailed test matrix is shown in Table. **3.1**3.1 for the PIV and OH-PLIF study discussed in this report.

Table. 3.1 Operating conditions and all the flow parameters of RJICF used in the experiment.

Cross Flow Operating Condition					
Operating Pressure (atm)			**5.5**		
Operating Temperature (K)			**723**		
MCZ Air Flow Rate (kg/s)			**0.39**		
MCZ Equivalence Ratio, ϕ_{main}			**0.5**		
Main Flow Reynolds Number(NR), Re_{main}			**105000**		
Main Flow Reynolds Number(R), Re_{main}			**61000**		
Non-Reacting Jet in Cross Flow					
High Temperature Air Jet	**Momentum Flux Ratio, J**	**Density Ratio, S**	**Jet Reynolds Number, Re_{jet}**		
	3	1	16900		
	8	1	27600		
RJICF Conditions					
FUEL JET	**Momentum Flux Ratio, J**	**Density Ratio, S**	**Jet Reynolds Number, Re_{jet}**	ϕ_{jet} =0.9	ϕ_{jet} = 3.0
Premixed Natural Gas	3	2.5	27500	**ΔT = 36 K**	**ΔT = 145 K**
	8	2.5	45000	**ΔT = 52 K**	**ΔT = 212 K**

The current study focuses on two momentum flux ratios, J=3 and J=8. The J =3 case corresponds to a lower momentum flux ratio where the premixed fuel reacts closer to the nozzle exit, with the reaction zone stabilized within the wake of the jet. The J=8 case allows the jet fluid to penetrate deeper into the crossflow with a higher degree of mixing. The jet equivalence ratios of ϕ_{jet} = 0.9 and 3 are chosen in order to study leaner and richer jet flame cases that provide different changes in temperature across the SCZ. The jet to crossflow density ratios (S) for the non-reacting jet cases and the RJICF cases were 1 and 2.5, respectively. Velocity measurements were performed at 5 planes along the cross-section of the jet, as shown in Fig. 3.1a, z = 5 mm (1), 15 mm (2), 25 mm (3), 35 mm (4) and 45 mm (5) away from nozzle exit plane. Here z represents the distance from the nozzle exit plane. The nozzle exit plane is considered as the origin for this geometry as shown by the coordinate axes in Figure a and 3b. The horizontal green lines indicate the locations of laser sheet and the view shown in the schematic is defined as the side view of the jet in the x-z plane. The flow streamlines indicating the near wake region of the jet are shown in Fig. 3.1b highlight the overall feature of the flow field under consideration.

The shear layer between the crossflow and the jet is represented by the black dotted lines and the region outside the shear layer is termed as outer wake region. The PIV measurements were performed along x-y plane which is perpendicular to the jet axis. Henceforth, the x-z planes will be referred as the planes parallel to the jet trajectory and the x-y plane will be referred as jet cross-section planes. Note that PIV measurements were not successful on planes parallel to the jet trajectory due to high scattering when the laser sheet impinges on the TBC-coated combustor wall, saturating the camera pixels. In order to isolate the effect of heat release on the flow field, non-reacting flow PIV measurements were performed. The fluid for the non-reacting flow field was heated air flowing through the main and secondary combustion zone without any fuel. The density ratio (S) of the jet to the crossflow fluid was 1.0. Multi plane velocity measurements on non-reacting jets were performed for 4 different J values, J = 3, 4, 6 and 8.

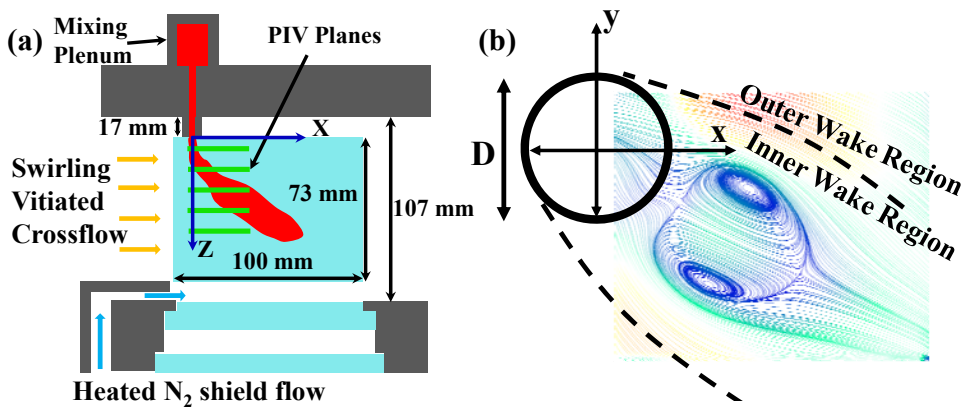

Figure 3.1 (a) Schematic diagram of the window assembly portion of the test rig with the extended nozzle showing the side view of the RJICF. The green horizontal lines indicate the PIV measurement planes. (b) The flow streamlines indicating the near field wake region of the RJICF along one of the x-y measurement planes.

SubTask 3.2: Development of Seeding, Data Acquisition, and Data Analysis Techniques for High-Speed PIV Measurements in High-Pressure Combustion Test Rigs

The PIV system consists of a high repetition rate, dual cavity, diode-pumped solid state Nd:YAG laser (Edgewave – IS8IIDZ) and a high speed CMOS camera (Photron-FASTCAM SA4), as shown in Fig 3.2. The pulse energy for each cavity is 6 mJ/pulse at 5 kHz and 532 nm. The laser beam is focused using a 1000 mm focal length positive spherical lens, a cylindrical lens of -50 mm focal length and finally a 250 mm cylindrical lens to form a laser sheet that is 35 mm wide and 650 µm thick. The time delay between the two laser pulses was optimized to 15 µsec for the reacting flow case and 20 µsec for the non-reacting flow case in order to account for non-uniform velocity gradients as well as to minimize the influence of the out of plane velocity component of the jet. The flow field was seeded with TiO_2 particles with nominal diameter of 250 nm. The scattered light from the particles was collected using a 105 mm Nikon lens. The test rig has two locations to seed the flow field, i) upstream of the LSB and ii) along with the jet. The PIV imaging was performed using the LaVision high speed controller and software package (LaVision 8.1.4) to control the Photron Camera. The high speed controller was synchronized to an external function generator (Quantum Composer 9520 Digital Delay Pulse Generator) that

provided the input signal and necessary time delays to the laser system, including the time delay between the two laser pulses. A 3D dot target was used to calibrate the PIV images. Calibration was always performed just before the start of the experiment.

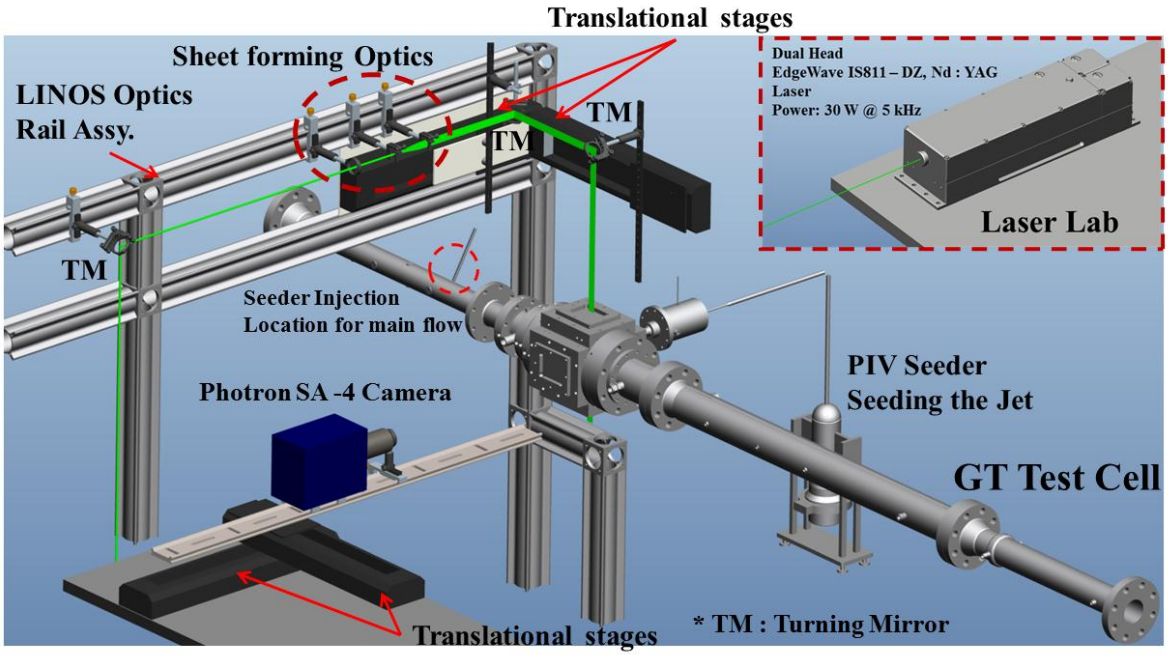

Figure 3.2 A three dimensional CAD representation of the high repetition rate PIV system.

Ideally, the seeding for PIV measurements should be homogeneous in order to ensure minimal vector rejection and high correlation values. Due to the presence of non-uniform temperature and density gradients in turbulent flames, PIV measurements in these flow-fields suffer from non-uniform seeding density. Another issue with PIV measurements in high temperature and high pressure flows similar to those studied here is that the optical windows became coated with the seeding particles during testing. At high temperatures the quartz windows soften and seed particles stick to them. This limits the amount of data that can be acquired in a single experimental run.

2.5 PIV Velocity Vector Processing

The velocity vector fields were computed from the particle image pair spatial cross-correlation using the LaVision 8.1.4 software package for 2D PIV. A rigorous PIV process optimization, based on the particle density, time delay between the two laser pulses and vector computation technique, was performed to maximize the correlation values for the computed vector field. A multi-pass vector evaluation technique featuring an auto-adaptive interrogation window with a first pass window size of 64X64 and a second pass window size of 16X16 pixels with 50% overlap between the image pairs was utilized for computing the vector field. Because the jet was being seeded for the PIV measurements the particle seed was present only in the region where the jet was present. Thus, for the purpose of velocity vector computation, the remaining regions without any particles were masked. The field of view utilized to perform the cross correlation was 35 mm x 55 mm, with a vector resolution of 0.8 mm x 0.8 mm. Based on

these parameters the total number of rejected vectors varied between 15 – 25 %. The signal to noise ratio was always maintained greater than 1.2. A total of 3777 image pairs were captured at each plane. This corresponded to a data acquisition time of 0.755 secs.

SubTask 3.3: High-Speed PIV Measurements for Natural Gas Jets Injected Into Vitiated and Nonvitiated Crossflows

Time-resolved velocity measurements in the current study provide significant insight into the flow physics describing the influence of flow variables on the jet flame. The flow-field in this study features the interaction between a swirling vitiated crossflow and a fuel carrying transverse reacting jet. The raw PIV images, shown in Fig 3.3, indicate a strong influence of the swirling cross-flow on the jet at x-y plane z = 5 mm which is closest to the nozzle exit. The background subtracted images also show fine scale flow structures in the instantaneous sequence of images. The non-uniformity of particle seeding in these images as the two fluid streams mix is clearly evident.

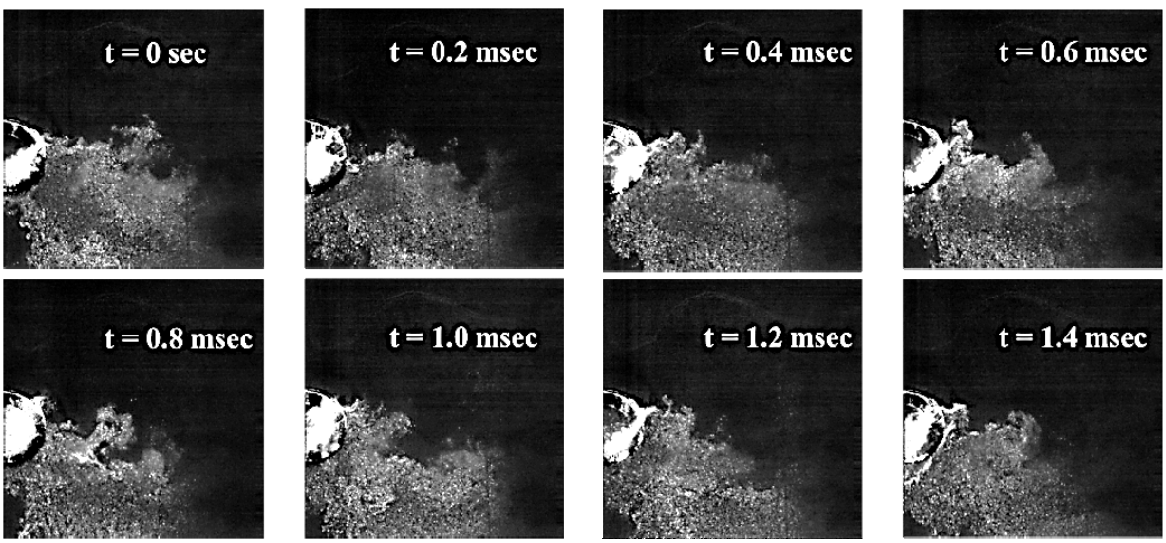

Figure 3.3 A sequence of background subtracted PIV images, in a measurement plane 5 mm from the nozzle exit plane, for the case of J =3 and ϕ_{jet} = 3. The images reveal that the swirling crossflow has a strong influence on the trajectory of the transverse jet, forcing it diagonally downwards in the image.

3.3.1 Time Averaged Flow Field

Velocity data were collected for a duration of 0.755 sec at a repetition rate of 5 kHz. A total of 3777 particle image pairs were collected, providing enough sampling time to extract reasonable time-averaged fields. In order to fully characterize the flow field, three different PIV measurements were performed. We performed (i) PIV measurements of the vitiated crossflow to quantify the velocity of the crossflow fluid stream, (ii) PIV measurements for non-reacting jets, and (iii) for the reacting jet cases. For all the three tests the locations of the measurement planes were the same. The time averaged velocity fields obtained from these studies are discussed in this section.

PIV Measurements of the Crossflow

Two component PIV measurements were performed for characterizing the velocity field of the incoming vitiated crossflow. These measurements will provide valuable information on the boundary conditions for numerical simulation of the JICF and RJICF experiments. For these experiments, the jet injector face was removed and replaced with a planar metallic blank. Multi plane PIV measurements were performed to characterize the swirling motion of the crossflow. The velocity vectors computed at measurement planes z = 5, 10, 15, 35, 45 and 50 mm are shown in Fig.3.4. The velocity vectors are overlaid on top of a false color map of velocity magnitude. The velocity magnitude is found to be mostly constant across all the measurement planes except at the center of the combustor (z = 35 mm). This is probably due to the velocity deficit at the center of the LSB. The directions of the velocity vectors in the planes z = 5, 10 and 15 mm are towards the bottom corner of the image and that in the planes z = 45 and 50 mm are towards the top corner of the image, which shows the direction of swirling motion of the crossflow. At the center of the combustor the velocity vectors are nearly parallel to the x-axis. The spanwise variation of the mean and standard deviation of x- and y-components of the velocity field at x/d = 0.5, is shown in Fig. 3.5. The x-component of velocity is seen to be higher than the mean magnitude of velocity between y = -15 and -5 mm in the planes z = 45 mm and 50 mm. The y-component of velocity, as shown in Fig. 3.5b is negative for the planes z = 5, 10 and 15 mm, positive for the planes z = 45 and 50 mm and is approximately zero for z = 35 mm plane. The y-velocity trend clearly shows the behavior of the swirling crossflow. The standard deviations in the measured values of x and y components of velocity lie in the range of 7 – 15 m/s across all the planes, as shown in Fig. 3.5c and d.

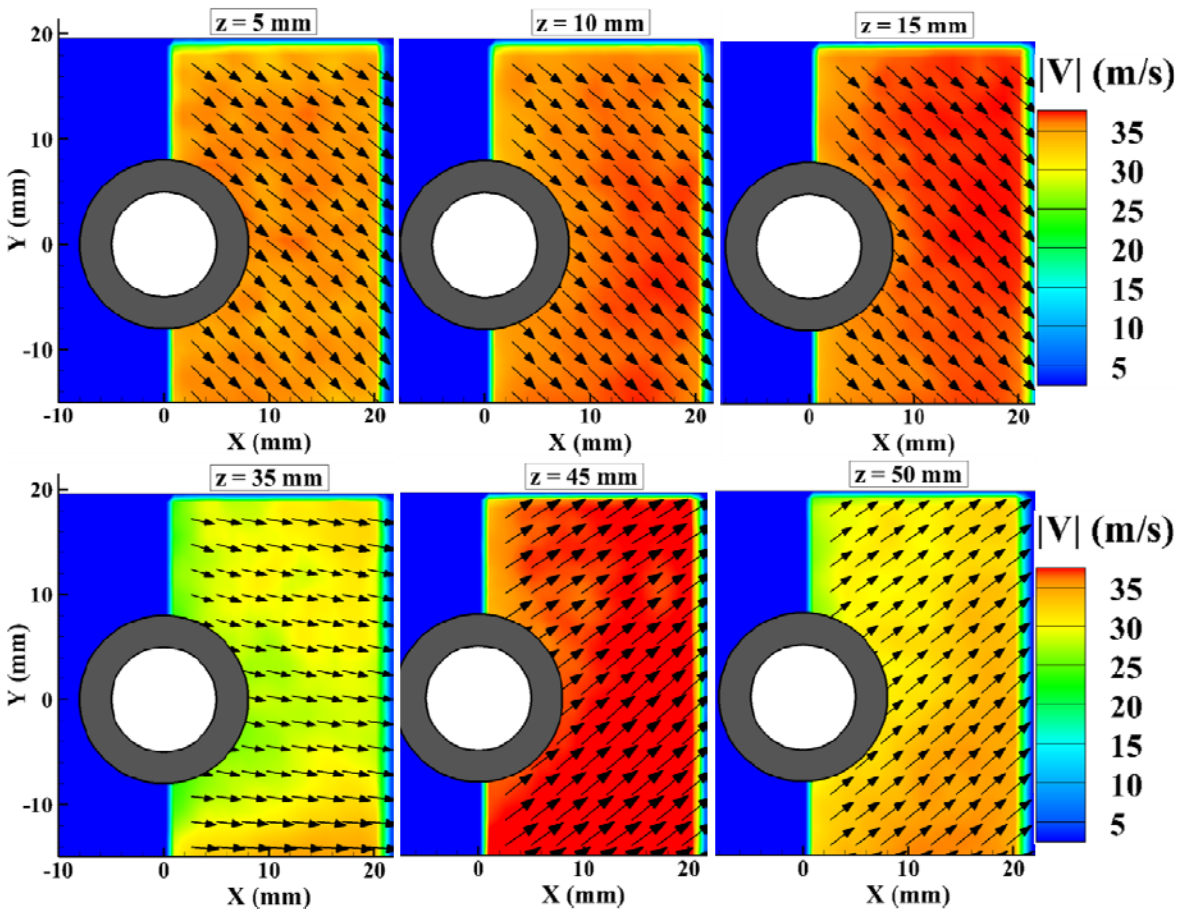

Figure 3.4 Comparing the crossflow velocity field measured at planes z = 5 mm, 10 mm, 15 mm, 35 mm, 45 mm and 50 mm. The velocity vectors are overlaid on top of velocity magnitude |V| (0 – 40 m/s). The direction of the velocity vectors observed the measurement planes shown confirms the strong swirling motion present in the crossflow.

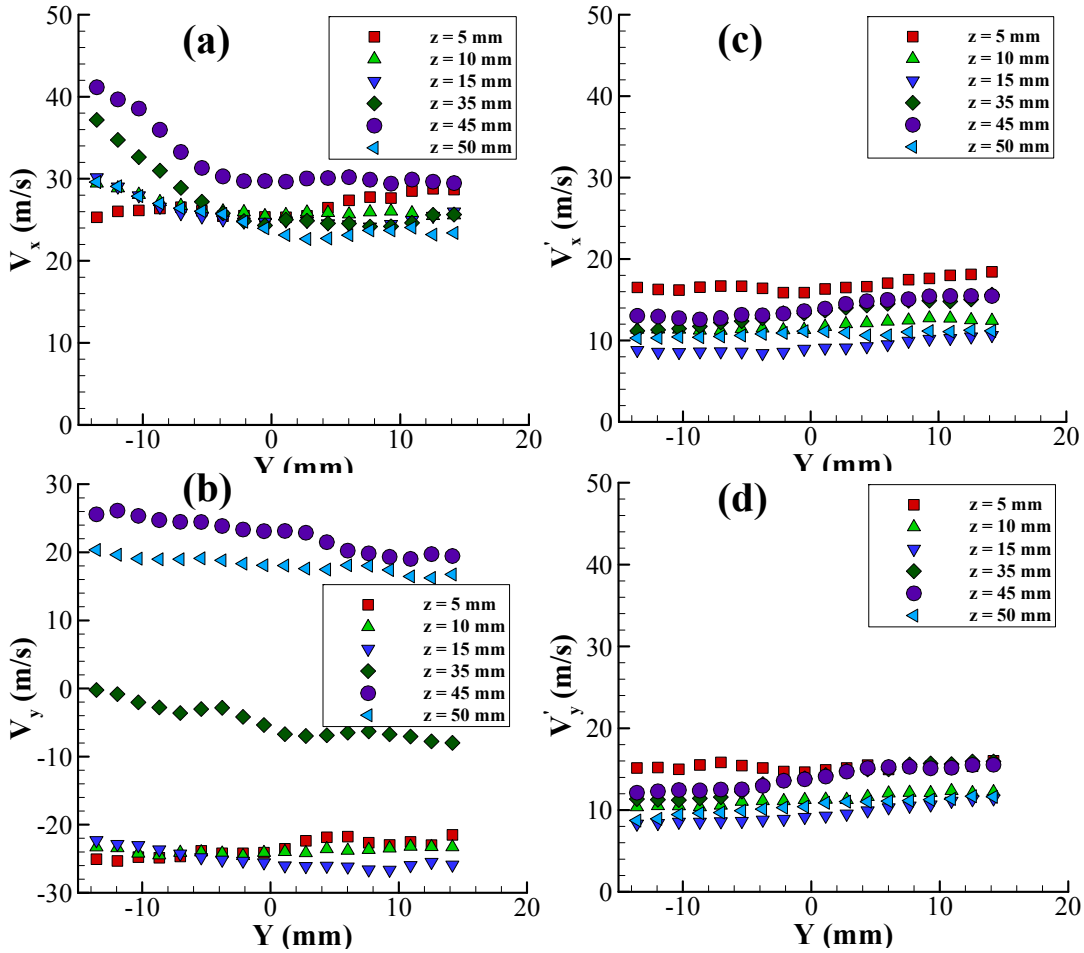

Figure 3.5 Variation of the x- and y- components of velocity of the crossflow measured at planes z = 5 mm, 10 mm, 15 mm, 35 mm, 45 mm and 50 mm, plotted at x/d = 0.5 from the physical location of the center of the injector.(a) time averaged x-component of velocity, (b) time averaged y-component of velocity, (c) standard deviation of the x-component of velocity and (d) standard deviation of the y-component of velocity.

Non-Reacting Flow Field of JICF

The time-averaged flow fields for the non-reacting jet cases (Fig.3.6) show that an increase in jet momentum flux ratio results in an increase in the out-of-plane vorticity magnitude, (ω_z). The vorticity magnitude is extracted from 4 locations along the x-direction (x/d = 0.5, 1.0, 1.5 and -2.0) along the black dotted lines shown in the vorticity contour plots. The velocity vector fields shown in Fig 3.6 were measured at z = 5 mm. The results indicate that for a higher momentum flux ratio, the rate of mixing of the jet fluid with the crossflow fluid will be higher.

Reacting Flow Field of RJICF

The velocity fields measured for the reacting jet case of J = 3 and ϕ_{jet}= 3 at planes z = 5 mm, 15 mm and 48 mm are shown in Fig 3.7a. The mean velocity vectors are overlaid on a false color map of the x-component of velocity contour. For the velocity vectors measured at z = 5 mm the vectors in most regions are pointed towards the bottom corner of the image. The nozzle

exit, represented by the concentric circles centered at x = 0 mm, y = 0 mm, has been included to indicate the vector direction with respect to the nozzle location. The jet fluid interacts with the incoming crossflow by forming the shear layer that surrounds the wake of the jet. Within the two shear layers there are two distinct high speed regions. A strong recirculation region is evident between the two high speed flow regions at z = 5 mm. The recirculation region is a characteristic feature of the wake of the jet. The wake vorticity entrains the jet fluid and the crossflow fluid within the wake of the jet, leading to chemical reactions and stabilization of a reaction zone. Fig 3.7b shows the same vector field overlaid on a false color map of the y-component of velocity. A strong negative y-velocity field is present except for the region where the flow is recirculating. Fig 3.7c shows the velocity vectors overlaid on a false color map of the z-component of vorticity (ω_z). A steady counter-rotating wake structure aligned in the direction of the mean velocity vectors is clearly evident at z = 5 mm. These wake structures are steady and well defined and are similar to the wake structure behind a cylindrical bluff body. A detailed analysis involving time resolved dynamics of the wake of the jet is discussed in a subsequent section. The flow field at z = 15 mm is similar to that at z = 5 mm in terms of the direction of the velocity vectors. However, the flow field observed at z = 15 mm shows a significant decrease in the magnitude of the out of plane vorticity (ω_z). At z = 15 mm the measurement plane is no longer located within the wake of the jet resulting in a weaker wake vorticity, and the recirculation region is absent as well. The directions of the velocity vectors computed at z = 45 mm indicate that the flow field is moving towards the top corner of the image. The y-component of the velocity field shows positive values for this plane. This is a clear indication of the effect of swirling crossflow, which tends to push the jet fluid in the negative y direction near the nozzle exit plane, and in the positive y direction towards the opposite wall. The time averaged flow streamlines shown in Fig 3.7d provide a different visualization of the wake vortical structure at z = 5 mm. Two counter-rotating structures are located between x = 5 and 22.5 mm and y = -2.5 and -20 mm. The structures are surrounded by the two high speed shear layers. No distinct flow structures are evident at planes z = 15 mm and 45 mm, indicating that the wake vortices are shorter than z = 15 mm. At the center plane of the combustor the velocity vectors are parallel to the x-direction with negligible y-velocity. A similar trend for the velocity field is observed for the case J = 3 and ϕ_{jet} = 0.9 for all the measurement planes. When the momentum flux ratio is increased to J = 8 the velocity field measured at z = 5 mm is found to be similar to that of J = 3 cases. A steady wake structure is captured for all the cases at this plane. However, at z = 15 mm the wake vortex structure is still well characterized for the J=8 cases, unlike the J=3 cases. This is because for higher values of momentum flux ratio the jet penetrates deeper into the crossflow, resulting in larger wake fields and longer upright wake structures.

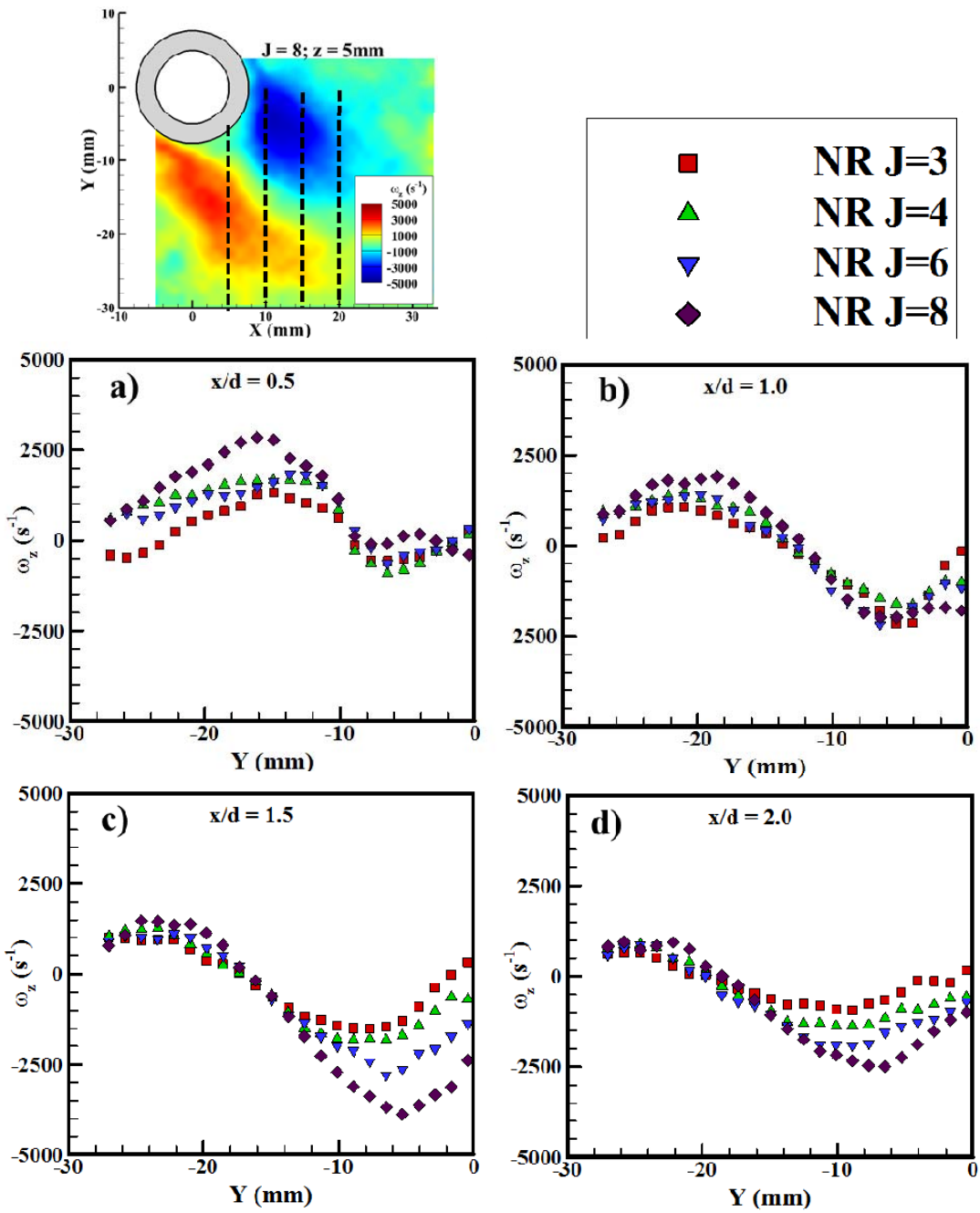

Figure 3.6 Variation of ω_z along the stream-wise direction indicating the effect of the momentum flux ratio on the magnitude of mean z-component of vorticity at z=5mm for all the non-reacting jet cases. The black dotted lines in the velocity contour plot show the corresponding axial locations.

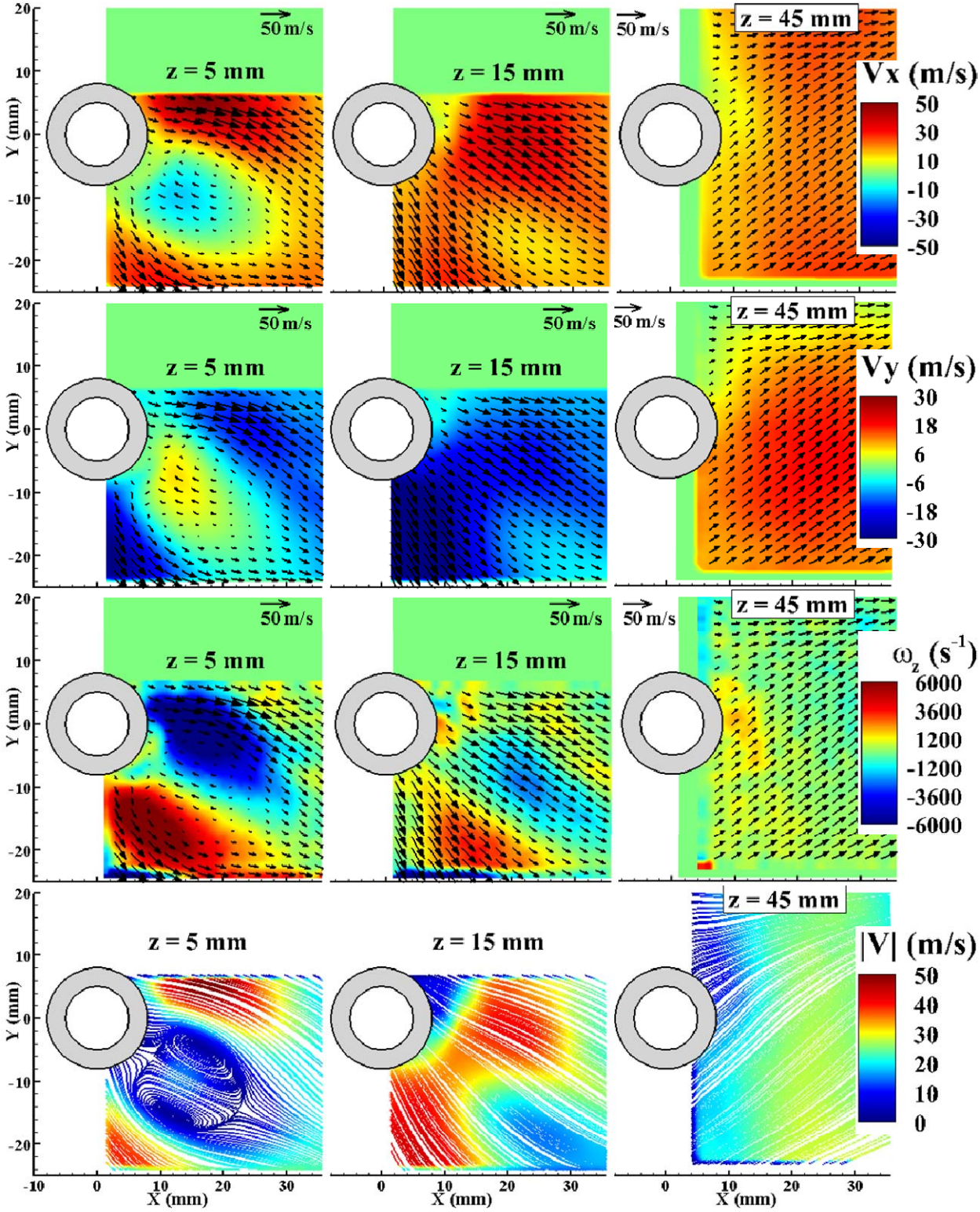

Figure 3.7 Computed velocity vectors overlaid on top of x- velocity (row 1), V_x (-20 – 50 m/s), y- velocity (row 2), V_y (-20 – 30 m/s), c) z-vorticity (row 3), ω_z (-6000 – 6000 s^{-1}) and d) flow streamlines (row 4) colored by the velocity magnitude, |V| (0 – 50 m/s) for J = 3 and ϕ_{jet} = 3, measured at z=5 mm, 15 mm and 48 mm.

As mentioned earlier for the PIV measurements, the flow field was seeded through the jet. Seeding the flow field by injecting the particles through the jet leads to some bias in the magnitude of the velocity field measured. Injecting the PIV seed particles into the crossflow was challenging due to two main reasons. Firstly, due to the swirling motion, seeding the crossflow resulted in much faster coating of the windows as compared to seeding only the jet. To maximize the amount of data collected on a single test day, seeding the jet was preferred over seeding the crossflow. Secondly, the crossflow seeded experiments could not capture the wake structure due to the lack of particles entrained in the wake region, which is an important flow structure for the current study. In order to quantify this bias some PIV measurements were performed by seeding the crossflow. Figure 3.8 shows the streamwise variation of the velocity difference between the flow field obtained by seeding the crossflow and seeding the jet for reacting jet case of J = 3 and ϕ_{jet} = 3 at z = 5 mm.

$$\delta V_i = V_i^{CF} - V_i^{JET} \; (i = x, y) \qquad \text{Eq.1}$$

Here, the velocity field is extracted from a region x = 0 mm – 15 mm and y = -10 mm - -25 mm. It is observed that the x-component of velocity is approximately 10 – 15 m/s higher for the crossflow seeded case. At x = 10 mm and 15 mm the y-component of velocity is higher for the jet seeded case and this is mainly due to the lack of particles within the wake of the jet for the crossflow seeded case. Due to this reason the wake structure and the recirculation region could not be captured by seeding the crossflow. Thus, these observations confirm that there is a bias in the velocity magnitude when seeding the jet versus the crossflow and the velocity data needs to be carefully interpreted. However, as the focus of the current study is characterizing the structure and dynamics of the wake vorticity, henceforth, all the discussions are based on the velocity fields obtained by seeding the jet.

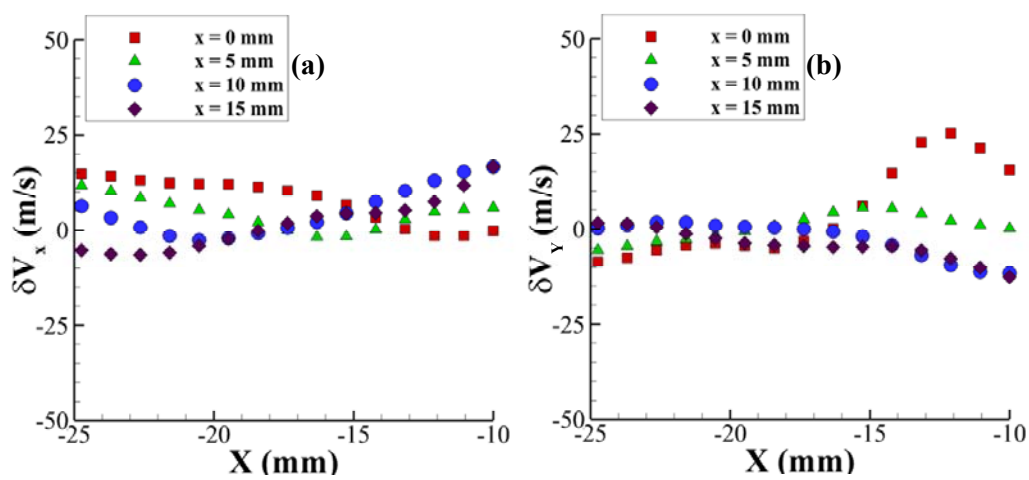

Figure 3.8 Streamwise variation of the velocity difference of the x-component of velocity (a) and y-component of velocity (b) obtained by subtracting the velocity field obtained by seeding the jet from the velocity field obtained by seeding the crossflow.

3.3.2 Instantaneous Flow Field

Flame structure visualization using 10 kHz OH-PLIF shows a steady reaction zone within the wake of the jet, discussed in section 3.5. This can be attributed to the wake vorticity entraining fuel air mixtures and reaction products within the wake of the jet stabilizing the reaction zone. This observation demands a detailed understanding of the dynamics of the wake structure is therefore very important. The velocity measurements at 5 kHz discussed in this section successfully provide time-resolved information on the transient wake structure of the reacting jet.

Non-Reacting Flow Field

A sequence of instantaneous velocity streaklines and corresponding vector fields overlaid on top of the ω_z magnitude is shown in Fig.3.9 for the non-reacting J = 8 jet case for the z = 5 mm measurement plane. It can be seen that at time t = 0.2 msec, a single vortex structure near the upper shear layer (USL) is captured. At time t = 0.4 msec the lower vortex structure appears near the lower shear layer and an asymmetric counter-rotating wake structure is captured. The flow structure is oriented along the direction of mean flow and the two counter-rotating structures move away from each other indicating in-plane motion of the jet. The detected flow structure exhibits strong vorticity. The two main sources of vorticity for this flow field are the mixing layer between the jet and crossflow fluid, and from within the nozzle inner wall boundary layer. The sequence of velocity vectors shows that the vorticity originates near the nozzle and eventually sheds off in the inner wake region further downstream of the nozzle. Thus, the non-reacting jet case provides important insight into the dynamics of the dominant wake structure showing the presence of periodic asymmetric vortex structures similar to those observed behind a cylindrical bluff body in a crossflow.

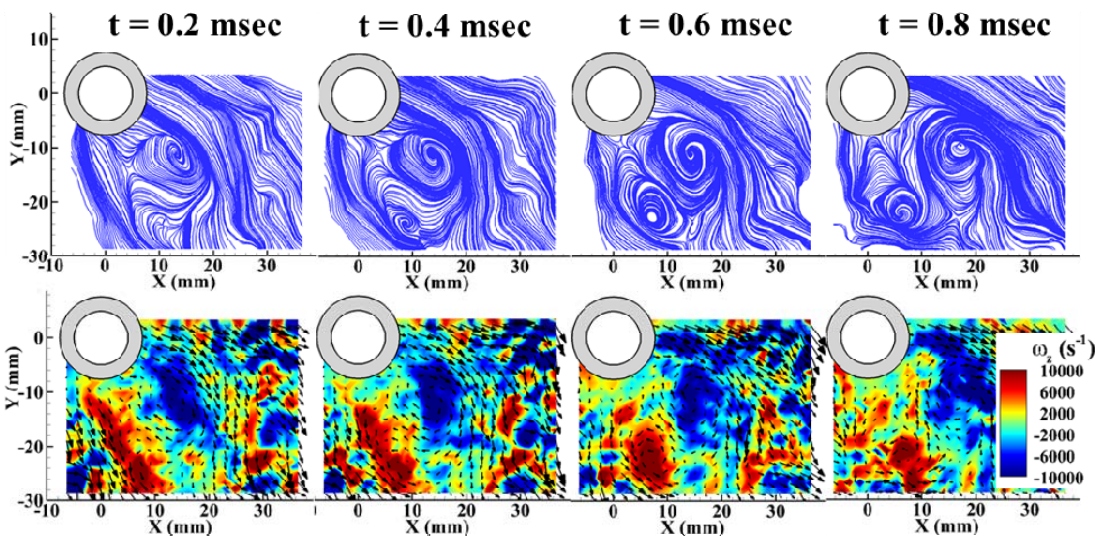

Figure 3.9 Instantaneous vector field of the non-reacting jet case, J =8, measured at z = 5mm showing the streaklines (left) and the corresponding vector field overlapped on z-vorticity magnitude (right)indicating the temporal evolution of the wake structure.

Reacting Flow Field

A sequence of instantaneous velocity vectors overlaid on top of a false color map of the velocity magnitude for the J = 3, ϕ_{jet} = 3 reacting jet case for the z = 5mm plane is shown in Fig. 3.10. The velocity magnitude clearly shows that the flow field comprises of three main regions, the upper and lower high speed regions and the inner recirculation region. The counter-rotating wake structure is surrounded within the high speed region creating an inner recirculation region. The sequence of images shows interesting fluid behavior in the wake of the jet. At time t = 0.2 msec, the crossflow seems to be closing around the jet resulting in a small wake region. This behavior of the wake changes from time t = 0.4 msec to time t = 16 msec where the wake of the jet is more open and has a much larger recirculation region, a phenomena similar to the wake of a bluff body. However, it has already been shown, by (Fric and Roshko 1994) and several other researchers, that there is a significant difference between the mechanism of vorticity formation in the wake of a transverse jet as compared to that of a cylindrical bluff body. The velocity vectors show that the upright wake vortices do not necessarily appear in counter-rotating pairs. Unlike the Karman vortex street, the instantaneous flow structures are quite disordered in appearance. Figure 3.11 shows the same sequence of flow fields with velocity vectors overlaid on top of the out of plane component of vorticity. The most noticeable observation is that the vorticity magnitude for the reacting jet case is found to be twice as much as observed for the non-reacting jet, which suggests that local heat release and density gradient add to the vorticity strength and create a stronger recirculation region. Similar to the non-reacting flow cases, the vorticity originates near the nozzle and convects downstream along the direction of the mean flow.

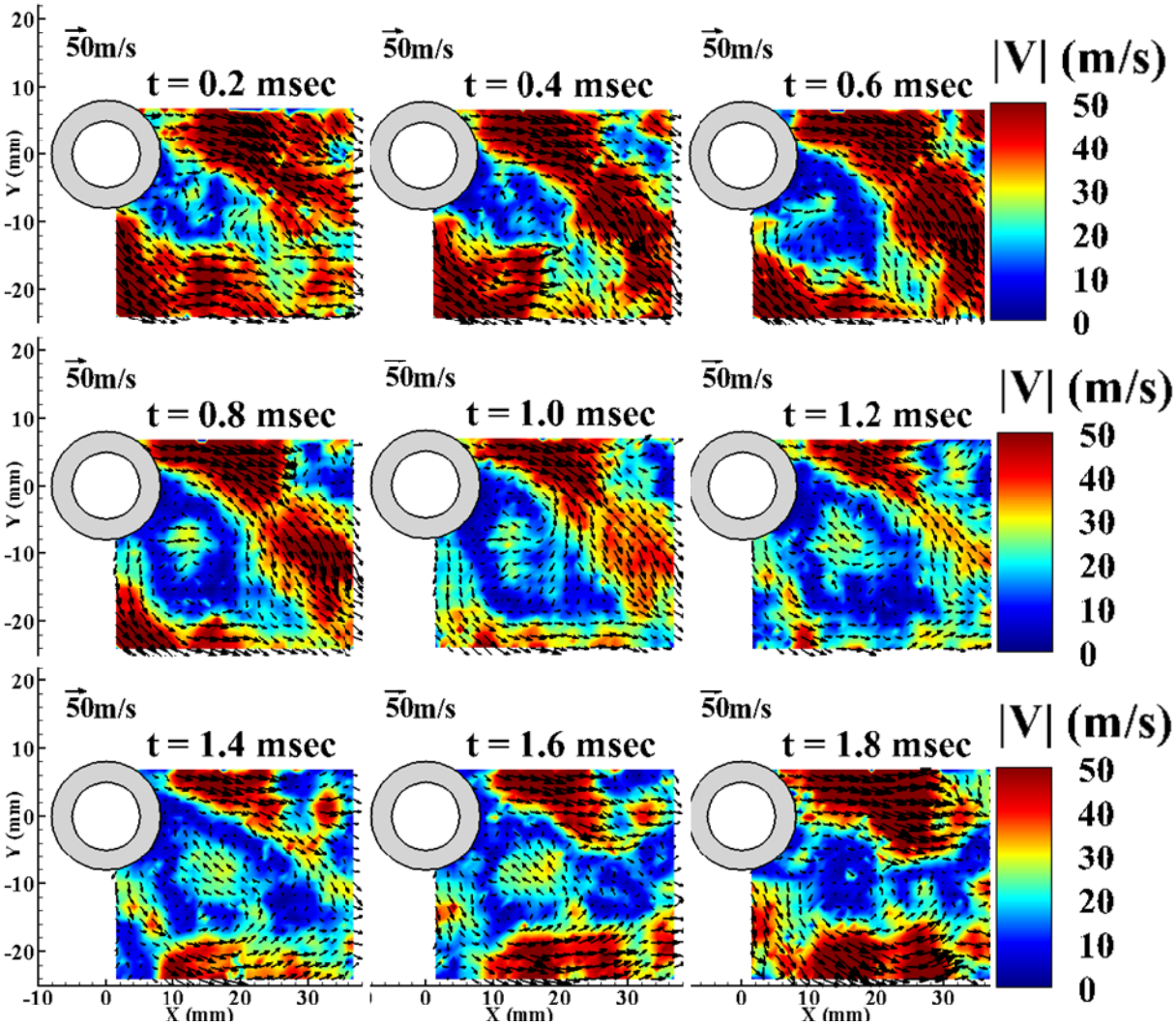

Figure 3.10 Instantaneous flow velocity vectors with background false colored by velocity magnitude of J=3 ϕ_{jet} = 3 at z = 5mm, showing the temporal evolution of the most dominant flow structures.

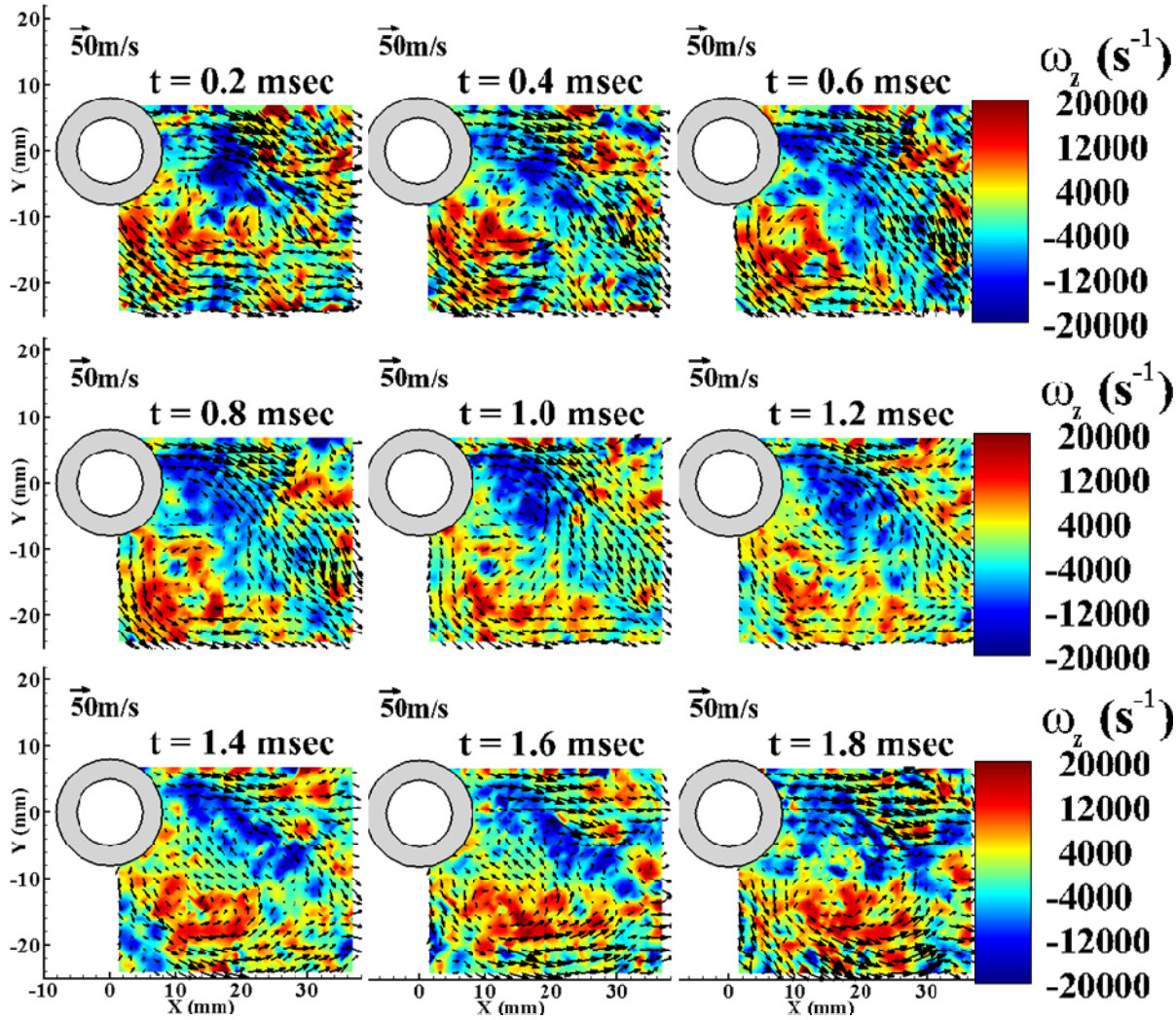

Figure 3.11 Instantaneous vector field with background false colored by z-vorticity (ω_z) of J=3 ϕ_{jet} = 3 at z = 5mm, to show the dynamics of the flow field.

3.3.3 Turbulent Kinetic Energy Spectra and Wake Dynamics

The turbulent kinetic energy (TKE) spectra, E(k), is plotted in the wavenumber space, k, for the reacting and non-reacting jets to understand the contribution of the dominant wake structure to the TKE within the wake region of the jet. Here the turbulent kinetic energy is computed from the contributions of fluctuating component of x and y components of velocity. Fig. 3.12 compares the TKE spectra for the reacting jet cases of J = 3 ϕ_{jet} = 3 and J = 8 ϕ_{jet} = 3, at z = 5 mm. The TKE at the integral length scale (k~ 0.1) for J = 8 is found to be higher as compared to J = 3 case. This can be attributed to the fact that the jet Reynolds number for J = 8, Re_{jet} = 45000, is higher than that for J = 3, Re_{jet} = 27500, and the higher Reynolds number results in a higher turbulence kinetic energy. Thus, a higher momentum flux ratio induces higher levels of turbulence intensity into the flow field which implies a higher degree of mixing. In order to understand the effects of instantaneous heat release, the turbulent kinetic energy spectra of non-reacting jet of J =8 is compared with reacting jets of J = 8 and ϕ = 0.9 and 3, at z = 5 mm, as

shown in Fig. 3.13. At the integral length scale the TKE is higher for reacting jets as compared to the non-reacting jet, which is expected because the jet Reynolds number for the non-reacting jet case is $Re_{jet} = 27600$ and that of the reacting jet cases it is $Re_{jet} = 45000$. The TKE spectra of the reacting jets reveal an interesting finding. It can be seen that the TKE for reacting jet case of J = 8 and $\phi_{jet} = 0.9$ is around 1.5 times higher than J = 8 and $\phi_{jet} = 3.0$ at the integral length scale. This observation can be related to the fact that the reacting jet case for $\phi_{jet} = 0.9$ would tend to autoignite much more quickly than for the reacting jet case with $\phi_{jet} = 3.0$ which would require longer mixing time before it autoignites. Thus, locally in a plane closer to the nozzle exit reacting jet of $\phi_{jet} = 0.9$ would have higher heat release as compared to $\phi_{jet} = 3.0$. This implies that the reaction zone has a strong interaction with the flow field. But this will require further study by using HRR simultaneous PIV/OH-PLIF measurements. An interesting point to observe in the TKE spectra is that the curve flattens towards the higher wavenumber values unlike the theoretical spectra where there is a sharper rate of energy transfer to smaller length scales and eventually dissipating at the Kolmogorov length scale. This flattening of the curve is mainly due to the energy accumulation at the length scale corresponding to the minimum spatial resolution in the experiment. Since the Kolmogorov scales are not resolved in this experiment, complete dissipation of the turbulent kinetic energy cannot be seen in the energy spectra resulting in energy accumulation at the lowest length scale that could be measured in this experiment.

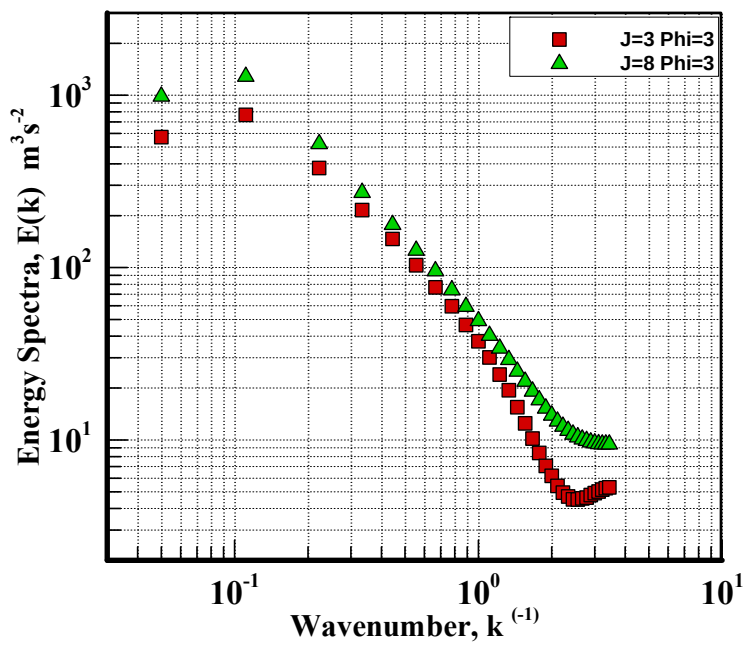

Figure 3.12 Turbulent kinetic energy spectra plotted in wave number space for the reacting jet cases J = 3, $\phi_{jet} = 3$ and J = 8, $\phi_{jet} = 3$.

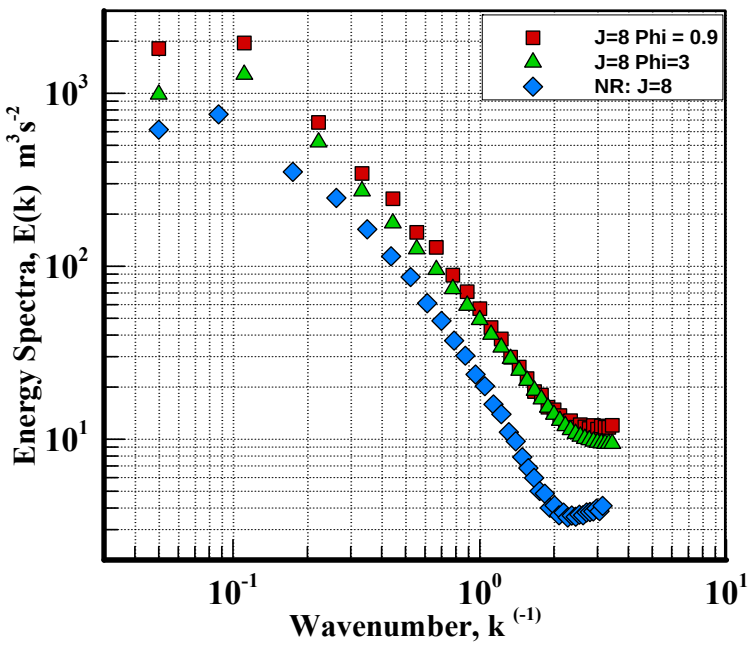

Figure 3.13 Turbulent kinetic energy spectra for the non-reacting jet case of J = 8 and the reacting jet cases of J = 8, ϕ_{jet} = 0.9 and ϕ_{jet} = 3, showing the effect of heat release on the flow field at measurement plane z = 5 mm.

In order to extract the wake dynamics, velocity fluctuation statistics are extracted from three locations for the J=3, ϕ_{jet}=3 case for the z = 5 mm measurement plane, as indicated in Fig. 3.14. These three locations are identified as the lower shear layer (LSL), upper shear layer (USL) and recirculation region (RR). To characterize the dynamics of the wake of the jet it is of interest to examine whether the vortical structures flow past a fixed point with a characteristic frequency. The power spectra of the x component of velocity (V_x) indicate a peak in the frequency at approximately 462 Hz at all three locations (Fig 3.15a, b and c). Thus, the event associated with this frequency is associated with strong dynamics in the flow-field. Based on this observation of the characteristic frequency of the wake and the instantaneous velocity magnitude and ω_z magnitude, it is hypothesized that the associated dynamics are the result of wake vortex shedding around the jet. This hypothesis will be further supported by the POD analysis on the vector field discussed in the next section.

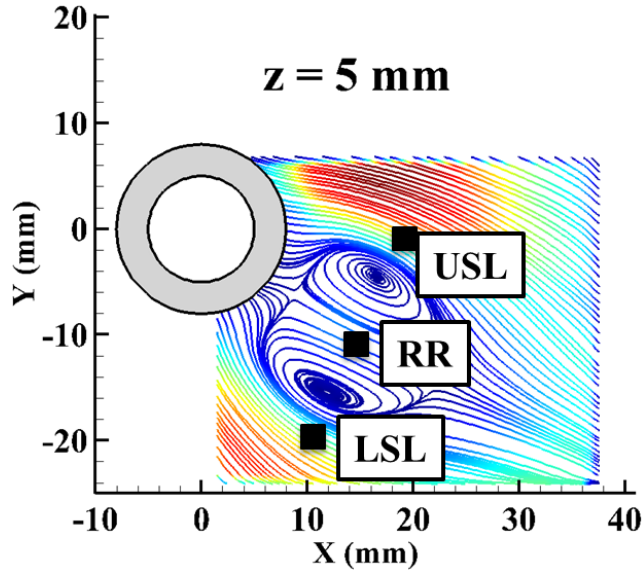

Figure 3.14 The flow field at z= 5 mm for J =3 and ϕ_{jet} = 3, is divided into three regions, upper shear layer (USL) (Region 1), recirculation region (RR) (Region 2) and lower shear layer (LSL) (Region 3).

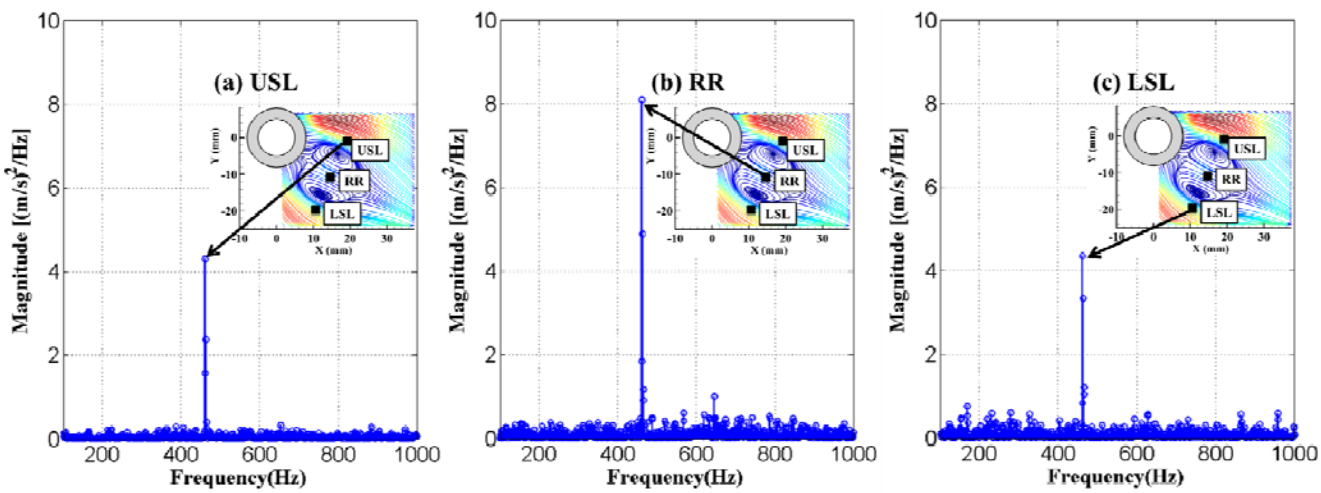

Figure 3.15 The power spectral density (PSD) of the fluctuating part of the x- component of velocity (V_x) for the three locations: (a) upper shear layer(USL) (location 1), (b) recirculation region (RR) (location 2) and (c) lower shear layer (LSL) (location 3). The plots indicates presence of a single peak frequency at f = 462 Hz.

3.3.4. Wake Strouhal number of the RJICF

The wake Strouhal number (St_{wake}) is based on the wake frequency (f_{wake}), jet exit diameter (D) (the internal diameter of the protruding injector), and the area averaged mean upstream crossflow velocity magnitude (U_∞), as defined below in Eq 2,

$$St_{wake} = \frac{f_{wake} D}{U_\infty} \qquad \textbf{Eq. 2}$$

Within the wake region of the jet the wake Strouhal number depends on the mode of injection of the jet into the crossflow. In an experimental study, (Moussa *et al.* 1977) derived important conclusions on the wake field of an isothermal transverse jet issuing from a nozzle protruding into the crossflow. One of the main findings of the study was that the wake Strouhal numbers for protruding transverse jets closely matched the wake Strouhal numbers for a cylindrical bluff body, and differed from those of the flush mounted jets. In another study of an isothermal transverse jet (Fric and Roshko 1994) a flat rectangular metal plate or 'skirt' was mounted flush with the nozzle's upper edge; found that the wake Strouhal number deviates from that of a cylindrical bluff body by as much as 50%. Fric and Roshko (1994) hypothesized that the vortices generated within the boundary layer of the nozzle wall are responsible for the wake vortices. In the current work the flow field is more complex than that of Moussa *et al.* (1977) and Fric and Roshko (1994) due to the presence of swirling motion in the crossflow and chemical reactions leading to instantaneous heat release. However, the velocity measurements within the wake of the RJICF show a very similar behavior in the wake dynamics. Our analysis shows that the wake Strouhal number of the non-reacting jets was 0.132 and it was found to be invariant of the jet momentum flux ratio. In the case of the reacting jets the wake Strouhal number is found to be dependent on the jet equivalence ratio, which is indirectly related to the local heat release. For ϕ_{jet} = 0.9, St_{wake} is 0.150 and 0.147 for the J=3 and J=8 cases, respectively. In the case of ϕ_{jet} = 3.0 it is found to be 0.128 and 0.122 for J = 3 and 8, respectively. The exact nature of dependence on the local heat release is still unknown. However, as a conjecture it is proposed that in the case of ϕ_{jet} = 0.9, due to higher local flame temperature the wake vortical structure is found to be smaller as compared to ϕ_{jet} = 3.0. As a result the flow field will exhibit afaster shedding frequency and hence a higher St_{wake}. The values of the wake Strouhal number computed for all of the JICF/RJICF cases are shown in Table 3.2.

Table. 3.2 Strouhal number, St_{wake} corresponding to the wake vortices frequency for all the test cases.

Case	TYPE	Momentum Flux Ratio, J	Jet	ϕ_{jet}	f_{wake} (Hz)	St_{wake}
1	NR	3	Air	NA	172	0.132
2	NR	8	Air	NA	172	0.132
3	R	3	Premixed NG	0.9	540	0.150
4	R	3	Premixed NG	3.0	462	0.128
5	R	8	Premixed NG	0.9	530	0.147
6	R	8	Premixed NG	3.0	440	0.122

SubTask 3.4: High-Speed PIV Measurements for HHC Gas Jets Injected Into Vitiated and Nonvitiated Crossflows

2D PIV measurements are performed along the jet cross-section to extract the prevalent flow structures and to understand their influence on the jet flame. Time averaged velocity vectors measured at z = 10mm for the reacting jet case of J=8 and 40%H_2/60%N_2 are shown in Fig. 3.16. Fig 3.16a shows the time averaged velocity vectors overlaid on top of the x-component of velocity (V_x). The two concentric circles centered at x= 0 mm and y = 0 mm shows the physical location of the nozzle exit plane. The mean direction of the velocity vectors indicates a strong influence of swirling crossflow on the reacting jet. The jet and crossflow fluid form a shear layer that surrounds the wake of the jet. Within the two shear layer there are two distinct regions with high velocity. A strong recirculation region is evident between the two high speed flow regions. The recirculation region is a characteristic feature of the wake of the jet. The velocity vectors overlaid on top of y-component of velocity, shown in Fig 3.16b, indicates a strong negative y velocity component confirming the swirling crossflow is pushing the jet in a net downward direction. The out of plane vorticity component, ω_z, shown in Fig 3.16c provides a strong evidence of the presence of a steady wake structure enveloped between the top and bottom shear layer. The wake vorticity entrains the jet fluid and the crossflow fluid within the wake of the jet, leading to chemical reactions and stabilization of a reaction zone. The time averaged flow streamlines provide a different visualization of the wake of the jet, as shown in Fig 3.16d. Two counter-rotating flow structures are observed at x = 5 mm, y = 0 mm and x = 25 mm and y = -20 mm.

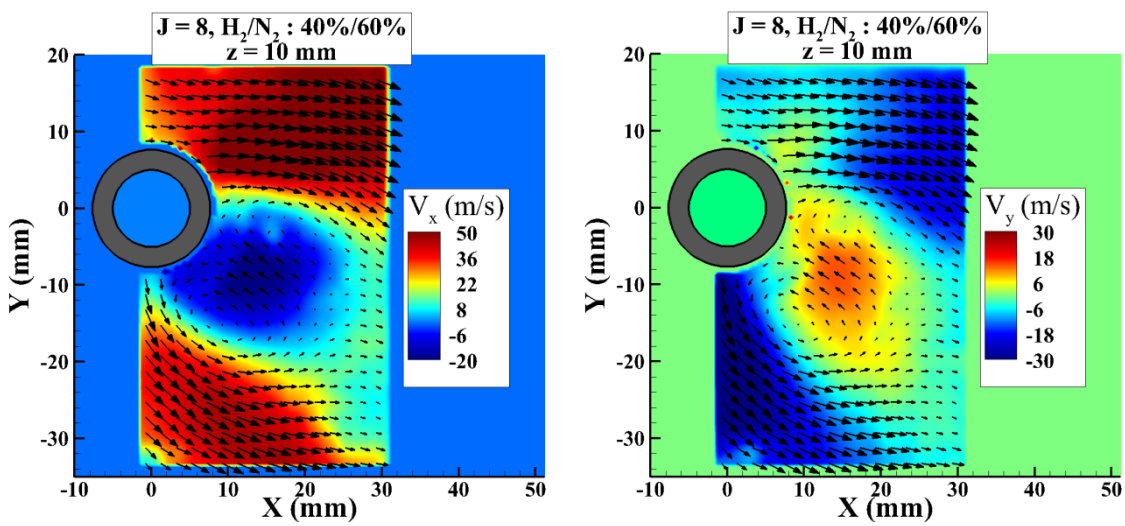

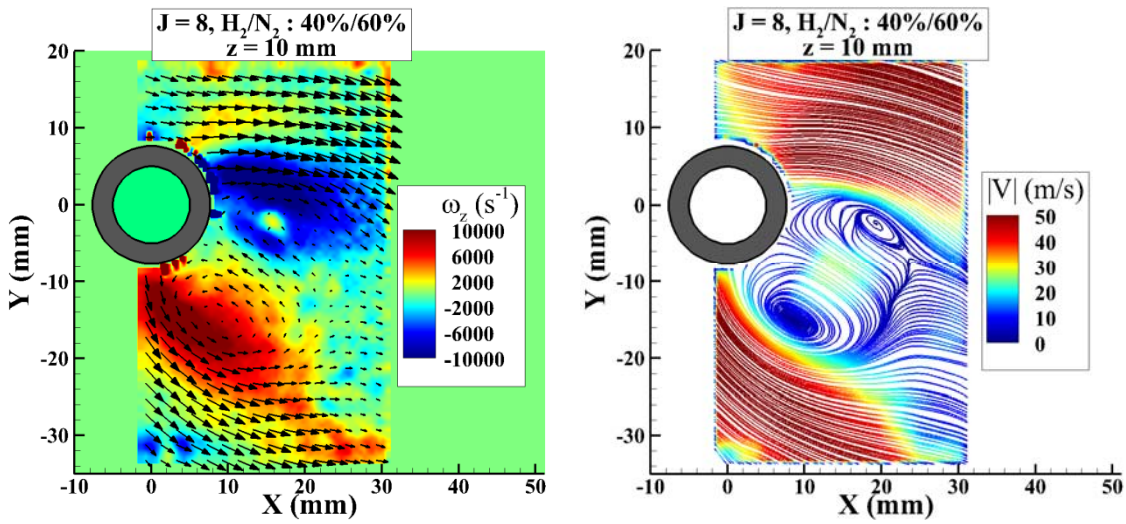

Figure 3.16 Time averaged velocity vectors for reacting jet case of 40% H_2/60% N_2 J=8 measured at z = 10mm. The velocity vectors are overlaid on top of (a) x-velocity, V_x, (b) y-velocity, V_y, and (c) z-vorticity, ω_z, (d) time averaged streamlines colored by velocity magnitude.

A consecutive sequence of instantaneous vector field for the reacting jet case of J = 8 and 40%H_2/60%N_2 measured at z = 10mm is shown in Fig 3.17. In Fig. 3.17a a sequence of instantaneous velocity vectors overlaid on top of x-component of velocity vector is shown. The x-component of velocity clearly shows that the flow field comprises of three main regions, the upper and lower shear layer marked with high velocity and the inner recirculation region. These sequences of velocity field could very well capture the time evolution of the wake vortical structure. At time t = 0.2 msec, a vortex structure appears at x = 0 mm and y = -10 mm. At time t = 0.4 msec this flow structure has convected downstream and a second structure appears at the same location. The time resolved PIV measurement could successfully capture these wake structures and their spatio-temporal evolution. These flow structures can be seen clearly in the instantaneous vorticity and flow streakline plots as shown in Fig. 3.17b and c. Based on visual inspection the size of the flow structure appears to be 6 – 8 mm in diameter. Similar flow structures are observed on the upper shear layer part of the flow field. When compared with the instantaneous OH-PLIF images (discussed under Task 4), the wake vorticity seems to be responsible for providing the characteristic structure to the flame front. It entrains the hot gases and reactants and helps stabilizing a reaction front within the core of the jet which has relatively lower velocity magnitude and hence lower compressive strain rates. As the high repetition rate PIV and OH-PLIF experiments are done separately only qualitative conclusions can be drawn from this study. In order to extract quantitative information, HRR simultaneous PIV/PLIF experiment needs to be conducted which is a part of future work in the current research.

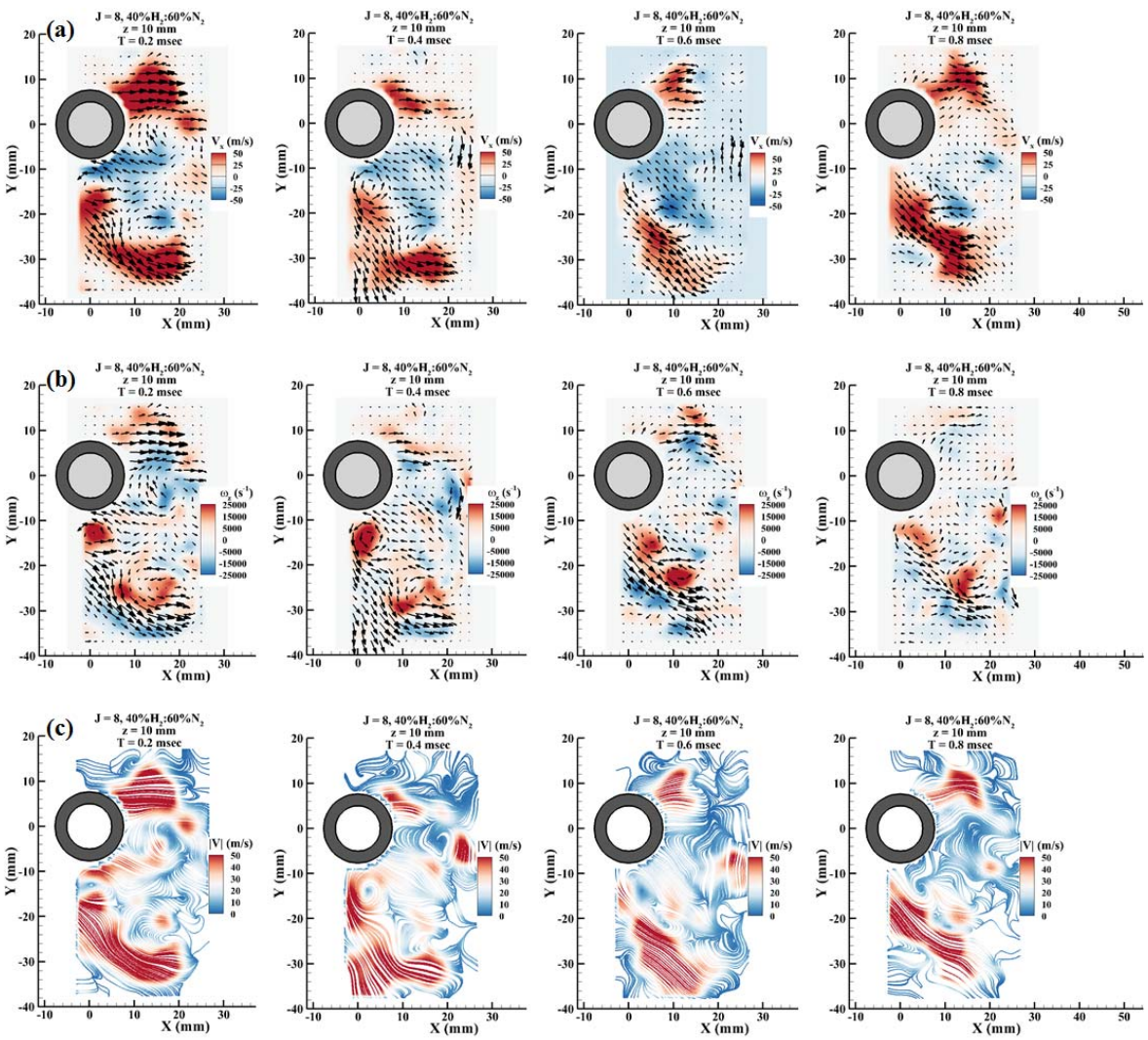

Figure 3.17 Instantaneous velocity vectors for the reacting jet case of 40% H_2/60% N_2, J=8, measured at z = 10mm. The consecutive sequence of velocity vectors are 0.2 msec. The velocity vectors are overlaid on top of (a) x-component of velocity (V_x), (b) z-component of vorticity (ω_z) and (c) instantaneous flow streaklines colored by velocity magnitude.

The velocity fluctuation statistics is extracted from the recirculation region for J = 8; 40% H_2/60% N_2 case at z = 10 mm measurement plane. To characterize the dynamics of the jet wake it is necessary to investigate whether the wake vortical structures flow past a fixed point at a characteristic frequency. The power spectra of the x component of velocity (V_x) indicate a peak in the frequency at approximately 410 Hz, as shown in Fig 3.18. The flow field is phase averaged based on this frequency. Phase averaged flow-streamlines, as shown in Fig 3.19, shows the evolution of wake structure at various phase angles, it appears at a phase angle of 120°, which then rotates in plane in a clockwise direction and eventually disappears at 330°. Since, the velocity measurements shown in this study is based on 2D PIV, not much can be stated about the dependence of the flow field on out of plane component of velocity. In order to fully understand the spatial evolution of wake structures stereo PIV based three component velocity

measurements are necessary; however, due to the limited optical access it was not feasible for this study.

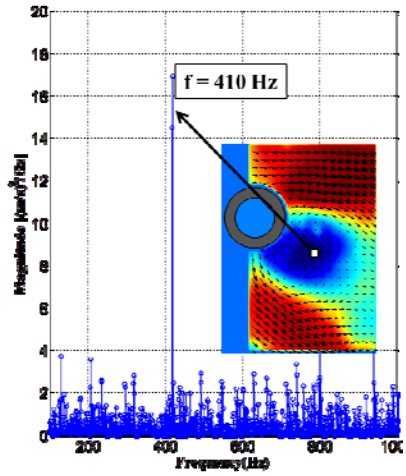

Figure 3.18 Power spectral density (PSD) of the fluctuating part of the x- component of velocity (V_x) extracted from the recirculation region for the reacting jet case of 40% H_2/60% N_2 J=8, measured at z = 10 mm. The plot indicates presence of a single peak at a frequency, f = 410 Hz.

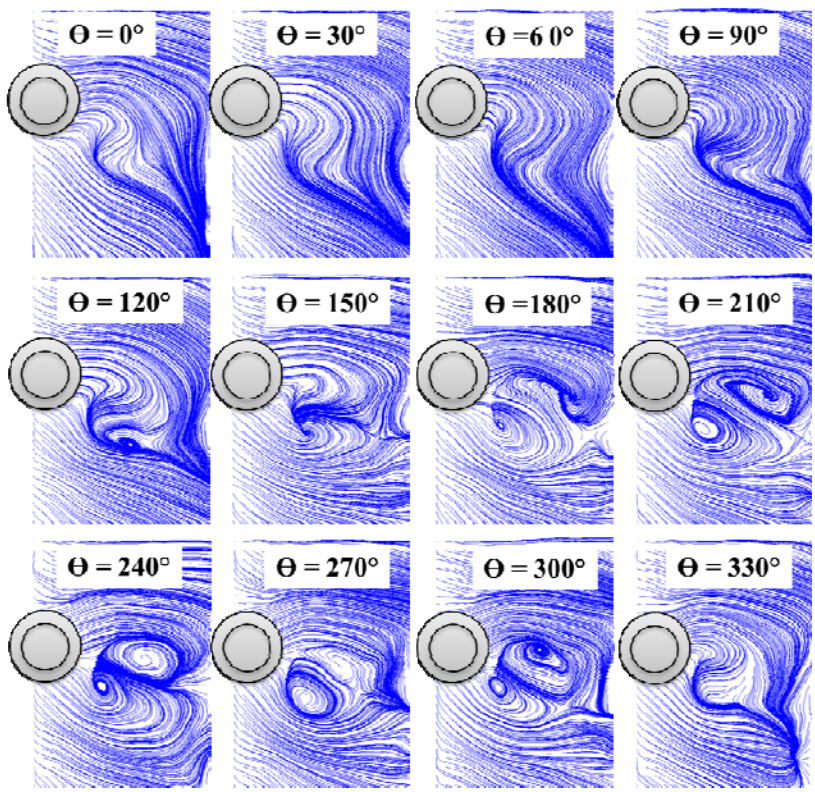

Figure 3.19 Phase averaged flow -streamlines for the reacting jet case of J=8; 40%H_2/60%N_2 case at z = 10mm.

TASK 4.0: HIGH-SPEED OH PLIF STUDIES

The OH PLIF system consists of a high repetition rate diode-pumped, Q-switched Nd:YAG slab laser (Edgewave – IS8IIDZ) that pumps a frequency-doubled dye laser (Sirah Credo). The fundamental output of the dye laser system is frequency doubled and tuned to excite Q1(7) transition line of the A-X (v′ = 1, v″=0) band of OH at 283.2 nm.The laser system is operated at 10 kHz with pulse energy of 0.5 mJ/pulse at 283.2 nm. For OH-PLIF measurements the laser beam is collimated and is expanded into a sheet that is 30 mm wide and 250 μm thick. The OH-PLIF signal is focused onto a high-speed image intensifier (LaVision IRO) using a UV enhanced camera lens (Soden Cerco 2178) with an f number of 2.8. The intensified signal is detected using a high-speed camera (Phantom v411). The intensifier time gate is set to 75 nsec to suppress noise due to OH* chemiluminescence. The OH-PLIF measurements were performed in two different configurations, one to visualize the jet flame trajectory in the x-z plane and second to visualize the jet flame cross-section in the x-y plane.

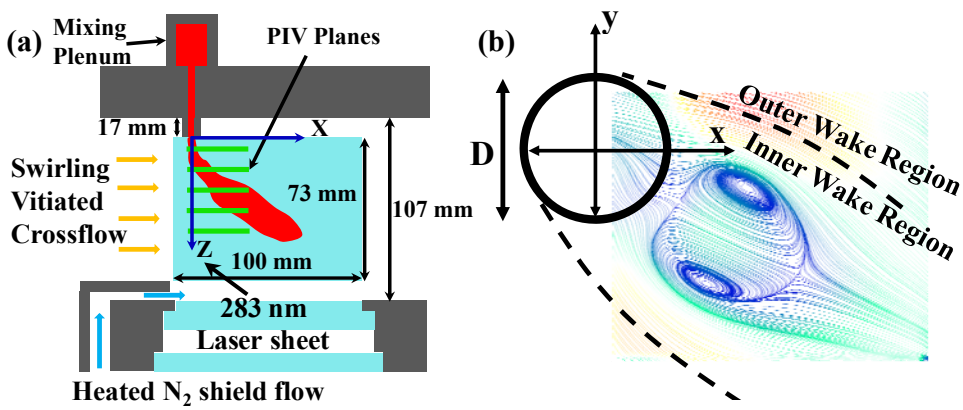

Figure 4.1 Schematic of the windowed combustor with an extended nozzle. The region shaded with blue color indicates the location of the 283nm laser sheet for OH-PLIF measurements of the flame trajectory and the lines in green indicate the locations of 532nm and 283 nm laser sheet for both PIV and OH-PLIF measurements, respectively.

The raw OH-PLIF images were post-processed in order to remove background noise and correct the non-uniformity in the laser sheet intensity profiles. Three main steps were followed in order to process the OH-PLIF images. Firstly, the images were multiplied by the calibration to convert them from pixel to physical space. The calibration process also included rotational correction in case of any minor tilts in the images. In the next step the calibrated images were background subtracted. The background images were collected by taking images at the same measurement planes by blocking the laser sheet. Finally, the background subtracted images were normalized by the OH-PLIF images of only the vitiated crossflow for laser-sheet correction.

SubTask 4.1: High-Speed OH PLIF Measurements for Natural Gas Jets Injected Into Vitiated and Nonvitiated Crossflows

A time averaged OH-PLIF intensity field is shown in Fig. 4.2, highlighting the jet flame trajectory and the extent of penetration of the jet flame into the crossflow. These measurements were performed along the x-z plane which is normal to the PIV measurement planes. The

injector is shown in a grey box protruding into the flow field. The crossflow moves from left to right in the figure. The time averaged images show that there is no reaction in the windward side of the jet and the jet flame is anchored along the leeward side of the jet. The unreacted part of the jet core for the J = 8 case, as highlighted in Fig. 4.2, is longer than the reacting jet case of J = 3, indicating deeper penetration of the reacting jet for higher momentum flux ratio. For both the reacting jet case, J=3 ϕ_{jet} = 3 and J=8 ϕ_{jet} = 3, it can be clearly seen that the wake of the jet exhibits a strong OH-PLIF intensity field, hence, justifying the focus of current paper on understanding the flow-field within the wake of the jet.

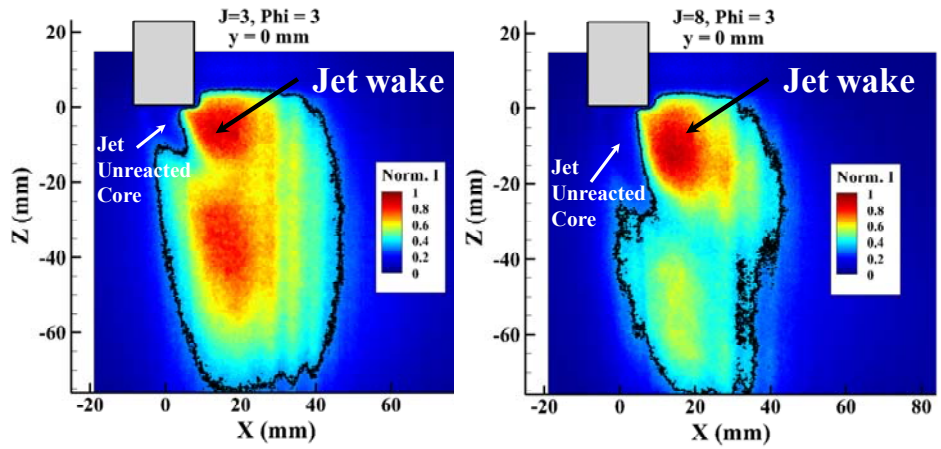

Figure 4.2 Time averaged normalized OH-PLIF intensity field for reacting jet cases of J=3 ϕ_{jet} = 3 and J=8 ϕ_{jet} = 3 measured at y = 0 mm, indicating the jet flame trajectory under the influence of swirling crossflow.

A consecutive sequence of OH-PLIF images each 0.2 msec apart is shown in Fig. 4.3 for J=3 and ϕ_{jet} = 3 case at the mid-plane. The yellow rectangle represents the extended nozzle. The crossflow direction is from left to right of the image. The images exhibits clear distinction between the reacting and non-reacting part of the flame. The flame structure is highly convoluted with occasional flame shedding being observed. There seems to be distributed reaction fronts in this case, one being attached to the core of the jet and another one being further deep into the crossflow as a result of flame shedding-off the jet. The jet sheds off unreacted gas which reacts further deep into the crossflow. The flame is seen to anchor on both windward as well leeward side of the jet, with a broader PLIF signal being seen on the leeward side of the nozzle exit, which is most likely due to the wake stabilization of the reaction zone.

In case of higher momentum flux ratio of J =8, a similar sequence of OH-PLIF images shows that the core of the jet penetrates further into the flow field as compared to J = 3 case,as shown in Fig. 4.4. The jet flame similar to the J = 3 case exhibits two reaction zones, one on the windward side and the other on the leeward side. The broader PLIF signal in the leeward side of the flame seems to be a characteristic feature of RJICF, which is again attributed to the wake stabilized reaction zone. Unlike the J=3 case the flame front in J=8 is connected to the jet core, although multiple reaction zones are seen, but distinct flame shedding-off the main jet flame structure is not seen. This could be because much more mixing of the premixed NG fuel is achieved in case of J=8 case as compared to J=3 for the same jet equivalence ratio, as a result some of the premixed fuel escapes in case of J =3 and reacts in a separate reaction zone located deep in the crossflow.

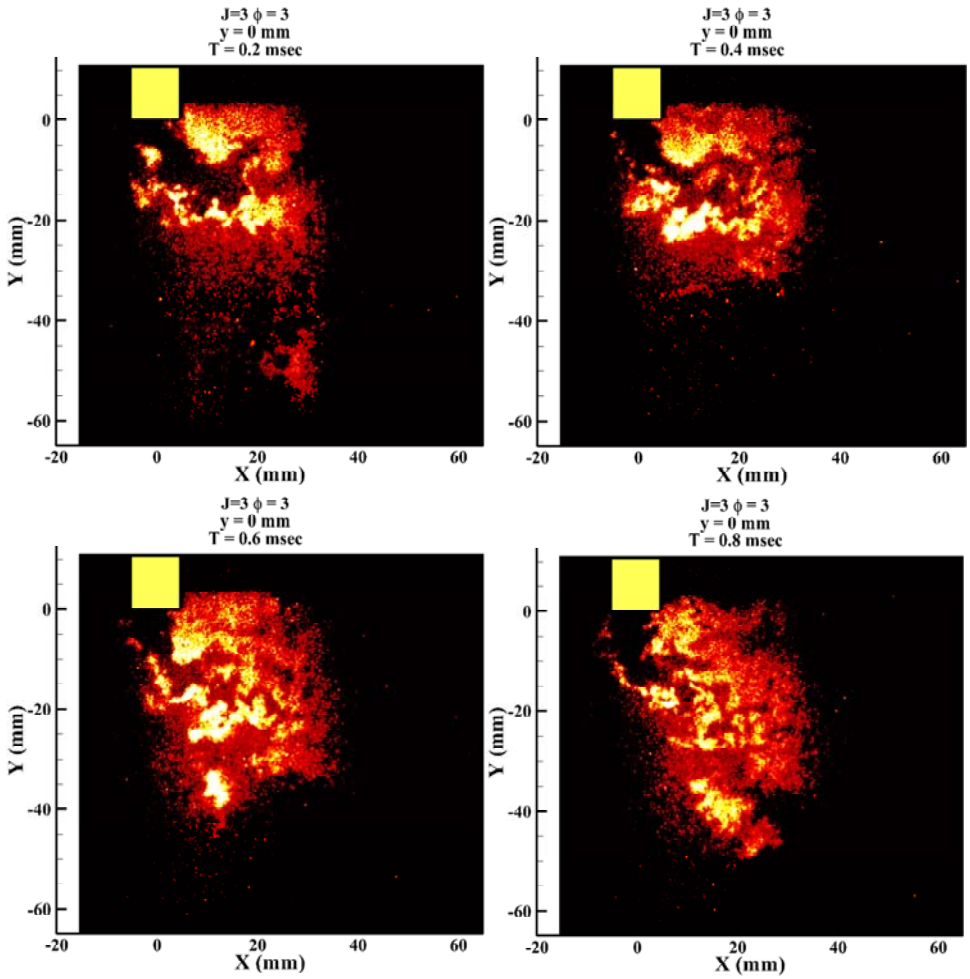

Figure 4.3 Consecutive sequence of single shot OH-PLIF images for the reacting jet case of J =3 ϕ_{jet} = 3, measured at plane y = 0 mm.

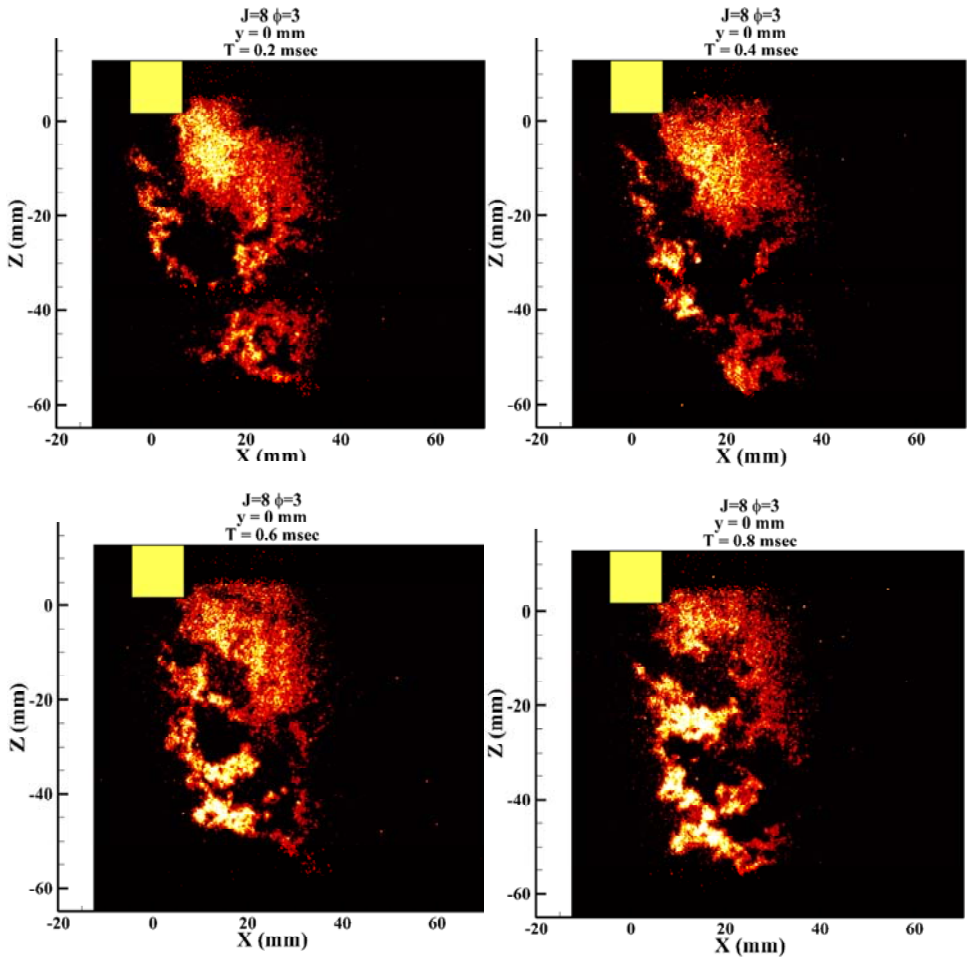

Figure 4.4 Consecutive sequence of single shot OH-PLIF images for the reacting jet case of J =8 ϕ_{jet} = 3, measured at plane y = 0 mm.

A sequence of processed OH-PLIF images corresponding to the reacting jet case for J = 3 and ϕ_{jet} = 3.0 is shown in Fig. 4.5. This sequence of images is based on measurement along the cross-section of the jet, lying in the x-y plane. The measurement plane shown here corresponds to z = 5 mm. The grey concentric circles represent the physical location of the nozzle, centered at x = 0 mm and y = 0 mm, with the smaller circle corresponds to the jet exit diameter (D = 10 mm). The natural gas jets do not show any OH-PLIF intensity on the windward side of the jet. This could be due to large compressive strain rates prevalent on the windward side of the jet making it difficult to sustain a stable reaction front. However, the leeward side and wake region of the jet seem to be favorable in sustaining a stable reaction zone. This sequence of images is an illustrative of the complexity of the flame structure prevalent in an RJICF. An interesting transient behavior is observed between time t = 0.1 msec to 0.4 msec. The flame front is being pushed downstream at locations x = 15 – 20 mm and y locations corresponding to y = -5 mm and -20 mm. Eventually, part of the flame front breaks-off from the main body of the reaction zone. This observation highlights the importance of obtaining velocity, vorticity and strain rate field simultaneously at these locations in order to identify the role of fluid dynamics in local extinction leading to flame break-up.

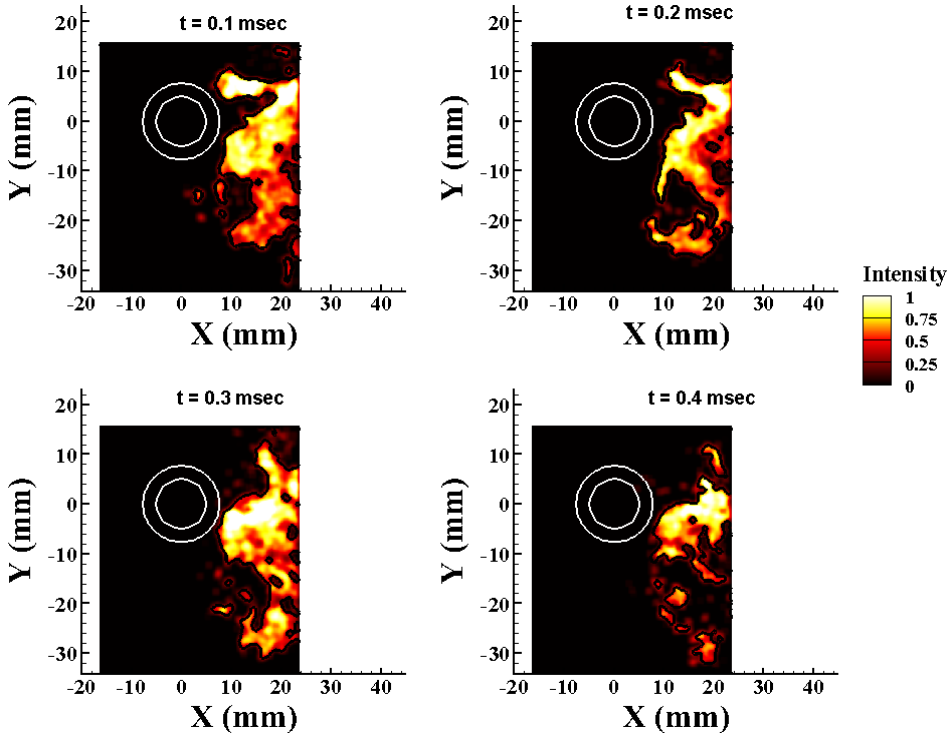

Figure 4.5 Instantaneous OH-PLIF intensity field overlaid on top of the flame front edge for the reacting jet case of J = 3, ϕ_{jet} = 3.0 at plane z = 5 mm.

SubTask 4.2: High-Speed OH PLIF Measurements for HHC Gas Jets Injected Into Vitiated and Nonvitiated Crossflows

Four reacting jet conditions are investigated in this study, corresponding to two different fuel compositions (40% H_2/60% N_2 and 50% H_2/50% N_2) and two jet momentum flux ratios J=3 and J=8. However, results from reacting jet case of J = 8 and fuel 40%H_2/60%N_2 are discussed in this paper. The RJICF is visualized at 17 planes in steps of 4 mm along the x-z plane to obtain a steady three dimensional structure of the jet flame. In order to capture the sequence of auto-igniting H_2 jet, the camera and laser system are synchronized with the secondary fuel valve actuation. This is performed only at the center plane (y = 0 mm) of the jet flame trajectory. A series of instantaneous processed OH-PLIF images showing the temporal evolution of the auto-igniting jet is shown in Fig 4.6, for the reacting jet case of J = 8 and fuel 40%H_2/60%N_2. In these sequences of images every second image is shown and the yellow rectangle represents the physical location of the injector. Consider, at time T = 0.0 msec the first flame kernel appears in the leeward side of the jet attached to the nozzle exit. This flame kernel propagates 40 mm into the crossflow within 1.2 msec when a thin reaction front appears along the windward side of the jet. It takes approximately 3.6 msec to establish a fully connected jet flame that penetrates 50 – 60 mm into the crossflow. During the entire sequence of auto-ignition the reaction front along the windward side stays thin and the OH-PLIF intensity is observed to be the lowest in the entire reaction front. In this side of the jet the reaction occurs mainly within the jet and crossflow shear layer and it takes about 1.2 – 2.0 msec to attain a chemically reactive mixture in the windward side. The thin reaction front in the windward side is mainly due to high levels of compressive

strain rates leading to high scalar dissipation rate. On the other hand, the leeward side and the near wake region of the jet sees a dramatic increase in the intensity of OH-PLIF. Most of the heat release and fuel-air entrainment occurs in the wake of the jet, leading to super-equilibrium concentrations of OH radical owing to high fluorescence intensity in these regions. Thus, we can see that the wake of the jet is able to provide flow condition that leads to efficient fuel-air mixing and a stable reaction zone. Consecutive sequence of processed OH-PLIF images at the center plane for 40% H_2/60% N_2 J=3case is shown in Fig. 4.7. The flame front shows a diffusion flame like sharp gradients in the OH-PLIF signal, clearly distinguishing between the reacting and non-reacting part of the flame. The signal to noise ratio in case of H_2/N_2 jet flame is found to be much higher as compared to the premixed NG jet flame. The flame front is thin and highly convoluted both along the windward and leeward side of the jet. When compared to the natural gas reacting jets, the H_2/N_2 jet flame appears vastly different, especially, in terms of flame thickness along the windward and leeward side of the jet. The premixed natural gas flame is seen to have a much broader a diffused PLIF signal as compared to extremely well defined flame boundaries for the H_2/N_2 jet flames. In case of lower momentum flux ratio, J=3, both natural gas and H_2/N_2 jet flames share similar characteristics, where both jets shed off unreacted gas from the main jet and have a flapping nature. Again at higher momentum flux ratio, J=8, higher levels of mixing is achieved as result the wake stabilized reaction zone is comparable to that of the premixed NG jet flame, as shown in Fig. 4.8.

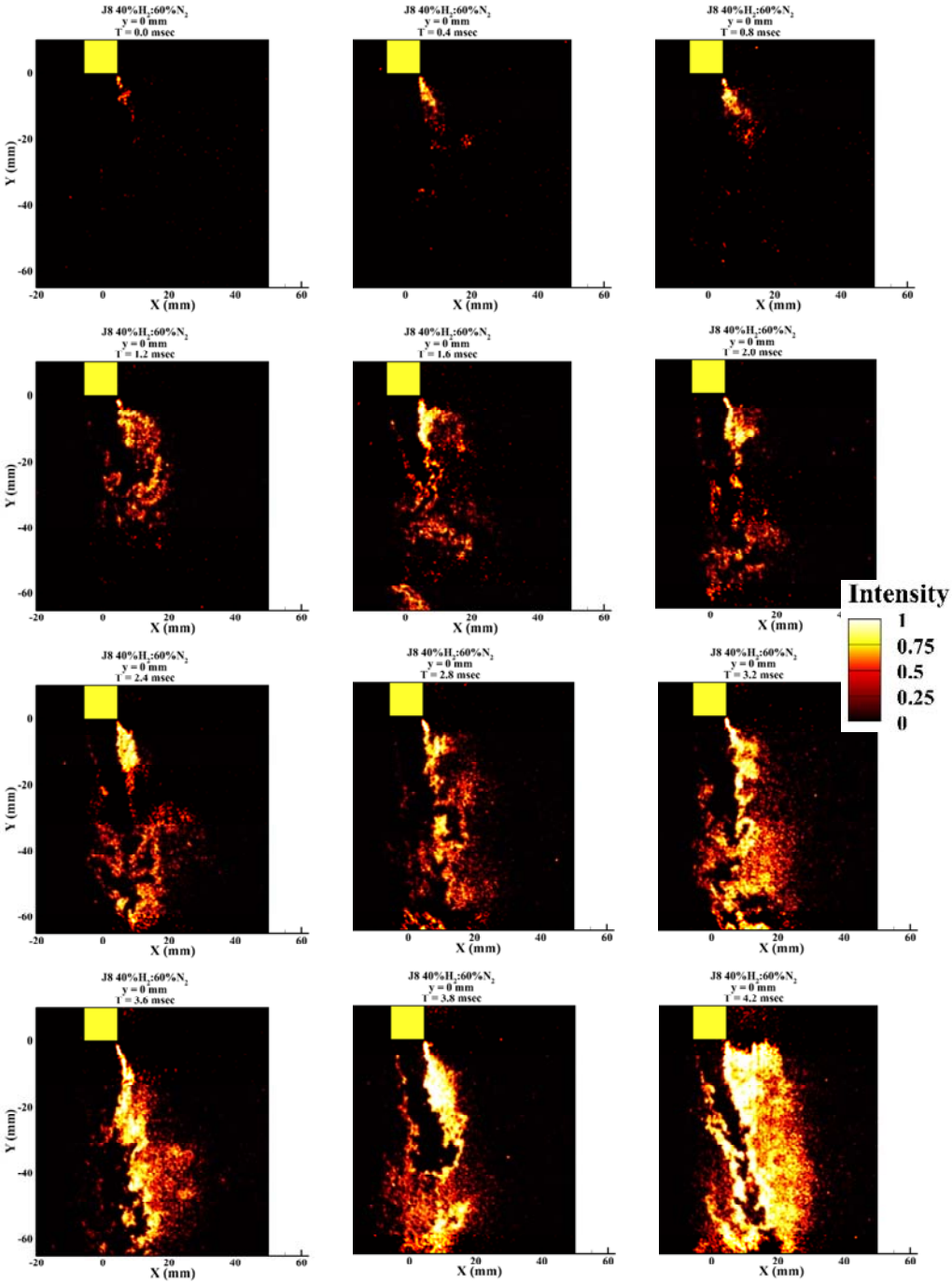

Figure 4.6 OH PLIF single-shot images for the reacting jet case of 40% H_2/60% N_2, J=8 ameasured at the jet center plane (y = 0 mm). The sequence of images indicates the initiation of auto-ignition and temporal evolution of the flame front.

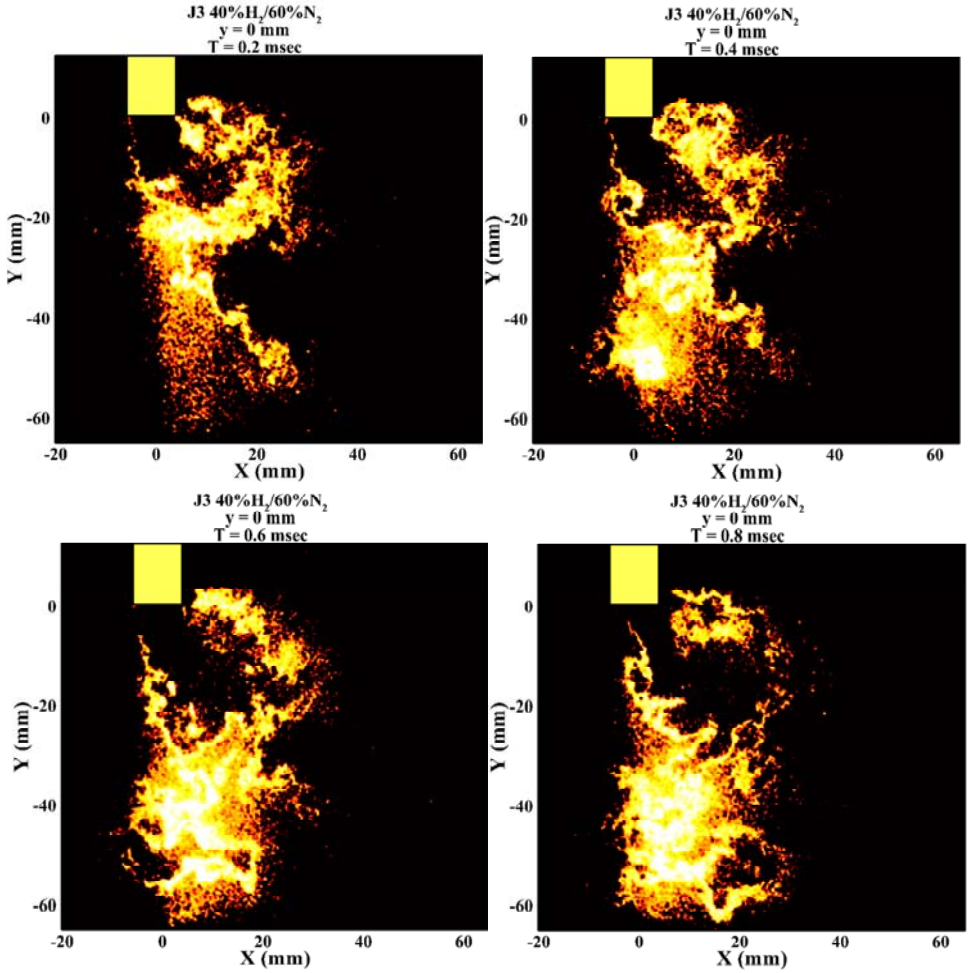

Figure 4.7 Consecutive sequence of OH PLIF images for the reacting jet case of J=8 40% H_2/60% N_2 measured at the jet center plane (y = 0 mm).

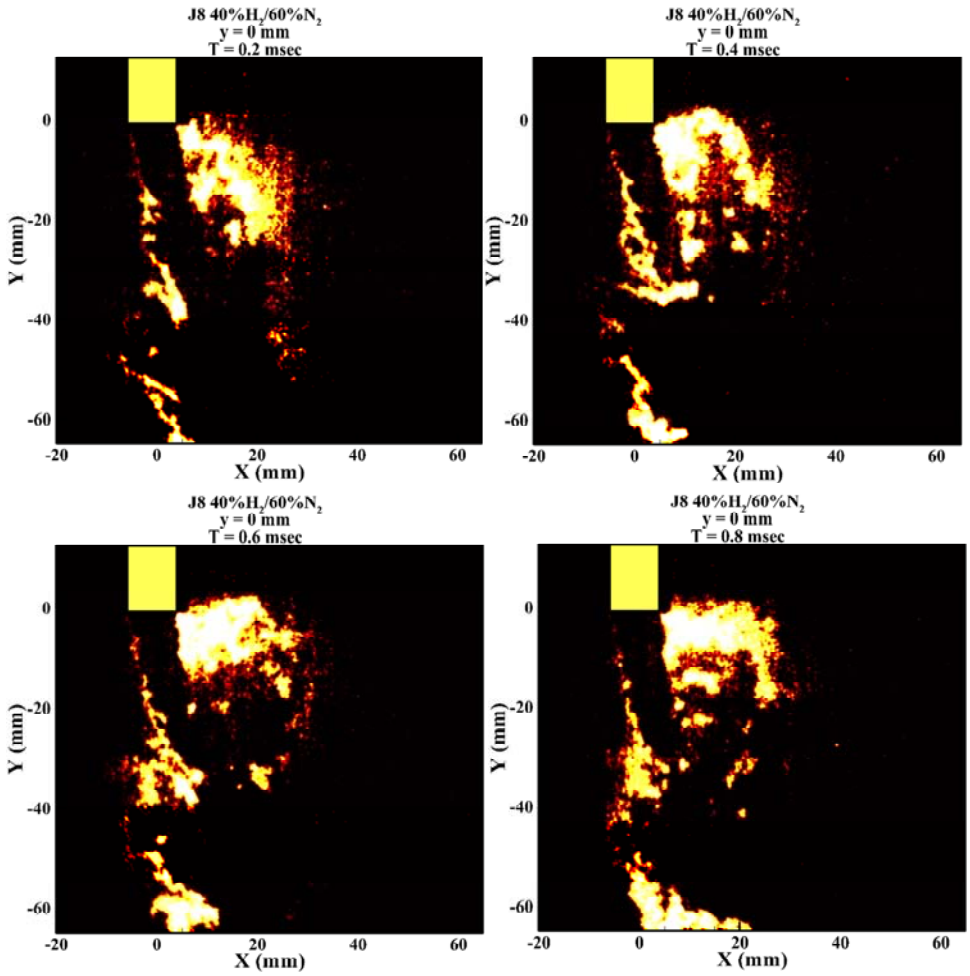

Figure 4.8 Consecutive sequence of OH-PLIF images for the reacting jet case of J =8 40% H2 and 60% N2 measured at plane y = 0 mm.

We have also performed OH-PLIF measurements along the cross-section of the jet flame. The OH-PLIF measurement planes correspond to the same planes where HRR-PIV measurements are performed. A sequence of instantaneous OH-PLIF images of the jet flame cross-section is shown in Fig 4.9 for the reacting jet case of J=8 and 40%H_2/60% N_2 at the measurement plane z = 10 mm, where z indicates the distance from the nozzle exit plane. The jet flame reaction front is observed to have a highly distorted flame structure. The direction of the mean crossflow is shown by the white arrow in the first image, which is based upon the PIV measurements discussed in the subsequent section. Under the influence of swirling crossflow the jet flame is anchored at an angle to the nozzle exit plane. The white concentric circles represent the inner and outer diameter of the injector. It is observed that the flame front tries to wrap around the core of the jet entraining hot products and unburnt fuel air mixture into the wake of the jet. The flame structure can be described as two arm like structure the envelopes a region with a broad OH-PLIF intensity field of the jet flame. From image 1 at time T = 0.2 msec – 1.2 msec this region between the two arms of the jet flame moves towards the nozzle in a direction opposite to the mean flow field, indicating the presence of a recirculation region that pushes the products and fuel-air mixture in this region towards the nozzle. The flame is always anchored on both the windward and leeward side of the jet. Similar to the observation along the jet flame

trajectory, along the cross-section of the jet flame too the OH PLIF signal in the windward region is much weaker than the OH PLIF signal on the leeward side. This behavior could be attributed to the local compressive strain rates that are much higher on the windward side as the jet encounters the crossflow.

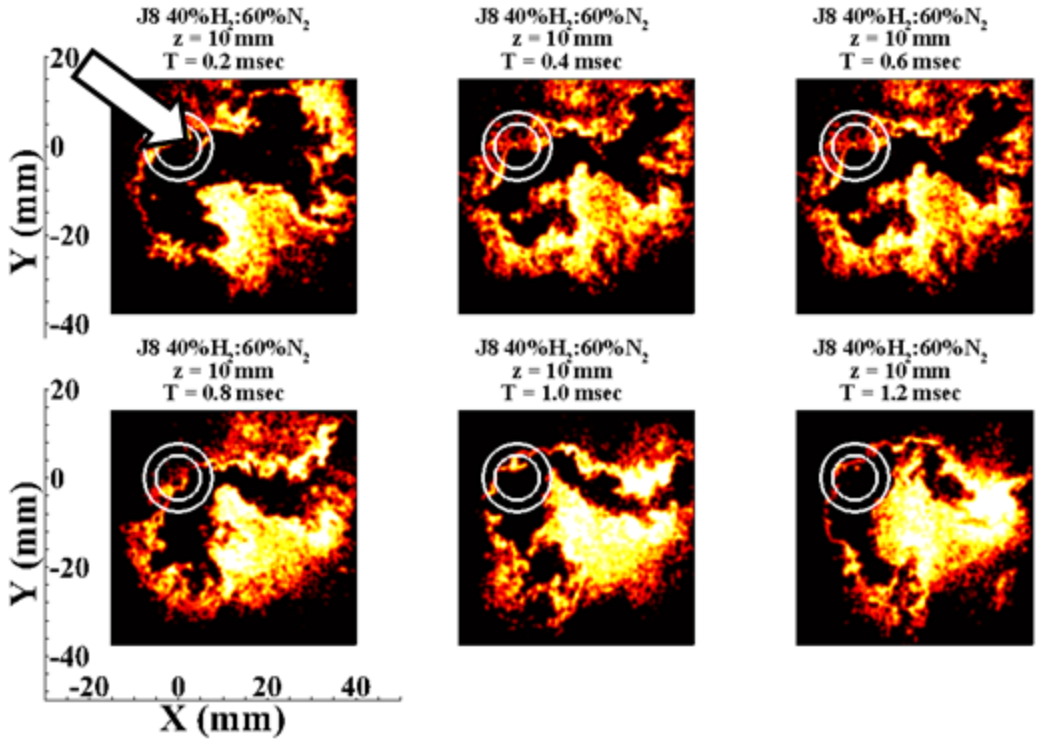

Figure 4.9 Instantaneous OH PLIF images for the reacting jet case of 40% H_2 60% N_2 J =8 along the cross-section of the jet flame visualized at z = 10mm. The consecutive sequence of OH-PLIF images are 0.2 msec apart.

TASK 5.0: SIMULTANEOUS HIGH-SPEED PIV/PLIF STUDIES

SubTask 5.1: Development of Optical and Data Acquisition Systems for Simultaneous High-Speed PIV/OH PLIF Measurements

5.1.1 Measurement Techniques

Two component PIV and OH-PLIF technique are applied simultaneously at a repetition rate of 10 kHz to study the dynamics and turbulence-chemistry interaction in a reacting jet injected into a swirling vitiated crossflow. A brief description of these techniques is provided in this section.

OH-PLIF System

The OH PLIF system consists of a high repetition rate diode-pumped, Q-switched Nd:YAG slab laser (Edgewave – IS8IIDZ) that pumps a frequency-doubled dye laser (Sirah Credo) that produces a 283 nm beam in UV. The laser system is operated at 10 kHz with

ultraviolet pulse energy of 0.5 mJ/pulse at 283 nm wavelength. The laser beam is directed into a reference leg featuring a bunsen burner to tune the fundamental frequency of the dye laser in order to excite the Q1 (6) transition of the OH molecule. After this the laser beam is collimated and is focused using a 1000 mm focal length positive spherical lens, a cylindrical lens of -25.4 mm focal length and finally by a 300 mm focal length positive cylindrical lens forming a laser sheet that is 30 mm wide and 250 μm thick. The PLIF laser sheet is oriented in such a way to visualize the cross-section of the jet flame. A 3D schematic of the simultaneous PIV/PLIF system (Figure 2) shows the orientation of both the 532 nm and 283 nm laser sheet going into the window combustor. The OH-PLIF signal is focused onto a high-speed image intensifier (LaVision IRO) using a UV enhanced camera lens (Soden Cerco 2178) with F/2.8.and detected using a high-speed camera (Phantom). The intensifier is set to a gating of 75 nsec in order to reduce noise due to OH* chemiluminescence.

PIV System

The PIV system consists of a high repetition rate, dual cavity, diode-pumped solid state Nd:YAG laser (Quantronix Dual Hawk 80-M) and a high speed CMOS camera (Photron-FASTCAM SA5). Each of the cavity outputs a pulse energy of 3.5 mJ/pulse at 10 kHz and 532 nm. A picture showing the experimental test rig illuminated with the 532 nm laser beam during the test operation is shown in figure 8 indicating the locations of the two camera systems, dichroic mirrors and sheet forming optics. The time delay between the two pulses is optimized to 10 μsec in order to account for the high and slow speed flow field and a strong out of plane component of the jet velocity prevalent in the RJICF. A collimated laser beam is focused using a 1000 mm focal length positive spherical lens, a cylindrical lens of -50 mm focal length and a 250 mm cylindrical lens forming a laser sheet that is 35 mm wide and 500 μm thick. A dichroic mirror that transmitted 532 nm wavelength and reflected 283 nm wavelength was used to overlap the two laser sheets before entering the combustor. The two camera systems (OH-PLIF and PIV camera systems) were installed perpendicular to each other as a result another dichroic mirror was used that transmitted 532 nm scattered light from the PIV particles and reflected the 310 nm PLIF signal to the high speed IRO-camera system. The flow field was seeded with TiO_2 particles with nominal diameter of 250 nm. The scattered light from the particles were collected using a 105 mm Nikon lens. The test rig has two locations to seed the flow field, i) Upstream of the LSB and ii) along with the jet. For the experiements discussed in this paper only the jet fluid was seeded. The time delay in the PLIF laser was adjusted so that it lied in between the two pulses of 532 nm. The high speed controllers for the PIV and PLIF camera systems were synced to an external function generator (Quantum Composer 9520 Digital Delay Pulse Generator) that provided the input signal and necessary time delay to the laser systems. A 3D dot target was used to calibrate the images. Calibration was always performed just before beginning the experiment.

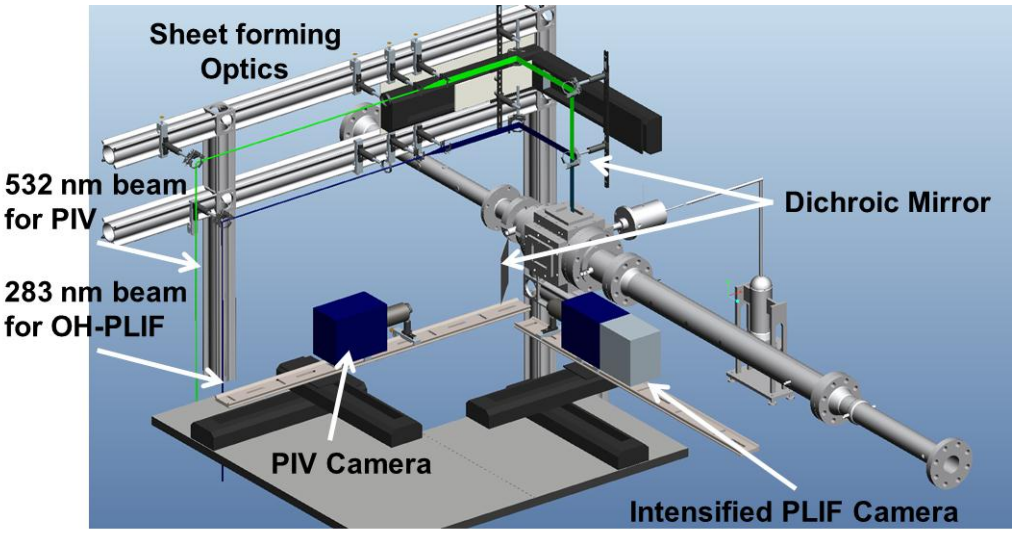

Figure 5.1 A three dimensional CAD schematic of the high repetition rate simultaneous PIV/OH-PLIF experimental system.

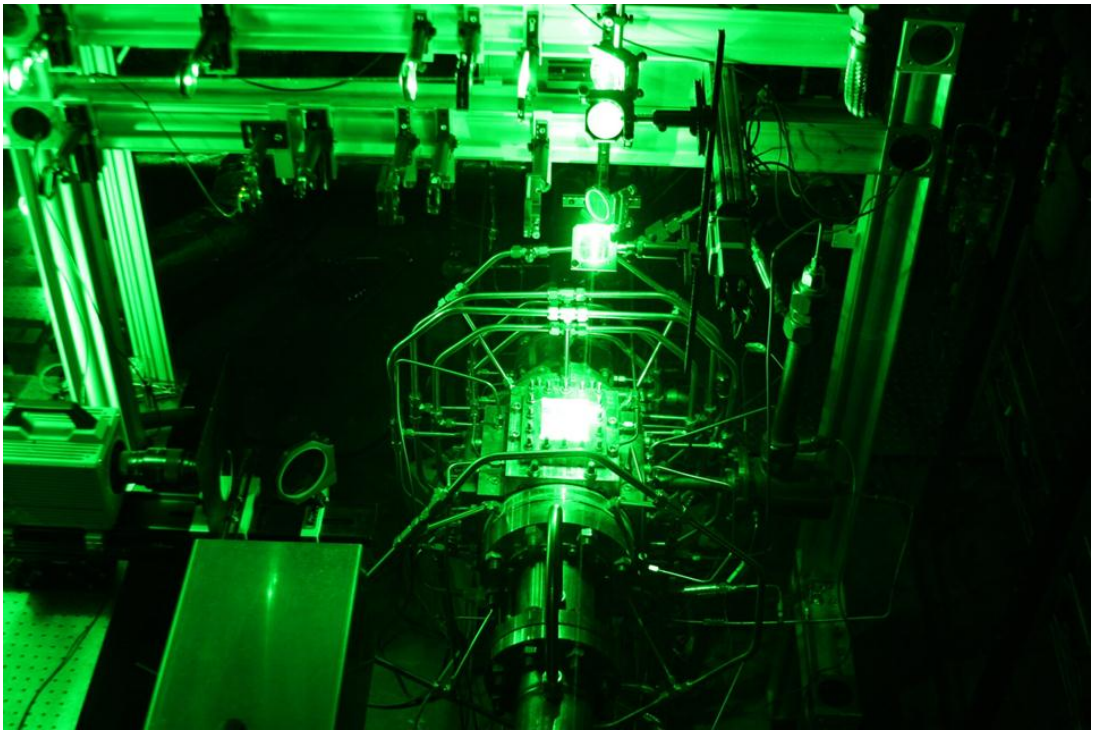

Figure 5.2 Photograph of test rig under operation, with the laser sheets going from top window of the combustor.

5.1.2 Data Post Processing

OH-PLIF Image Processing

The raw OH-PLIF images collected needed to post-processing in order to correct some experimental factors, remove background noise and increase the signal to noise ratio and finally correction of the non-uniformity in the laser sheet intensity profiles. Three main steps were followed in order to process the OH-PLIF images. Firstly, the images were multiplied by the calibration to convert them from pixel to physical space. The calibration process also included rotational correction in case of any minor tilts in the images. In the next step the calibrated images were background subtracted. The background images were collected by taking images at the same measurement planes by blocking the laser sheet. Finally, the background subtracted images were normalized by the OH-PLIF images of only the vitiated crossflow for sheet correction and then the normalized intensity was multiplied by a constant factor to further enhance the OH-PLIF signal. A total of 500 background images were collected from all the measurement planes. Each of the raw images were subtracted by the time-averaged background image, similarly the background subtracted images were normalized by the time averaged PLIF image of the vitiated crossflow for laser sheet correction. A MATLAB image processing algorithm was developed for flame front/edge detection.

Vector Field Computation

The PIV imaging was performed using the high speed camera integrated with a LaVision high speed controller. The controller was synchronized to an external function generator that provided the time delay for frame straddling between the two laser pulses. A 3D dot target was used to calibrate the PIV images before each experiment. The vector field was computed using the LaVision 8.1.4 software. A detailed analysis, based on the particle density, the time delay between the two laser pulses and cross-correlation technique, was carried out to maximize the cross-correlation value. A multi-pass cross correlation technique was adopted for vector computation with the first pass window size was chosen to be a square 64 X 64 pixel window followed by an auto adaptive window of 16 X 16 pixels for the second pass. Since, the jet was seeded for the PIV measurements only a portion of the particle images could be used for vector computation and rest of the image is masked. The field of view utilized to perform cross correlation was 35 mm x 55 mm, with a vector resolution of 0.8 mm x 0.8 mm. Also, in order to account for the influence of the out of plane velocity component of the jet the laser sheet thickness and Δt between the image pairs were optimized to, 500 μm and 10 μsec respectively. Based on these parameters the total number of rejected vectors varied between 15 – 25 % and a signal to noise ratio was always greater than 1.2. In order, to capture the turbulent statistics a total of 10,000 image pairs were captured at each measurement planes at a rate of 10 kHz.

SubTask 5.2: Simultaneous High-Speed PIV/OH PLIF Measurements for Natural Gas Jets Injected Into Vitiated and Nonvitiated Crossflow

The subtask involved simultaneous PIV/OH-PLIF based planar measurements for premixed natural gas jets injected into vitiated crossflow. A sequence of flame front edges (based on maximum OH-PLIF gradient), from time t = 0.1 msec – 0.8 msecs, overlaid on top of the processed OH-PLIF images corresponding to reacting jet case of J = 3 and ϕ_{jet} = 0.9 are shown in Fig. 5.3a. The measurement plane corresponds to z = 5 mm. The sequence of images

captures various flame dynamics like, flame break-up due to local extinction, re-ignition etc. The grey concentric circles represent the physical location of the nozzle, centered at x = 0 mm and y = 0 mm, with the smaller circle corresponds to the jet exit diameter (d = 10 mm). The natural gas jets do not show any OH-PLIF intensity in the windward side of the jet. This is due to large compressive strain rates prevalent at these locations making it difficult to sustain a stable reaction front. However, the leeward side and wake region of the jet seems to be extremely favorable in sustaining a stable reaction zone. The reaction zone is stabilized slightly downstream of the nozzle within the near wake region of the jet. This sequence of images is an illustrative of the complexity of the flame structure prevalent in an RJICF. Between time t = 0.1 msec to 0.8 msec it is observed that the flame front particularly in the lower shear layer region of the jet gets elongated and eventually breaks-off from the main reaction zone. The reaction zone has a characteristic kidney like shape that could be imparted due to the interaction of the flame front with the wake vortices. Figure 5.3b shows the flame edge and velocity vectors overlaid on the contours of axial velocity. The contour map ranges between -60 m/s - 60 m/s. The red contour represent strong positive x velocity and blue represents strongly negative x velocities. The interface between inner and outer wake regions of the jet sees highest magnitude of positive x velocity and the recirculation region sees a strong negative x velocity with velocity vectors pointing against the direction of swirl. The high positive x-velocity pushes the reaction zone downstream and the negative x velocity within the recirculation region pushes the reaction zone towards the nozzle exit. The sequence of velocity vectors between time t = 0.1 msec – 0.8 msec shows strong x-velocity within the upper and lower shear layer of the jet which correlates very well with the flame transient of localized displacement and elongation of the reaction front followed by breaking off from the main flame body. Figure 5.3d shows the sequence of out plane vorticity magnitude (-15000 s^{-1} – 15000 s^{-1}) which provides a much better picture of vortex and flame interaction. The vorticity plot in the sequence of vector field seems like shear layer vorticity with an alternate positive and negative vorticity magnitude seen at the USL and LSL. The counter-rotating wake vortex structure is seen which wraps the reaction front around it and pushes it downstream until it the reaction zone detaches at time t = 0.8 msec. The observed local extinctions could be due to a combined effect of higher instantaneous values of vorticity magnitude (which in this case exceeds 15000 s^{-1}) coupled with significantly higher instantaneous compressive strain rates. Thus, it is clearer that the observed flow structures which are essentially the wake vortices of the jet have a significant effect on the reaction zone. It entrains the surrounding hot product or unburnt fuel air mixture into the recirculation region which has a relatively lower magnitude of velocity and stabilizing a reaction zone within it. The instantaneous flow structures seen in the wake region of the jet are approximately 5 – 10 mm in

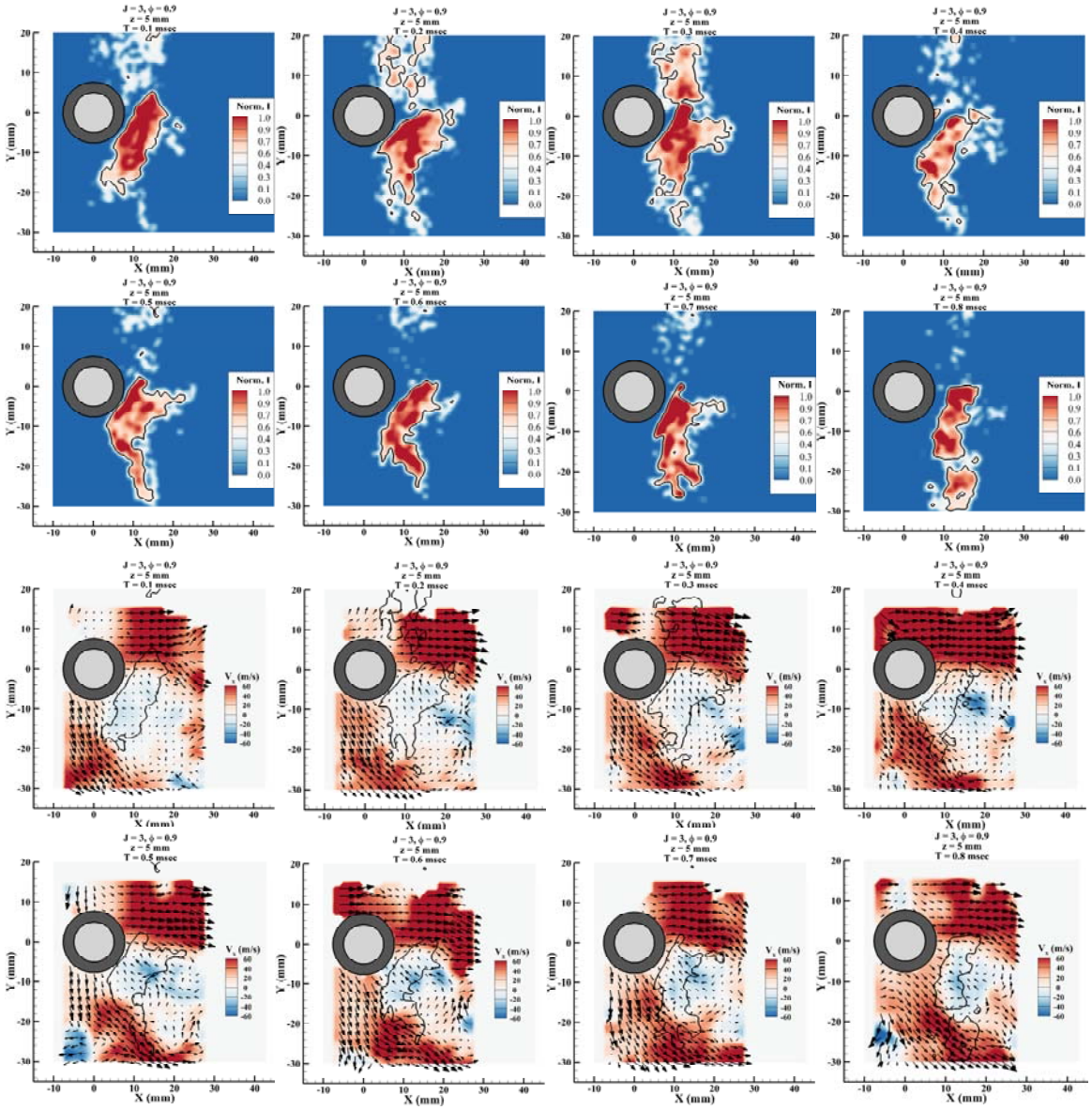
J = 3, ϕ = 0.9
z = 5 mm
T = 0.1 msec
T = 0.2 msec
T = 0.3 msec
T = 0.4 msec
T = 0.5 msec
T = 0.6 msec
T = 0.7 msec
T = 0.8 msec
Norm. I
V_x (m/s)
X (mm)
Y (mm)

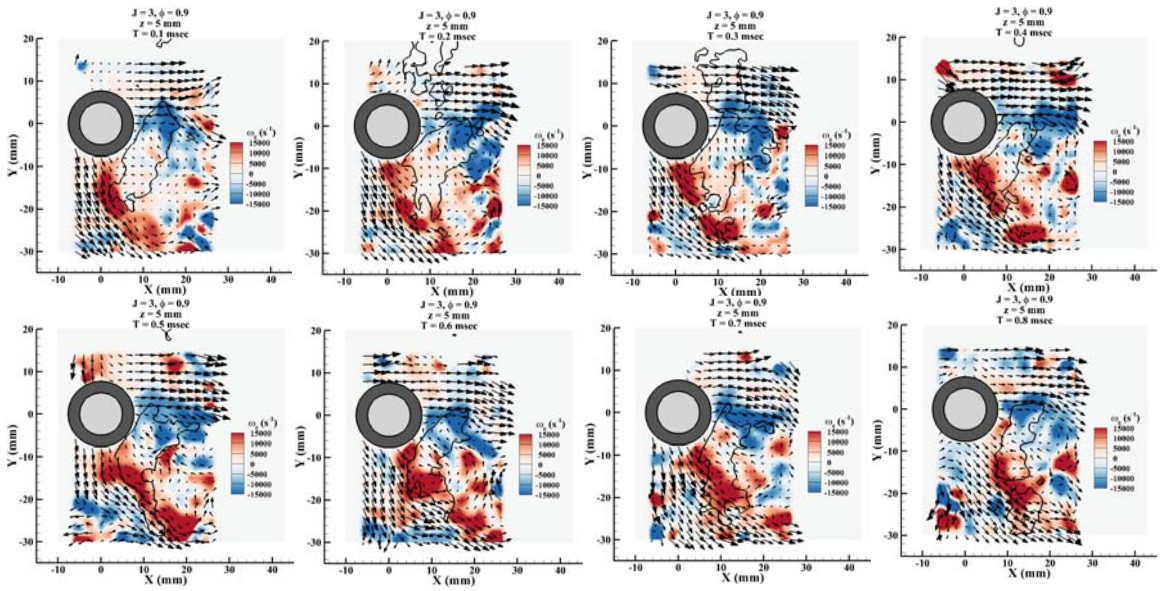

Figure 5.3 Instantaneous sequence of (a) Reaction fronts overlaid on top of OH-PLIF images–time separation = 0.1 ms. (b) Reaction fronts overlaid against contours of x-velocity and velocity vectors, (c) Reaction fronts overlaid against contours of vorticity, for the reacting jet case of J = 3 ϕ_{jet}= 0.9 at z = 5 mm.

SubTask 5.3: Simultaneous High-Speed PIV/OH PLIF Measurements for HHC Gas Jets Injected Into Vitiated and Nonvitiated Crossflows

The subtask involved simultaneous PIV/OH-PLIF based planar measurements for H_2/N_2 jets injected into vitiated crossflow. A sequence of flame front edges (based on maximum OH-PLIF gradient), from time t = 0.1 msec – 10 msecs, overlaid on top of the processed OH-PLIF images corresponding to J = 8 case and visualized at z = 10 mm are shown in Fig. 5.4a . The sequence of images captures various flame dynamics like, flame break-up due to local extinction, re-ignition, flame holes, etc. The black concentric circles is the physical location of the nozzle, centered at x = 0 mm and y = 0 mm, with the smaller circle corresponds to the jet exit diameter (d = 10 mm). There is a faint OH-PLIF signal present right above the location of the nozzle in almost all the images. This is an indicative of the fact that in case of an H_2 diffusion flame there is some amount of reaction occurring within the windward side of the jet, however, due to large compressive strain rates prevalent at these locations it's difficult to sustain a stable reaction front. However, the leeward side and wake region of the jet seems to be extremely favorable in sustaining a stable reaction zone. This sequence of images is an illustrative of the complexity of the flame structure prevalent in an RJICF. The first image sequence indicates a strong OH-PLIF signal level at y = 10 mm and between x = 0 to 10 mm, which could be an indicative of super equilibrium concentration of OH radical. There is a discontinuity between the highest OH-PLIF concentration at this location and rest of the flame body. But the reaction front re-attaches to the main body of the flame either due to through plane flame propagation or due to auto-ignition of a fresh mixture of fuel and air at around x = 10 mm and y = -10 mm. A similar behavior is observed between frame 6 – 10 at location x = 18 mm and y = 0 - 10 mm location where alternately there is local extinction and re-ignition but behavior could be mainly due to through plane flame propagation or bulk transport of OH. There is another interesting transient observed

between images 3-6 a sudden necking of the reaction zone which eventually breaks-up from the main body of the reaction zone convecting away downstream. By the look of this transient behavior it is now important to have velocity, vorticity and strain rate information at that location in order to identify the exact region of location extinction leading to flame break-up. The flame structure has a characteristic shape that could be imparted due to the vortex-flame interaction which will be discussed in the subsequent sections.

Figure . 5.4b shows the flame edge and velocity vectors overlaid on the contours of axial velocity.. The contour map ranges between -60 m/s - 60 m/s. The red contour represent strong positive x velocity and blue represents strongly negative x velocities. The interface between inner and outer wake regions of the jet sees highest magnitude of positive x velocity and the recirculation region sees a strong negative x velocity with velocity vectors pointing against the direction of swirl. The high positive x-velocity pushes the reaction zone downstream and the negative x velocity within the recirculation region pushes the reaction zone towards the nozzle exit. The image sequences 1 – 5 shows strong x-velocity within the upper shear layer which correlates very well with the flame transient of necking of the reaction front followed by breaking off from the main flame body. The same sequence of velocity vectors and flame front are overlaid on top of the y-velocity magnitude, as shown in Fig. 5.4c which provides a clearer picture of strong positive y-velocity between image 1 – 5 within the USL, which again correlates well with the flame front necking behaviour. The lower shear layer (LSL) sees high magnitudes of negative y-velocity, which is attributed to the incoming swirling crossflow. Again, between the images 6 – 10 there is an increase in the magnitude of y-velocity within the recirculation region that pushes the reaction front closer to the location of the nozzle. Figure . 5.4d shows the sequence of out plane vorticity magnitude (-25000 s^{-1} – 25000 s^{-1}) which provides a much better picture of vortex and flame interaction. The vorticity magnitude seen in the image sequence 1 -2 seems like shear layer vorticity with an alternate positive and negative vorticity magnitude seen at the USL and LSL. However, at image 3 a vortex structure (with a counter-clockwise rotation represented by red contour) located just below the nozzle at x = 5 mm and y = -15 mm is seen which wraps the reaction front around it and pushing it downstream until frame 8 after which the lower reaction front detaches from the main reaction zone at location x = 16 mm and y = -24 mm due to local extinction. The observed local extinctions could be due to a combined effect of higher instantaneous values of vorticity magnitude (which in this case exceeds 25000 s^{-1}) coupled with significantly higher instantaneous compressive strain rates. Thus, it is clearer that the observed flow structures which are essentially the wake vortices of the jet have a significant effect on the reaction zone. It entrains the surrounding hot product or unburnt fuel air mixture into the recirculation region which has a relatively lower magnitude of velocity and stabilizing a reaction zone within it. The instantaneous flow structures seen in the wake region of the jet are approximately 5 – 10 mm in size.

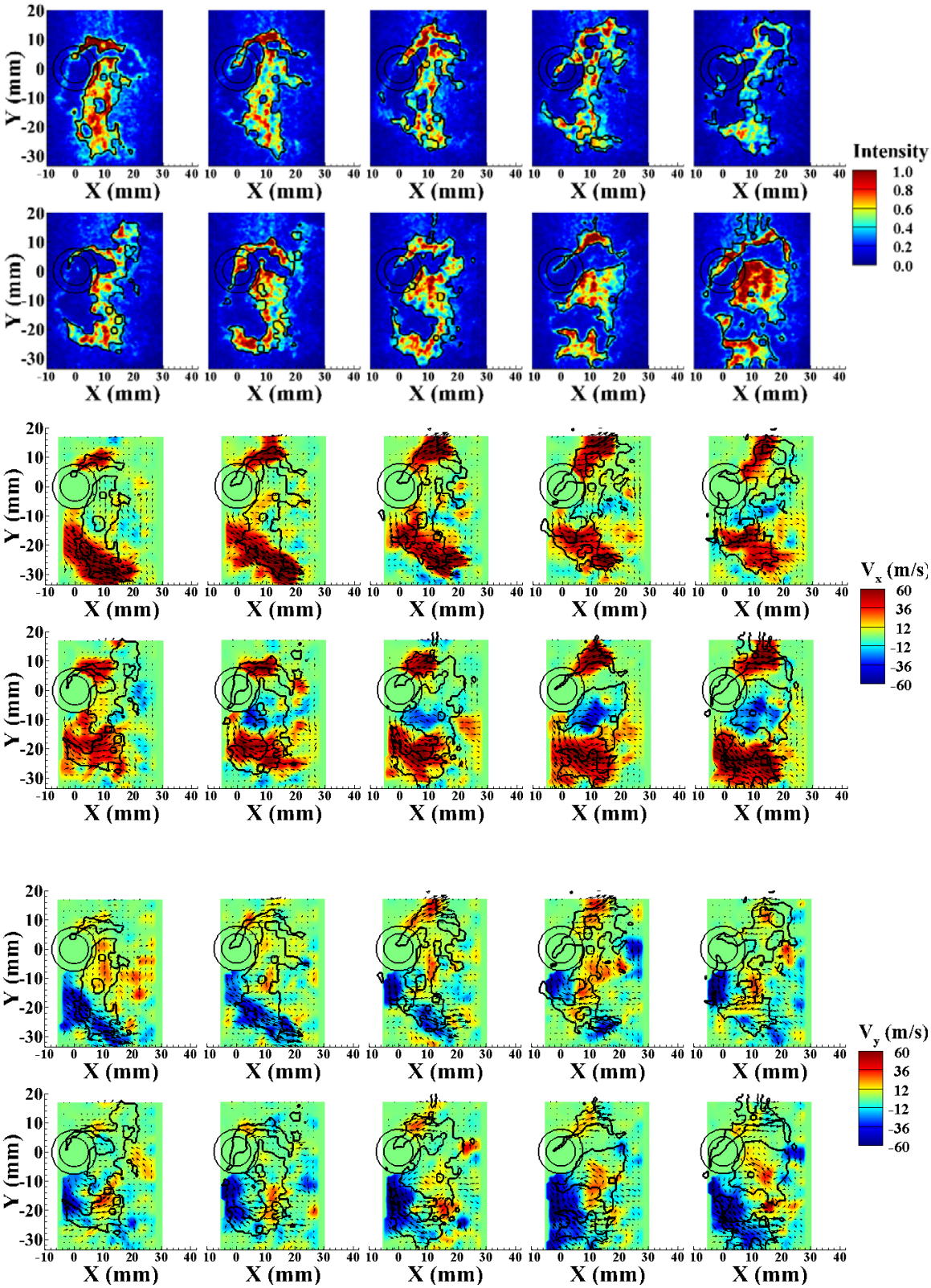
Intensity
1.0
0.8
0.6
0.4
0.2
0.0
V_x (m/s)
60
36
12
-12
-36
-60
V_y (m/s)
60
36
12
-12
-36
-60
Y (mm)
X (mm)

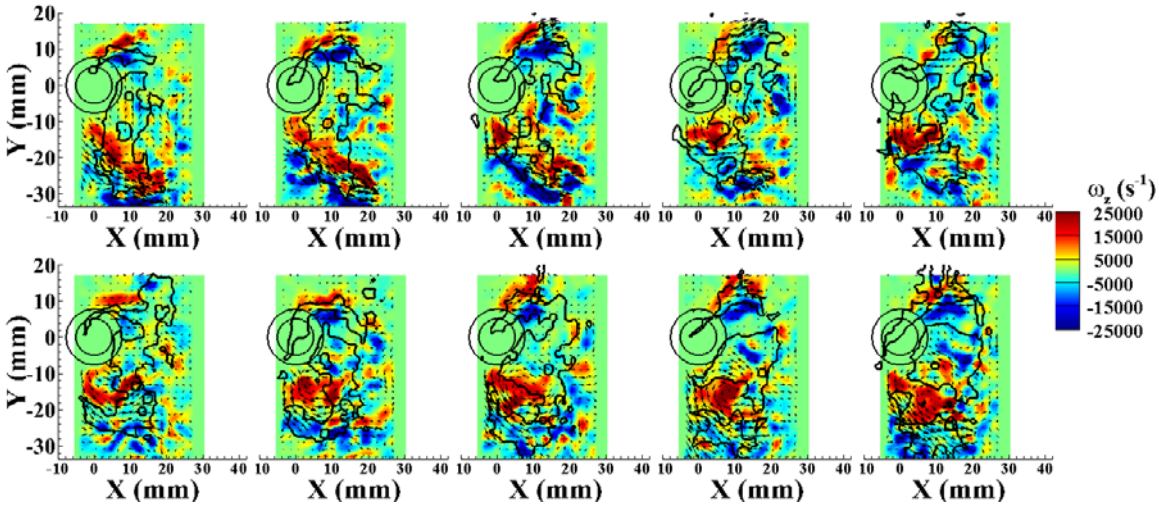

Figure 5.4 Instantaneous sequence of (a) Reaction fronts overlaid on top of OH-PLIF images–time separation = 0.1 ms. (b) Reaction fronts overlaid against contours of x-velocity and velocity vectors, (c) Reaction fronts overlaid against contours of y-velocity and velocity vectors. (d) Reaction fronts overlaid against contours of vorticity, for the reacting jet case of J = 8 40%H_2/60%N_2 at z = 10 mm.

TASK 6.0: PIV/PLIF MEASUREMENTS OF COUPLED COMBUSTION DYNAMICS

SubTask 6.1: Modification of the Reacting Jet in Crossflow Apparatus for the Combustion Instability Studies

A proven means for producing combustion dynamics has been used for performing combustion instability studies on the reacting jet in crossflow configuration. The method used to provide an unsteady flowfield into which the transverse jet is injected is a unique and novel approach that permits elevated temperature and pressure conditions. A model dump combustor is used to generate and sustain an acoustically oscillating vitiated flow that serves as the crossflow for transverse jet injection studies. A fully optically accessible combustor test section affords full access surrounding the point of jet injection. High speed 10 kHz planar measurements OH PLIF and high frequency 180 kHz wall pressure measurements were performed on the injected reacting transverse jet and surrounding flowfield, respectively, under simulated unstable conditions.

6.1.1 Combustion Dynamics Rig Hardware

A schematic of the combustion dynamics transverse jet combustor hardware is shown in Figure 6.1. The combustor configuration consists of two main components: a dump combustor that generates and sustains the acoustically oscillatory vitiated crossflow, and an optically accessible transverse jet injection test section to visualize the injected jet. The dump combustor burns a premixed, preheated air and fuel mixture. Preheated air at 0.40 kg/s is premixed with ambient temperature natural gas (NG) fuel in the dump premixer, where the massflow rates of the air and the fuel are independently metered upstream of the premixer test section. The NG is issued into the premixer using a fuel peg, which is a small sealed quarter inch stainless steel tube with four 1.3 mm (0.05”) diameter holes: two pointing into and two pointing perpendicular to the incoming air flow. Four cylindrical bluff bodies in the dump premixer arranged in an alternating pattern of horizontal and vertical orientations enhance the mixing of the air and fuel. The natural gas is sourced on site and its composition is provided by the Panhandle Eastern Pipe Line Company for the Tuscola East segment. A choked orifice plate precedes the premixer. The orifice plate contains 9 square edge orifice holes with an orifice diameter of 4.42 mm and a length to diameter ratio 5.75. The orifice plate serves as a boundary condition satisfying two requirements: it provides a large pressure drop to minimize coherence between the dump combustor resonant acoustics and the premixer, and was nominally designed to provide relatively high acoustic impedance in the resonator inlet to effectively ensure high reflection efficiency, i.e. an acoustically closed boundary. Following the orifice plate, the premixed preheated flow enters the half-wave resonator section, a constant cross sectional area tube section that serves as the inlet to the dump plane of the combustor. The premixed flow enters the backward facing step dump plane, is ignited and burned. A Champion igniter is used to ignite the premixed flow, is located 0.08 m downstream of the dump plane and is turned off once ignition is achieved. Combustion is stabilized at the dump plane rearward facing step due to the recirculation zone created by the sudden flow expansion. The combustor has a constant cross sectional area of 0.0056 m^2. The combustor is terminated with a linearly converging exit nozzle with an orifice throat diameter D_t = 0.027 m. The exit nozzle backpressures the combustor to a nominal combustor pressure of 0.9 MPa, and the exit nozzle gas is exhausted directly to the atmosphere.

The dump combustor and half-wave resonator inlet are assembled from smaller length module test sections, where the lengths of both can be discretely and independently varied by either removing or adding module test sections. For the transverse jet injection studies, a module test section is replaced with a transition section and an optically accessible combustor test section, referred to as the cube, which houses the transverse jet injector. The transition section is 77 mm in length and smoothly converts the corner radii of the modular test sections to the rectangular cube cross section while maintaining a nearly constant cross sectional area to avoid any significant adverse pressure gradient. Figure 6.2 shows a schematic of the optically accessible test section. The rectangular cube cross section affords full optical access of the transverse jet injection and surrounding flowfield with three of the four cube walls containing quartz windows. The windows are 125 mm by 72 mm in the streamwise and spanwise direction, respectively, and sit flush with the inner cube surface. Full optical access of the jet injection point is afforded with this configuration. The fourth wall contains a multi-purpose and generically designed port feature that accommodates both flush mounted and elevated transverse jet injection. For data presented on the combustion dynamics rig, a flush mounted 5.8 mm exit diameter jet nozzle was used resulting in optical access of 24.9 mm upstream and 101 mm downstream of the jet orifice exit centerline. The upstream edge of the jet orifice is 163 mm downstream of the start of the cube test section. The transverse jet injector assembly consists of a premixing chamber, a choke plate, a settling plenum and the jet nozzle (see Figure. 6.2). Figure 6.6 shows a schematic of the transverse jet injector. The transverse jet is a premixed preheated 60/40 mixture of hydrogen and nitrogen, respectively. Three separately controlled and metered propellant lines feed the jet injector assembly: a primary nitrogen circuit, a hydrogen circuit and a secondary nitrogen circuit. The secondary nitrogen flow connects with the PIV fluidized bed through the use of a needle valve: for PIV testing a portion of this flow is routed through the fluidized bed, while for PLIF only testing the secondary N_2 flow bypasses the fluidized bed. The primary nitrogen circuit is heated and used to set the resultant jet injection temperature. Mixing is achieved in the premixing chamber with cylindrical bluff bodies arranged in an alternating pattern of horizontal and vertical orientations to enhance the mixing. A 6.65 mm thick orifice plate with twenty two 0.043 mm diameter holes provides a large nominal pressure drop ($dP/P - 0.56$) between the premixing chamber and the injector. This ensures that the mass flow rate from the premixing chamber is constant (i.e. only a function of the premixing chamber conditions) and therefore independent of any pressure oscillations which occur inside the jet nozzle. Downstream of the orifice plate, the orifice jets mix out in a discretely variable length circular settling plenum of constant diameter that matches the starting diameter of the nozzle contour. The discretely variable length settling plenum is designed as a tuning parameter to adjust the resonant characteristics of the injector, and for the jet studies here the plenum length was fixed at 30 mm. The circular jet nozzle has a fifth order polynomial contraction contour, a 5.8 mm diameter orifice exit, an inlet to jet exit contour area ratio of 14, and a contour length of 66 mm. The nozzle contraction contour is an academic JICF style injector used in other subsonic transverse jet research groups and is associated with a top hat velocity profile at the jet exit with a relatively small jet momentum thickness (Megerian 2007, M'Closkey 2002).

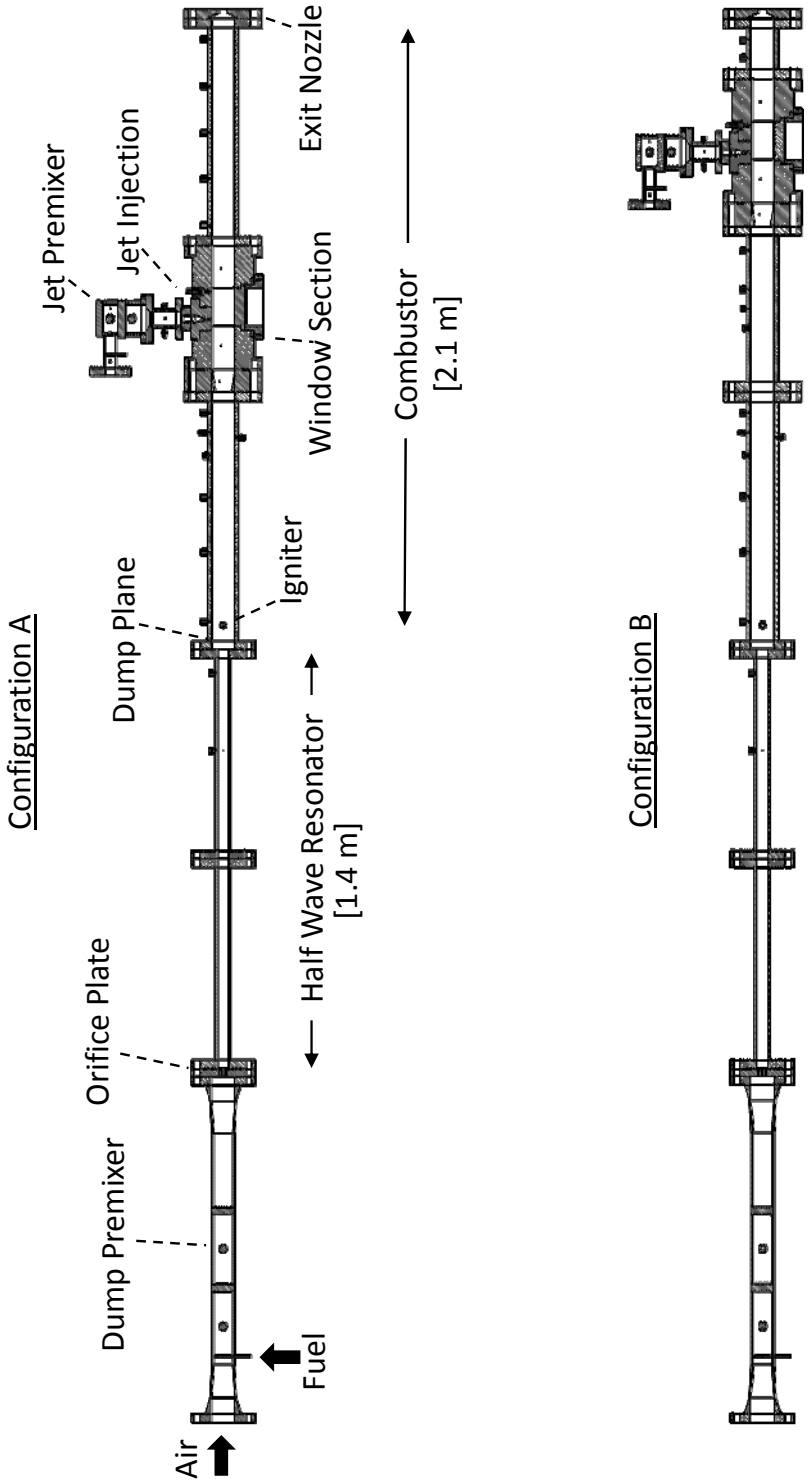

Figure 6.1 Combustion dynamics combustor configurations. The transverse jet injection is near the fundamental (near 200 Hz) pressure node (Configuration A) and anti-node (Configuration B).

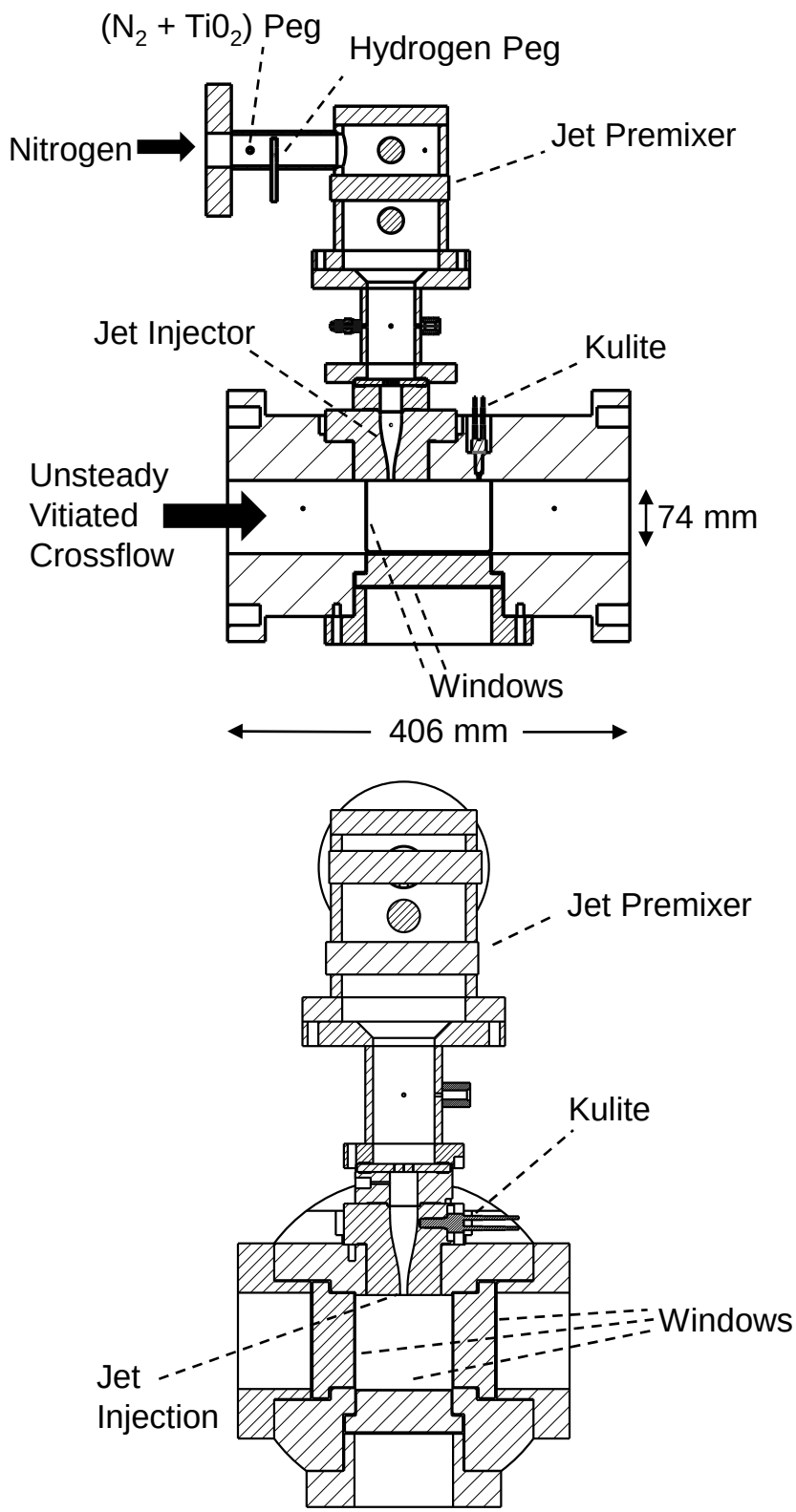

Figure 6.2 Cross sections of the optically accessible test section. Top: axial cross section. Bottom: transverse cross section.

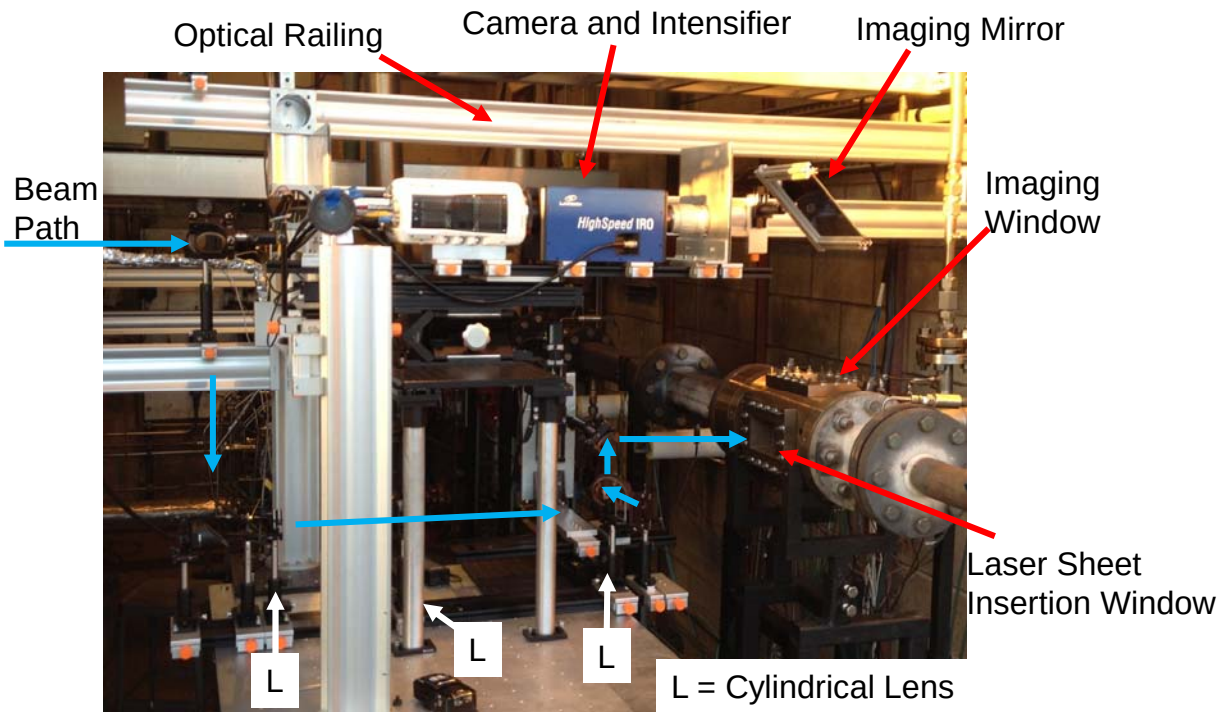

Figure 6.3 OH PLIF optical setup surrounding the optically accessible test section. This setup is for the X-Z cross sections of the transverse jet.

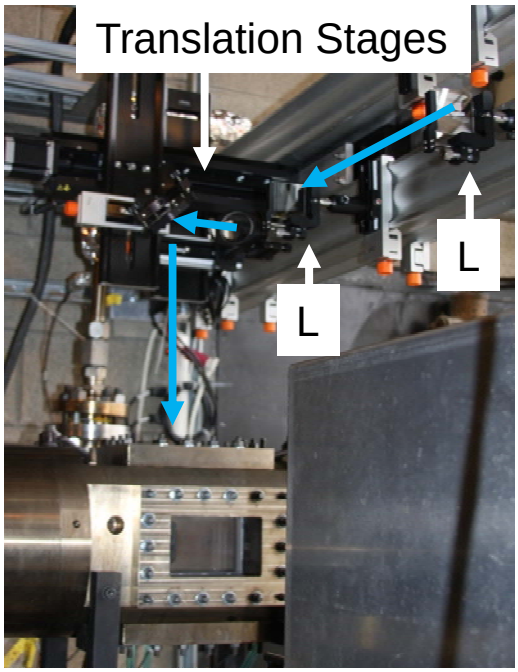

Figure 6.4 OH PLIF optical setup surrounding the optically accessible test section. This setup is for the X-Y cross sections of the transverse jet. Beam path is denoted by blue arrows.

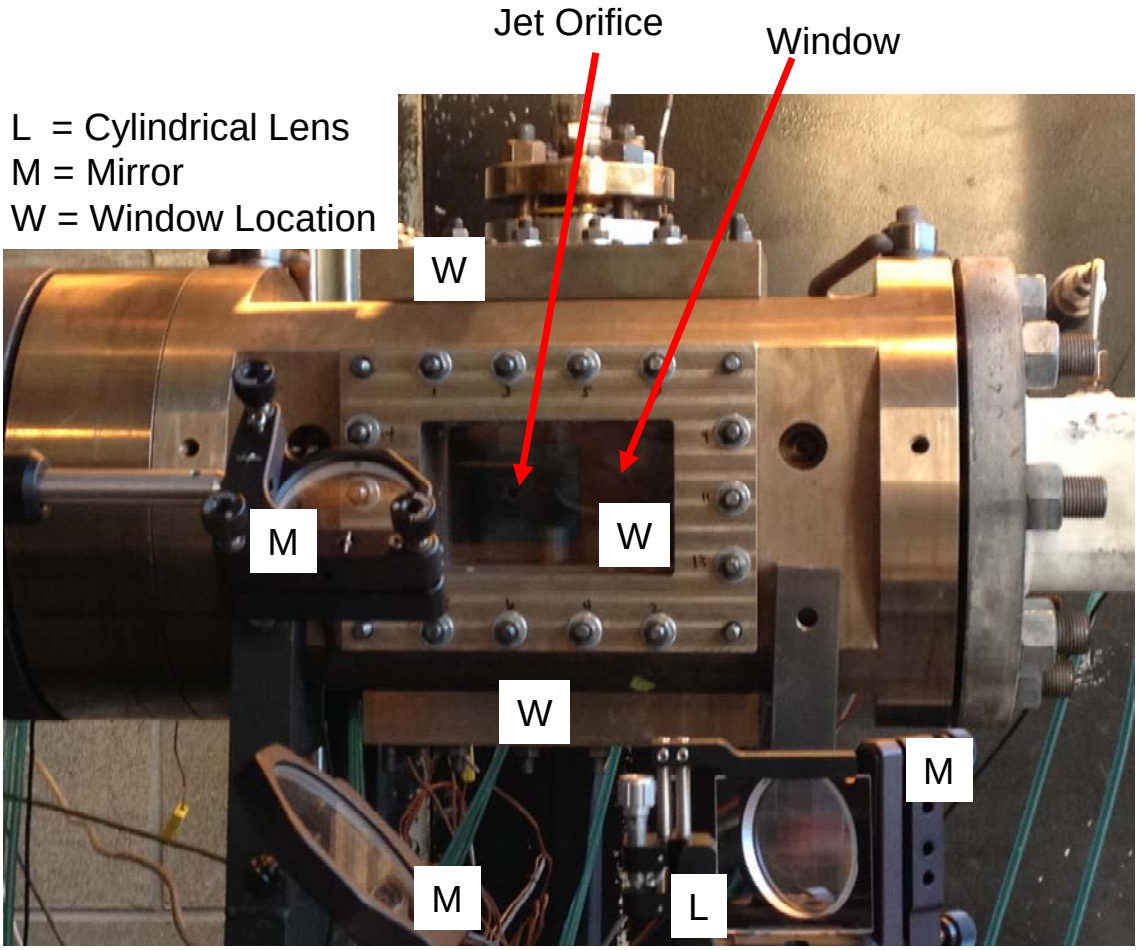

Figure 6.5. Optically accessible combustor test section on the test stand. From this perspective, the jet at the orifice exit is out of the page. This setup is for OH PLIF of the X-Z cross sections of the transverse jet.

Instrumentation and Controls

The massflow rates of all gases, including nitrogen purges, are metered using choked ASME MFC-7M toroidal sonic venturis. Mass flow rates of gases are controlled using the sonic venturi, an upstream thermocouple gas temperature measurement and a computer controlled electronic regulator (ER 3000) to set the static pressure upstream of the venturi. Nitrogen purge flows are present for the dump fuel peg, dump igniter and jet hydrogen peg, are metered using the sonic venturi method, and account for less than 1% of the dump combustor air mass flow rate. The nitrogen purges are flowing at all times for the igniter and on the three-way fuel run valves when fuel is off. Control and low frequency data acquisition at 100 Hz is performed using a labview 2012 virtual instrument (VI) program. Pressure measurements for mass flow rate calculation and system health monitoring were made using Druck PMP 1260 transducers with 0.25% full scale accuracy. Temperature measurements were made using Omega grounded type-K thermocouples with 0.75% error and are rated up to 1523 K. Analog input of pressure and temperature are signal conditioned using, respectively, and read in with the ADC PCI-6052E.

Analog output and digital output control are provided by NI PCI 6733 cards and NI PCI-6534, respectively.

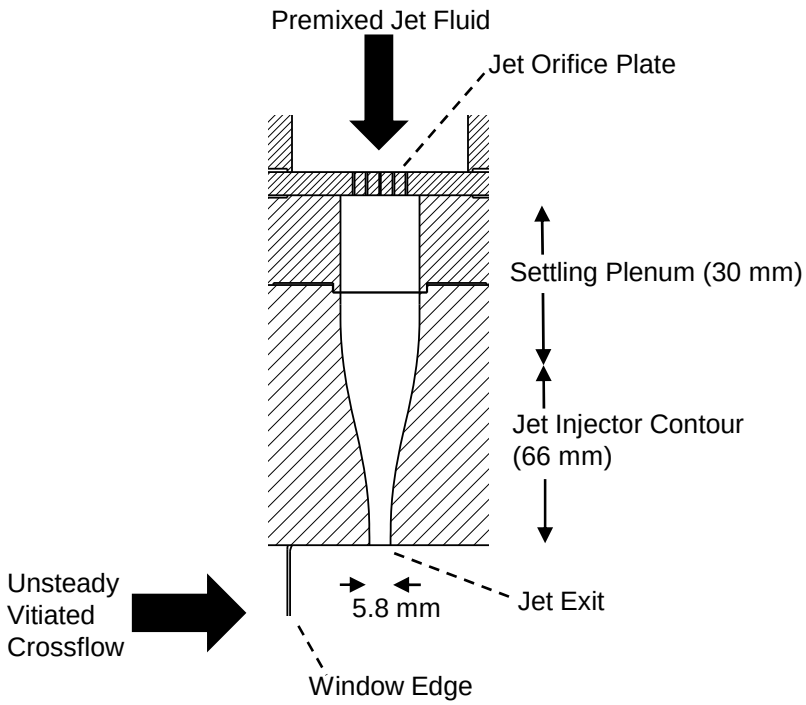

Figure 6.6. Transverse jet injector assembly.

Control and low frequency data acquisition at 100 Hz is performed using a labview 2012 virtual instrument (VI) program. Pressure measurements for mass flow rate calculation and system health monitoring were made using Druck PMP 1260 transducers with 0.25% full scale accuracy. Temperature measurements were made using Omega grounded type-K thermocouples with 0.75% error and are rated up to 1523 K. Analog input of pressure and temperature are signal conditioned using, respectively, and read in with the ADC PCI-6052E. Analog output and digital output control are provided by NI PCI 6733 cards and NI PCI-6534, respectively. The rig hardware is highly instrumented with high frequency pressure transducers (Kulite models EWCT-212M-10BARA and WCT-212M-70BARA) to spatially and temporally characterize the non-reacting and reacting gas phase acoustics. The HF transducers are wall mounted in cavities for improved survivability. The cavity design was carefully chosen to ensure the resonant characteristics of the cavity do not constructively or destructively interfere with the measured acoustics. Figure 6.7 shows a schematic of the HF transducer cavity; all cavities are designed with bulk resonant frequencies around 10 kHz, based on a 0D Helmholtz relationship and verified with an FEA analysis. The HF pressure transducers are recorded on a separate 16 channel high speed data system (DSPcon DataFlex 1000A, Control Module S/N 104024 and Analog Module S/N 105933) sampling at 180 kHz per channel. Synchronization between the HF data system and the low frequency data system is achieved with a square wave TTL pulse simultaneously sent to both data systems. Additionally, all camera triggers, frame strobes,

synchronization signals as well as laser pulse timing are phase locked (i.e. simultaneously recorded on the HF data system). For a typical test sequence, ten HF channels are reserved for the HF pressure transducers and the remaining data system channels for the imaging diagnostics timing signals.

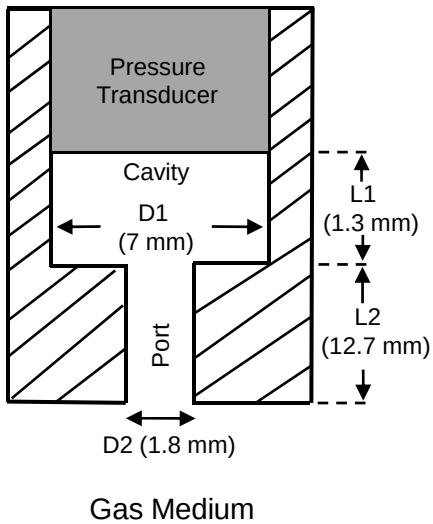

Figure 6.7. High frequency pressure transducer instrumentation port.

6.1.2 Laser Diagnostic System

The combustion dynamics optically accessible combustor test section is designed to afford increased visualization and interrogation of the reacting jet flowfield from multiple directions. Planar laser induced fluorescence of the hydroxide radical (OH-PLIF) is used to identify and characterize the reaction zones and surrounding burned gas region, and to qualitatively describe the spatial-temporal behavior of the jet structure and dynamics.

Planar Laser Induced Fluorescence System

For OH-PLIF measurements, a frequency doubled (532 nm) Nd:YAG laser (Edgewave IS200-2-L) was used to pump a tunable dye laser (Sirah Credo) operating with Rhodamine 590. The 566.7 nm output beam was frequency doubled and tuned to excite OH near 283 nm at the Q1(8) transition of (0,1) vibrational line of the A2-X2 system. The average laser pulse energy at 10 kHz was 6.10 W. The laser sheet was formed using two cylindrical lenses (f = -25 mm and f = 300 mm) resulting in a 50 mm collimated sheet height, and a third cylindrical lens (f = 750 mm) to focus the sheet. The OH fluorescence was collected perpendicular to the laser sheet using a UV sensitive lens (Cerco Sodern Type 2178, f = 100 mm focal length, f/2.8), high speed image intensifier (LaVision HS-IRO), and a high speed CMOS camera (Phantom v411). An optical band pass filter (Semrock 320/40) was placed in front of the UV lens to suppress background radiation, and a 100 ns intensifier gate width was used.

A ridged tiered optical rail structure is mounted over the combustion dynamics optical test section to accommodate up to simultaneous laser diagnostics. Adjacent breadboards accommodate additional optics and camera systems. All final turning mirrors are placed on 2-axis translational stages and utilized between tests to vary the flowfield interrogation region. Similarly, camera systems are mounted on 2-axis translational stages and travel accordingly as interrogation region changes in order to preserve camera focus.

Data Post Processing Procedure

The high frequency pressure data is analyzed post-test for frequency content by performing a power spectral density estimate using the Matlab PSD function with a hann window. Once a frequency peak is determined from the PSD, an estimate of the peak to peak pressure oscillation amplitude, i.e. p', is determined as follows: the Matlab function Butter was used to design a bandpass filter around the frequency peak from the PSD. The Matlab function filftilt implements the Butter transfer function and performs zero-phase digital filtering of the data, i.e. preserves phase information. Raw pressure data is compared against bandpass filtered pressure data to ensure that phase and amplitude are accurately captured. All filter parameters are fixed for the data analysis. After recording a set of high speed images, the images are converted from raw pixels to engineering units using a dot target calibration procedure. The calibration is performed using a LaVision Type 5 dot target and the LaVision calibration software. Additionally, the dot target calibration corrects for minor angular misalignments between the camera and the test article that are still present despite a careful setup of both. This is especially important so as to minimize any spatial bias of the jet structures. Images are averaged on a pixel basis to determine the location and size of mean jet flowfield structures. Additionally, dynamic mode decomposition (DMD) analysis is used to identify and track dynamic coherent structures in a sequence of OH PLIF images. DMD is an extremely useful data processing technique that permits reduction of extremely large experimental datasets to much more manageable reduced order descriptions of the fluid flow. DMD identifies the dominant frequencies and associated spatial modes shapes contained in the image dataset. This technique permits decomposition of an OH PLIF dataset into jet responses as a function of time (i.e. frequency). The DMD method implemented here is derived from Schmid (Schmid 2010).

Combustion Dynamics Rig Acoustics

The half-wave resonator inlet section in combination with the dump combustor is designed to provide combustion-driven axial instabilities at frequencies determined by the overall length of the chamber. The combustor design was formulated using a quasi-one-dimensional linearized Euler solver, LEE, to predict longitudinal acoustic mode shapes and frequencies for a given geometry and set of gas properties (Yu 2010). This configuration results in a self-excited thermoacoustically unstable dump combustor that generates harmonic acoustic oscillations superimposed on the mean vitiated combustor crossflow. For this study, the dominant unsteady crossflow resonant acoustics in the combustor are the 2L (near 200 Hz) and its harmonic 4L (near 400 Hz). The oscillation amplitude and dominant modes relative to one another are manipulated by varying the combustor geometry, e.g. inlet resonator length, and dump combustor inlet operating conditions. The dump combustor inlet operating conditions used

for manipulation of the chamber acoustics are the inlet preheated air temperature and the dump plane equivalence ratio.

Figure 6.8 shows typical instantaneous and averaged pressure mode shapes for the 2L, 4L and 6L acoustic modes, where for convenience a sinusoid solid line has been drawn over the data points to make the highlight the mode shape. Due to the self-excited nature of the dump combustor, the 6L (near 600 Hz) is occasionally present along with the 2L and 4L, but is typically at lower amplitude. Starting at the dump plane, the top plots show one pressure node and two anti-nodes out of phase relative to one another by T/2; this is the 2L mode of the dump combustor and inlet resonator combination. Starting at the dump plane, the 4L mode contains two nodes and three anti-nodes, and the 6L mode contains three nodes and four anti-nodes. While the 6L will naturally and occasionally sprout up in the chamber, data post processing will focus on time slices where the 6L is minimal. The 2L and 4L are the dominant chamber crossflow acoustics. The locations of transverse jet injection for this study are 1.12 m and 1.68 m from the dump plane: the location 1.12 m is close to the 2L node and 4L anti-node, and the location 1.68 m is close to the 2L anti-node and the 4L node. By changing the axial location of the transverse jet injection, the jet can be introduced at different locations in an acoustic pressure mode shape in the combustor, e.g. the jet can be injected at a pressure node or a pressure anti node. This strategy permits separate investigations of the jet structure and dynamics in response to a local pressure anti node flowfield (corresponding to a velocity node) and local pressure node flowfield (corresponding to a velocity node) near the point of transverse jet injection. The injector nozzle cavity will have natural acoustic resonances associated with it that are a function of the geometry, gas properties, and boundary conditions. These natural resonances are unavoidable and have the potential to bias the response of the transverse jet to the crossflow forcing events. Therefore, the injector geometry and gas properties are strategically chosen to avoid overlap with the crossflow frequencies and those associated with the JICF dynamics, e.g. jet shear layer rollup. An FEA acoustic analysis was run to meet this objective and Table 1 shows the resultant jet conditions chosen for this study. The bulk Helmholtz style resonance of the injector is calculated to be 671 Hz, which is half way between the combustor 6L and 8L acoustics. This ensures minimal overlap. Pressure and image data analyzed during post processing displays an occasional ~670 Hz injector resonance, but is not consistently excited and displays orders of magnitude lower power in the calculated pressure or image spectra.

Testing Sequence

The combustion dynamics transverse jet rig is not a continuously combusting test rig and reacting flow hot-fire tests are performed over a short duration, nominally 15-30 sec. This significantly reduces the cost of design and manufacturing of a model combustor since active cooling of hot combustor parts is unnecessary for short durations. Also in this manner, between tests the large gigabyte sized image sets (typically 15-20 GB per test) are transferred off of the cameras in preparation of the next test. Figure 6.9 shows a typical testing sequence. At 0 s preheated air at the set test condition (massflow and temperature) flows through the rig, preheating the combustor to approximately the air temperature. During this time, the transverse jet fluid consists only of the nitrogen at the set test condition. At 2 s, the transverse jet hydrogen run valve is actuated and all jet feed line and manifold pressures are allowed to become steady before crossflow ignition occurs. At 5 s the dump plane igniter is turned on and at 6 s the dump combustor fuel natural gas run valve is actuated. Once dump combustor ignition is confirmed (7

s), the igniter is turned off and the crossflow and transverse jet fuel run valves are left open for an additional 11 s to ensure chamber pressure and temperatures steady off. At 18 s, the camera systems are triggered and images are recorded of the reacting transverse jet in an unsteady crossflow. Once the imaging is complete, the dump combustor fuel run valve is closed (22 s) followed by the closing of the jet hydrogen run valve. At this time, the combustor continues to flow preheated air in the crossflow, and the targeted nitrogen flow rate through the jet.

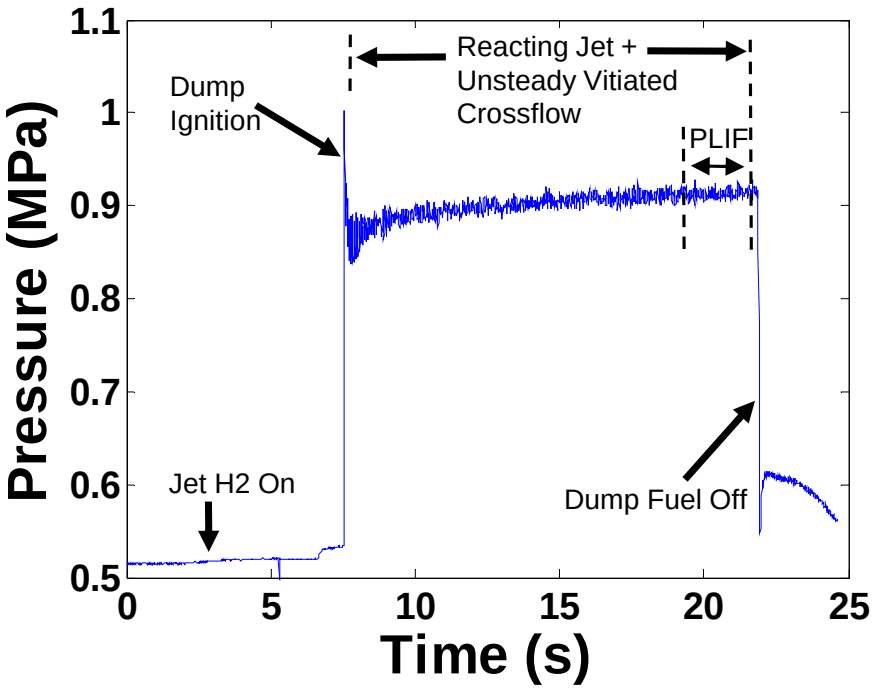

Figure 6.9. Dump combustor pressure trace for a typical test sequence for the reacting jet injected in an unsteady crossflow using the combustion dynamics rig configuration.

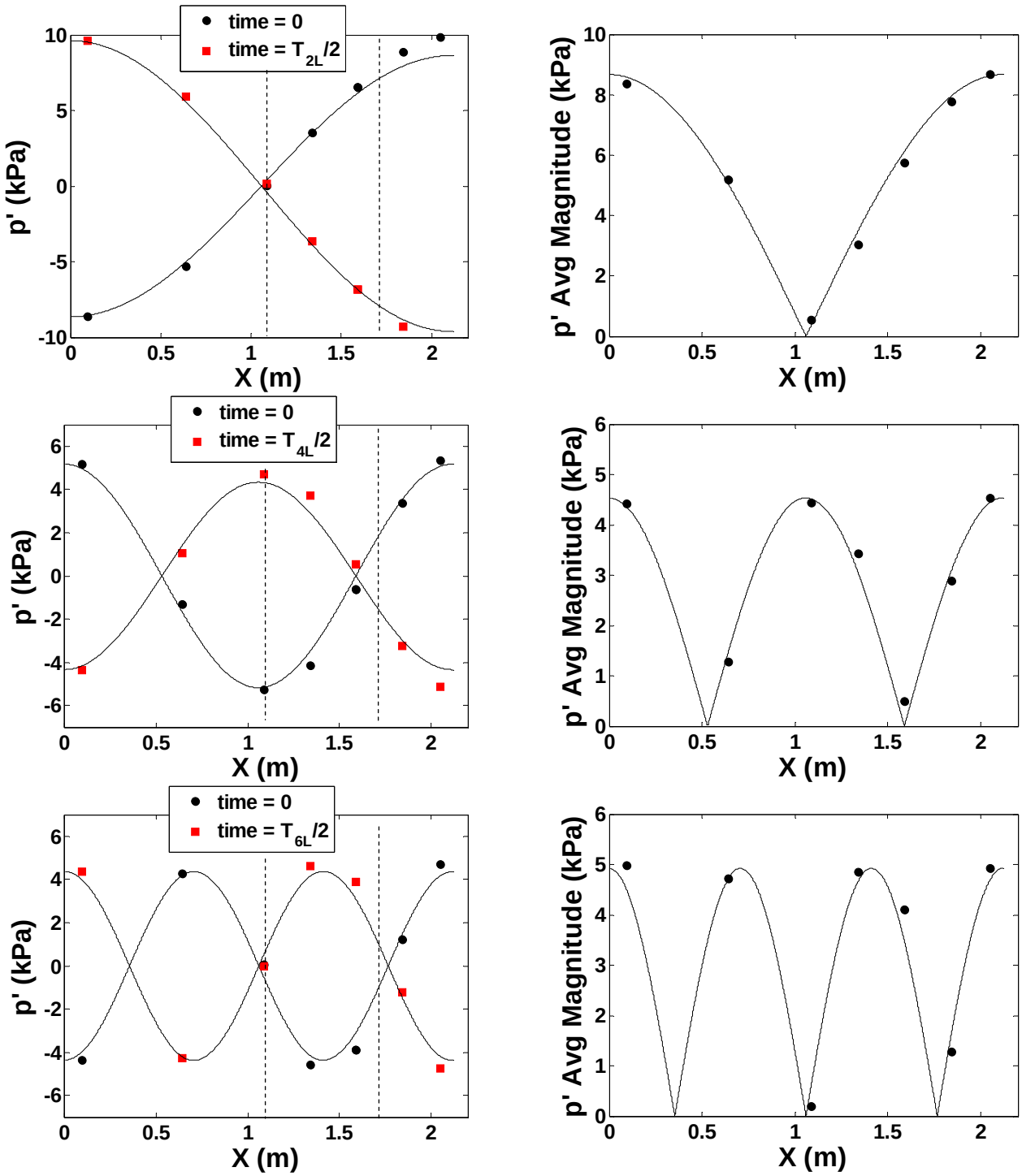

Figure 6.8. Spatial mode shapes for chamber 2L (top), 4L (middle) and 6L (bottom). Instantaneous (averaged) mode shapes are shown on the left (right). Dotted vertical lines represent configuration A and B jet injection locations. For data shown here, the 2L, 4L, and 6L acoustic modes correspond to 195 Hz, 389 Hz, and 579 Hz. X = 0 m represent the dump plane and X = 2.1 m is the chamber exit nozzle.

6.1.3 Results and Discussion

The combustion dynamics JICF studies at Purdue under the UTSR program have focused on 60/40 hydrogen/nitrogen fuel transverse jets. High speed 10 kHz OH PLIF on the reacting transverse fuel jet was performed simultaneously with 180 kHz high frequency pressure measurements in the jet injector and throughout the crossflow flowfield. For the OH PLIF tests, focus was placed on cross sectional slices of the jet core to investigate the structure and dynamics of the reacting shear layer between the vitiated crossflow and the fuel jet. Figure 6 shows a transverse jet injection schematic highlighting side and top views of the jet and the cross sectional OH PLIF planes.

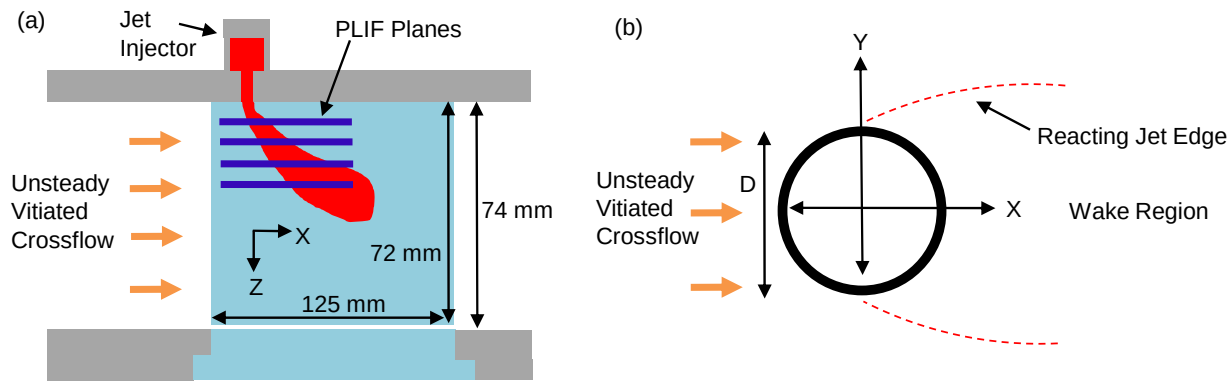

Figure 6.10. (a) Schematic diagram of the side view of the jet injection highlighting PLIF planes (purple) and window layout (blue). (b) Schematic diagram of top view of jet injection where the jet is coming out of the page. For both (a) and (b) the crossflow is from left to right.

Transverse jet structure and dynamics scale with parameters (not inclusive) J, Re, density ratio, forcing frequency and forcing amplitude. To constrain the rich JICF behavior and focus on the crossflow unsteadiness on an injected jet, certain jet and crossflow parameters were fixed. Table 1 shows the jet and crossflow conditions held constant for the OH PLIF study.

Table 6.1. Nominal (mean) fixed conditions for the combustion dynamics study

J (Jet to Crossflow Momentum Flux Ratio)	6
Jet Orifice Exit Diameter	5.8 mm, round
Jet Total Massflow	0.016 kg/s
Jet Mixture	60/40 H_2/N_2 Mixture
Jet Re	90000
Jet Mixture Temperature	370 K
Jet Exit Velocity	80 m/s
Crossflow Air Massflow	0.4 kg/s
Crossflow Chamber Pressure	0.9 MPa
Crossflow Re	47000
Crossflow Velocity	50 m/s

In total, two cross sectional interrogation angles on the jet were performed: the X-Z and X-Y cross sections. For the X-Z cross section, one plane was interrogated with the PLIF sheet

centered on Y/D = 0 and extends in the Z direction (see Figure 6.10). Z is measured from the injection wall (i.e., the jet injector is located at Z = 0) This angle affords visualization of the jet trajectory, jet flapping, and coherent jet structure rollup (e.g. jet shear layer rollup). For the X-Y cross section, planes at Z = 2 mm, 4.8 mm, 9.8 mm, 14.8 mm, 19.8 mm were performed for Figure 1 configuration B, and for Z = 2 mm, 4.8 mm, 9.8 mm, 14.8 mm, 19.8 mm, 24.8 mm, 29.8 mm and 34.8 mm Figure 1 configuration A. Repeat tests for all conditions are performed and multiple amplitude levels of crossflow acoustic content are investigated. As a summary, this report highlights three test cases containing salient features of the jet nearfield that describe common coherent structures and dynamics for a reacting 60/40 H_2/N_2 transverse jet injected into an acoustically oscillatory vitiated crossflow. The nearfield is loosely described here as within a distance of approximately seven jet diameters from the jet exit. The OH PLIF two inch optics constrains the sheet width to a two inch maximum and therefore this affords good nearfield visualization. Data processing of the data continues to this day and multiple journal publications are in preparation.

Test Case A

Figure 6.11 shows a sequence of unfiltered OH PLIF images at 10 kHz for the X-Y cross sectional plane located at Z = 4.8 mm or Z/D = 0.83, where the axes are scaled by the jet diameter D = 5.8 mm. The jet orifice location is indicated by the white circle centered at the coordinates (X/D,Y/D) = (0,0), and the colorbar indicates the pixel intensity, where the images were recorded using 12 bit pixel depth for a 0 to 4095 scalar range for pixel intensity. For test case A, the crossflow dump plane equivalence ratio is 0.64 and corresponds to an adiabatic flame temperature of 1900 K as determined using Chemical Equilibrium with Applications (CEA) for a 660 K preheated natural gas and air mixture. Test case A corresponds to combustor configuration B in Figure 6.1. The location of the reacting jet edges, i.e. flame front, are marked by sharp intensity gradients in the OH fluorescence signal in the vicinity downstream of the jet exit, e.g. see red arrows in frame 2 and 5 in Figure 6.11. Regions of speckled intensity values surrounding the reacting jet edges are due to OH fluorescence of the vitiated crossflow, e.g. see frame 3 red arrow in Figure 6.10, and not of a background chemiluminescence. This is confirmed to be the case since imaged regions upstream and downstream of the PLIF sheet are on the order of 0 to 20 pixel counts (making up the background vitiated crossflow chemiluminescence) as compared to the speckled regions which are on the order of 200-400 counts. For reference, the sharpest gradients in the flame front approach 3000 counts. Additionally, the images show concentrated intensity regions periodically manifesting near Y/D = 0 and over a range of X/D, e.g. see red arrow in frame 11 in Figure 6.11. These regions typically display more coherence in intensity as compared to the speckled regions, and are not defined by a thin sharp gradient that would define the flame front. Therefore, these regions appear to be burned gas wake regions of the reacting jet.

Characteristics of Phase Locked Imaging with Pressure

The sixteen sequential images in Figure 6.11 at 10 kHz cover only 1.6 microseconds and from frame to frame show relatively minor bulk structure evolution that can be tracked. For example, see structure development from frame 1 to frame 3, particularly the X/D length of the overall structure highlighted by the green arrow. It is important then to consider the time scales of the crossflow acoustics relative to the 10 kHz imaging rate and the evolution of jet structures.

For this, the phase locked high frequency pressure measurements are compared to the images. For a 200 Hz cycle, there are 50 recorded images, and similarly for a 400 Hz cycle there are 25 recorded images. Relative to Figure 6.11, 16 frames corresponds to approximately 1/3 of a 200 Hz cycle and 2/3 of a 400 Hz cycle. The crossflow acoustics are generally nearly linear (see Figure 6.8) and the changes in the crossflow at the 200 Hz and 400 Hz frequencies are typically expected to occur gradually at each respective frequency as opposed to sudden and sharp compression waves at a given frequency typically observed in larger amplitude and nonlinear acoustic resonances. Therefore, it is not unlikely that as the crossflow gradually modulates at 200 Hz, the jet trajectory in response changes due in part to a changing crossflow momentum flux (the acoustic velocity fluctuations effectively modulating the instantaneous crossflow velocity) and the jet momentum flux due in part to the temporally oscillating pressure locally at the point of injection (effectively modulating the injected pressure gradient and therefore the jet exit velocity). Figure 6.12 shows both unfiltered and bandpass filtered pressure traces at a location 89 mm upstream of the jet injection over the period of images corresponding to Figure 6.11. The raw pressure shows a coherent and dominant oscillation frequency near 200 Hz and is confirmed with a PSD estimate to be 195 Hz (not shown). Also shown in Figure 6.11 is the bandpass filtered pressure at 195 Hz (2L), as well as the location of the phase locked imaging in relation to the pressure. For the duration covering 16 frames in Figure 6.11, this pressure location moves from an acoustic rarefaction to a compression. The jet injection location for configuration B is downstream of the pressure node and close to the pressure anti node. Since the jet injection location is between a node and antinode, the jet is expected to display both a pressure based and a velocity coupled dynamic response. At 195 Hz, this pressure location moving from a rarefaction to compression near a pressure anti node can signify pumping of the jet fluid by the crossflow due to the fluctuating pressure locally at the point of jet injection. It can also signify a velocity coupled jet response of the jet: the rarefaction to compression produces a crossflow velocity fluctuation that lags the pressure by ¼ of a period. Interestingly, both a pressure and velocity crossflow perturbation help to explain the raw images.

From figure 6.11: (i) the first eight image frames shows a lengthening of the flame front in X/D (ii) these eight image frames are phase locked with a rarefaction to start of compression process where an increase in pressure decreases the pressure gradient of the jet to crossflow (iii) simultaneously, the crossflow velocity begins to increase as the pressure increases and results in a further decrease of the jet to crossflow momentum flux ratio thereby driving the jet trajectory closer toward the injection wall. Due to the planar imaging of OH and as the jet trajectory penetrates more and less into the crossflow, the cross sectional imaging captures different slices of the jet as a function of time. Moreover, Figure 6.13 shows additional unfiltered raw images and the frame locations for the back half of the 195 Hz cycle relative to the images in Figure 6.11. In particular, frames 27 and 51 at a compression and rarefaction, respectively, display lengthened and shortened jet flame structures, respectively. This suggests the jet is responding to the fluctuating pressure gradient by penetrating more or less as a function of the local instantaneous pressure.

Time Averaged OH PLIF

An average of the OH PLIF images of the jet provides a characteristic picture of the spatial shape of the unburned jet fluid and the burned gas wake regions. Figure 6.14 shows an

average of 2000 consecutive frames spanning 0.2 sec (corresponds to 40 cycles of a 200 Hz frequency) for test case A. The average is defined on a pixel basis and normalized by a fictitious pixel with a temporal intensity value of 20% the maximum intensity value of 4095. This was done to convey any notable and clear mean jet structures. Characteristic of the jet at the cross sectional plane Z = 4.8 mm, there is a bifurcated low intensity lobed structure immediately downstream of the jet. The lobed, kidney shaped structure is symmetric about Y/D = 0 and extends from X/D ~ 0 to as far as X/D = 2. The upper and lower halves of the kidney structure are surrounded by a thin layer of higher intensity and encompass a central region with relatively high intensity. For X/D > 2, there are larger regions of bulk OH mean concentration that make up the dynamic portions of the jet farther from the jet exit; in the average, this region is smeared without definable features due to the flame front fluctuating back and forth across this region. The relatively lower intensity region between 2.25 < X/D < 3.5 is due to the OH PLIF sheet nonuniformity and has not been corrected for in the data processing. From Figures 6.11, 6.13, and 6.14, the kidney shaped structure is a result of the instantaneous, i.e. 10 kHz imaging, winged structures immediately downstream of the jet exit that increase and decrease in length. The central region near (Y/D, X/D) = (0,2) is then the location at which the winged flame structures appear to collide in the plane. However, this is not definitive. Due to the jet flapping, this may be the recirculation zone moving into and out of the cross sectional plane.

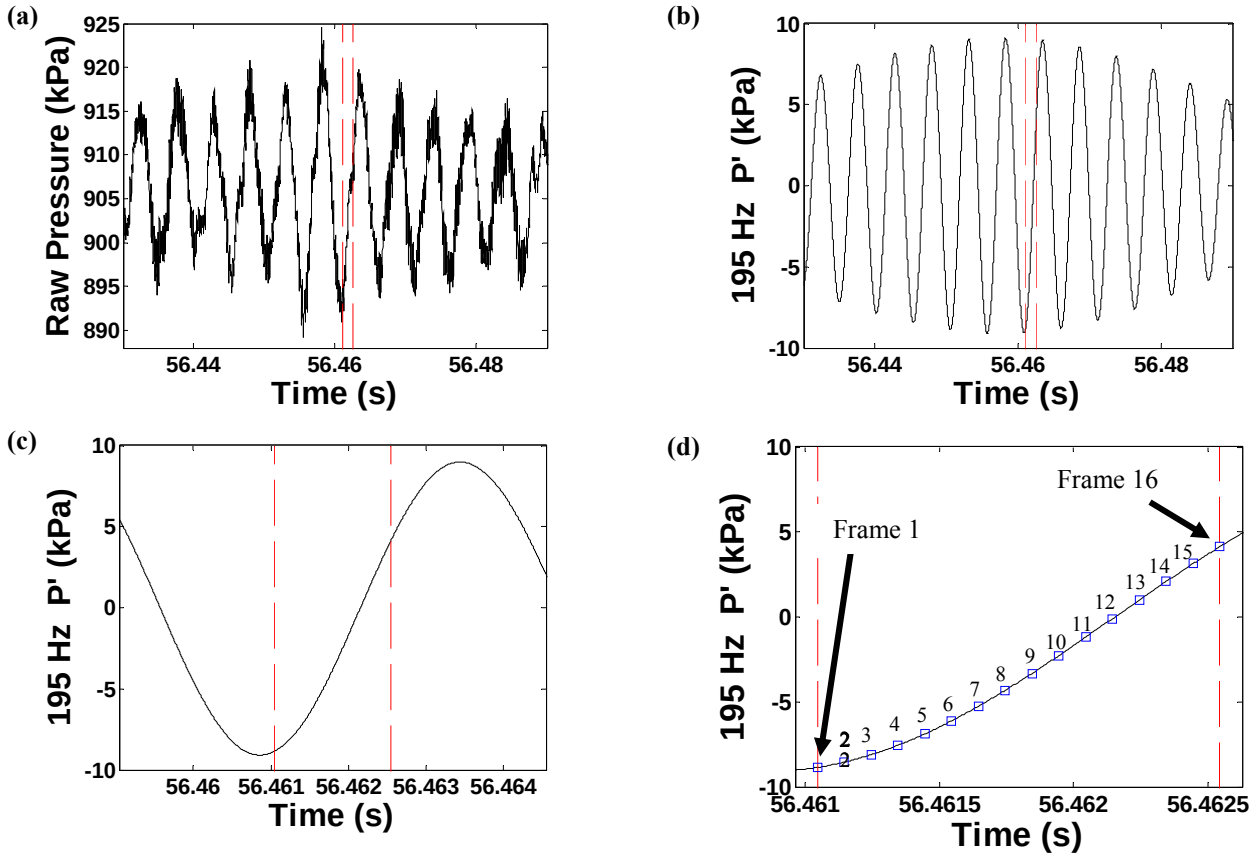

Figure 6.12. Pressure phase locked with Figure 6.11 images, where red vertical lines demarcate the time period of the 16 frames. (a) Unfiltered pressure trace. (b) Bandpass filtered pressure at 195 Hz, where plot (c) shows a zoomed in view. (d) Detailed view showing location of Figure 6.11 frame relative to pressure signal. Pressure transducer is located in the crossflow 89 mm upstream of jet injection.

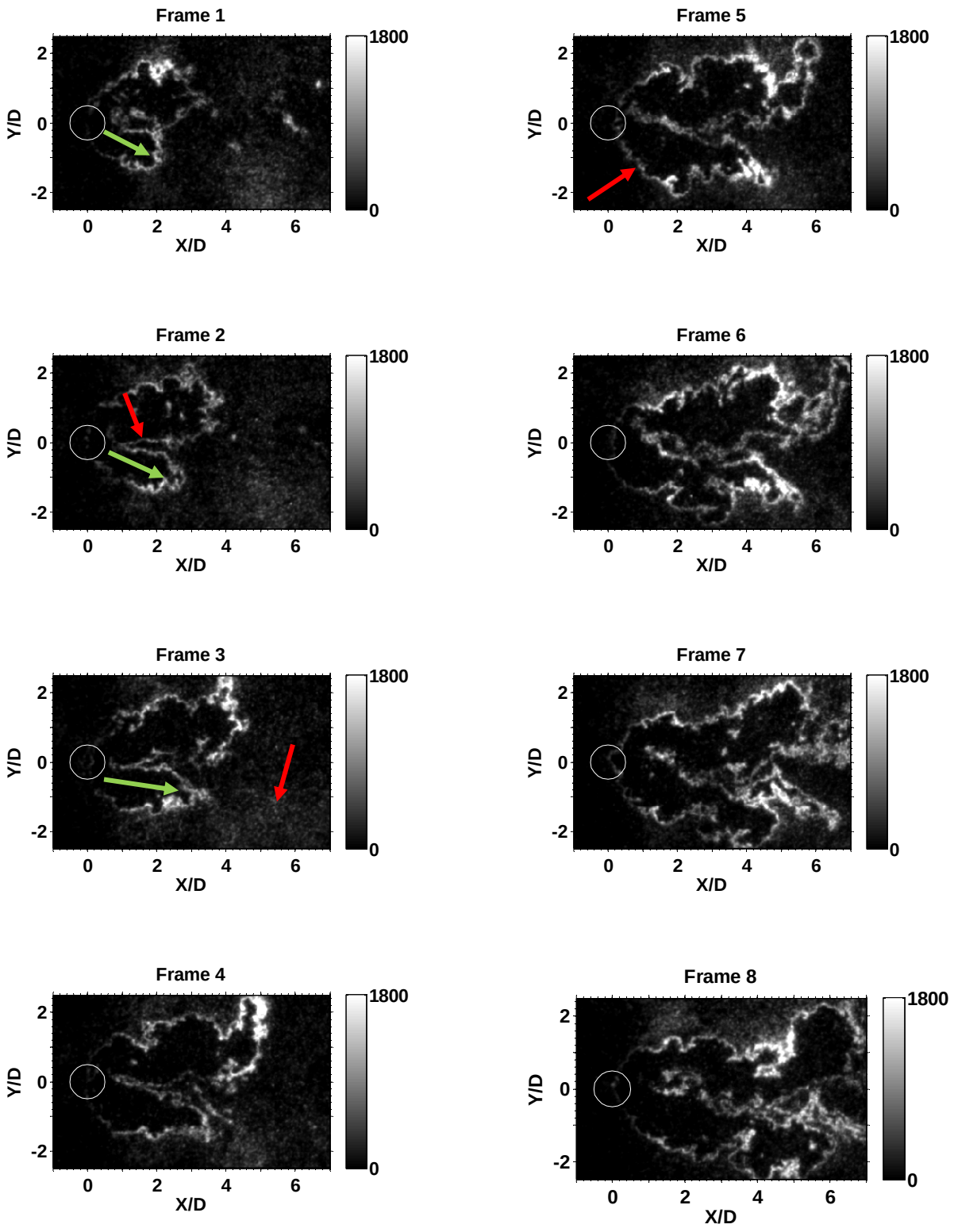
Frame 1
Frame 2
Frame 3
Frame 4
Frame 5
Frame 6
Frame 7
Frame 8
Y/D
X/D
2
0
-2
0
2
4
6
1800
0

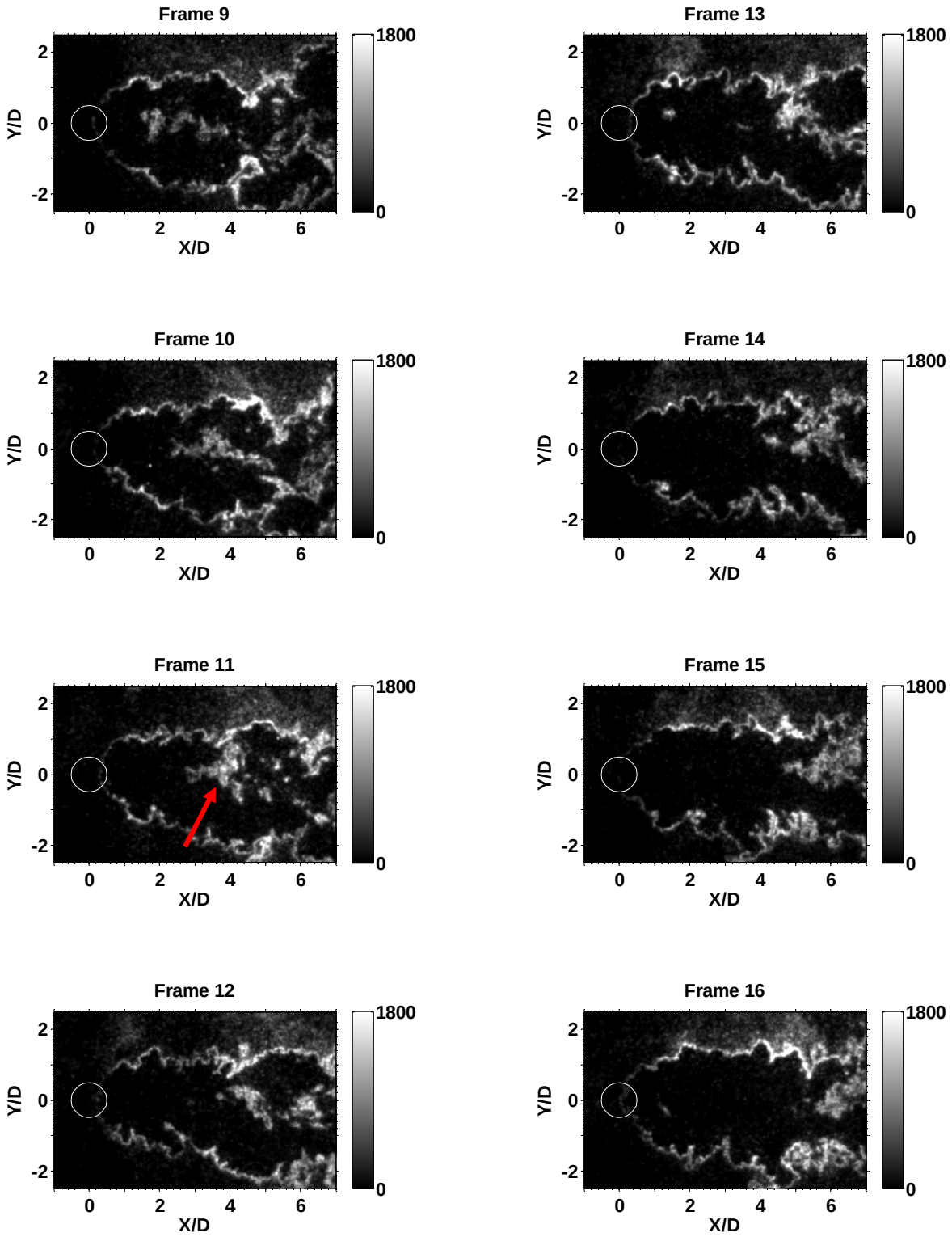

Figure 6.11. Sixteen consecutive 10 kHz OH PLIF images for plane z = 4.8 mm. The jet orifice is represented by the circle at (0,0), axes scaled by jet diameter, and the crossflow is left to right.

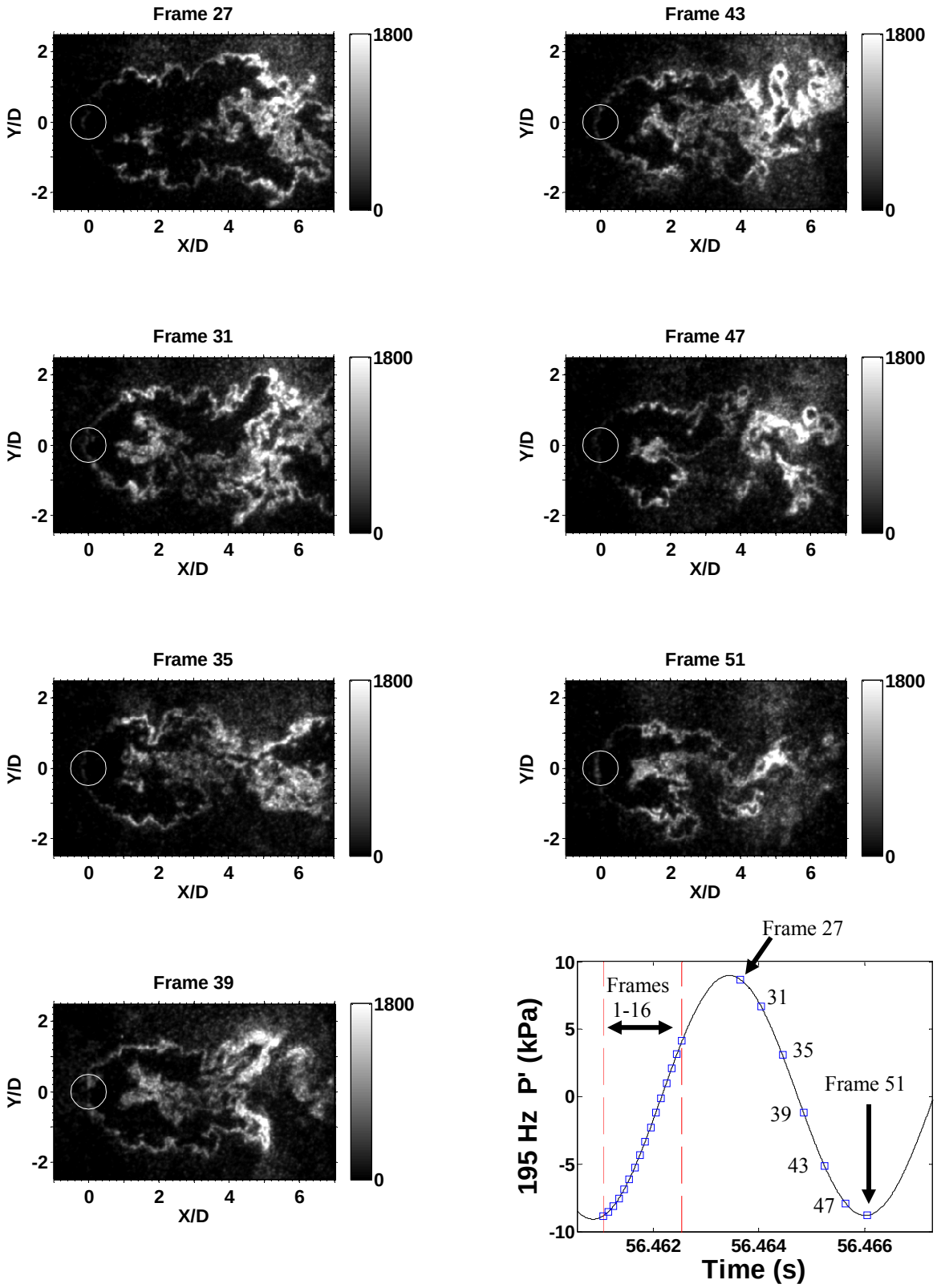

Figure 6.13. Plane Z = 4.8 mm showing every fourth image for a compression to rarefaction. These images preceed Figure 6.11 images and identified in the bandpass filtered pressure plot.

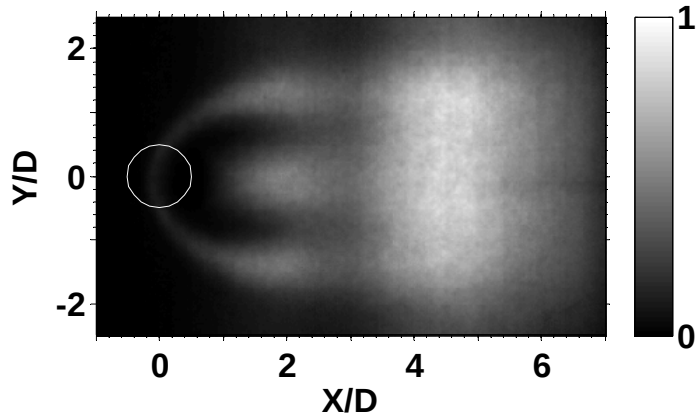

Figure 6.14. OH PLIF average at plane Z = 4.8 mm.

Dynamic Mode Decomposition Analysis

Dynamic mode decomposition (DMD) was applied to test case A. DMD provides frequency information and spatial structure of the dominant and most coherent structures that make up the jet evolution observed in the OH PLIF images. Figure 6.15 shows the DMD calculated power spectra for case A at the cross sectional plane Z = 4.8 mm for 2000 consecutive frames. Over the 2000 frames duration, there are multiple frequency peaks found from the DMD analysis. The dominant frequencies are 190 Hz and 385 Hz, with minor frequencies near 50 Hz, 100 Hz, 550 Hz and 765 Hz. Some of the minor peaks are typically observed in the crossflow acoustic spectra; this is not unexpected since the dump combustor is naturally self-excited and typically contains low level amplitude acoustics at many frequencies.

The dominant DMD frequencies (190 Hz and 385 Hz) in Figure 6.15 are identical to the dominant crossflow acoustic frequencies found in Figure 6.16 (195 Hz and 382 Hz), where the actual numeric difference is attributed to differing temporal resolutions (10 kHz images vs 180 kHz pressure) for a set period in time (2000 frames = 0.2 s). Over the 0.2 s duration, Figure 6.16 shows the 195 Hz mode as the nearly dominant crossflow frequency. Considering the acoustic mode shapes of the crossflow frequencies, the injector is placed near the 382 Hz pressure node node and 195 Hz pressure anti node. This is confirmed for this time period by comparing Figure 6.16 (a), (b) and (c) for the 382 Hz bandpass filtered pressure. At the exit nozzle of the combustion chamber, the 382 Hz is near its anti-node location, but for locations at and around the point of jet injection, the 382 Hz is near its pressure node. Figure 6.15 shows a dominant 385 Hz and Figure 6.16 shows a dominant 195 Hz, suggesting that the jet is responding more dynamically to the velocity based crossflow fluctuations rather than the pressure based crossflow oscillations. At the point of jet injection, the jet injector is near the 385 Hz pressure node, i.e. a velocity anti-node. Here, the 385 Hz spatial pressure gradient is large and since the linearized velocity perturbation is proportional to the spatial pressure gradient, the corresponding velocity oscillation can become significant. Additionally, the jet injector is near the 190 Hz anti node and

while it is between the pressure node and antinode in actuality, the spatial pressure gradient is not as severe for the 190 Hz mode as compared to the 385 Hz mode. Thus the 190 Hz mode can create lower velocity amplitude fluctuations for the same acoustic magnitude as the 385 Hz. Oppositely, the jet structure response can be particularly sensitive to fluctuations in the crossflow velocity as compared to fluctuations in the pressure at the point of jet injection and the hypothesis that the jet is responding strongly to the 190 Hz pressure fluctuation and not as much to the 190 Hz velocity fluctuations is evidence of this. The DMD spatial modes for 385 Hz and 190 Hz are shown in Figures 6.17 and 6.18, respectively. These correspond exactly to frames found in Figure 6.11 and highlight the dynamic nature of the jet flame front. Figure 6.17 shows frame 1 to frame 28, where at 385 Hz is nearly one complete acoustic cycle (10 kHz/385 Hz = 26 frames/cycle). This is indeed the case where frame 28 appears as the start of a new cycle in comparison to frame 1. In the case of 190 Hz in Figure 6.18, 28 frames corresponds to approximately 53 frames therefore making the frame sequence in Figure 6.18 approximately one half period of 190 Hz. Figure 6.19 shows the crossflow pressure at the pressure antinode of both frequencies (downstream of the jet injection location) highlighting the location of each frame relative to bandpass filtered pressure. In the case of the DMD 385 Hz mode, there is a rarefaction at the pressure antinode during frame 1. Between frames 1, 4, 8, and 12, the pressure moves from a rarefaction toward a compression and during this time the crossflow flowfield surrounding the injection location is accelerating and gaining velocity in the +X streamwise direction. During this time, the DMD 385 Hz mode in Figure 6.17 shows a region of high intensity centered on (Y/D, X/D) = (0,2) stretching and subsequently moving in a piecewise fashion in the +X direction. Oppositely, over frames 16 to 28, the 382 Hz crossflow acoustic moves from a compression to a rarefaction, generating acceleration and velocity against the mean vitiated flow and the movement of the dynamic structure upstream. The effective role the 382 Hz crossflow acoustic mode plays is to modulate the crossflow flowfield velocity and acceleration surrounding the point of jet injection, which appears to be partially responsible for the apparent lengthening and contraction of flame front as observed in Figure 6.11 raw images.

In the case of the DMD 190 Hz mode, the 28 frame period shown in Figure 6.18 corresponds to the crossflow moving from a rarefaction to a compression, i.e. only one half of the acoustic cycle. At the rarefaction, the higher than average jet pressure gradient contributes to a high momentum flux of the jet and thus a higher J. At frame 1, the rarefaction produces a small jet structure size above the mean intensity and directly downstream of the jet orifice. As the rarefaction becomes a compression, the structure is moved from being centered on (Y/D, X/D) = (0,2) to past X/D > 4. The effective role the 195 Hz crossflow acoustic mode plays is to fluctuate the crossflow flowfield pressure surrounding at the point of jet injection, which appears to be partially responsible for the apparent lengthening and contraction of flame front as observed in Figure 6.11 raw images as the jet momentum flux changes in response to a changing pressure gradient. These DMD images also align with the 190 Hz crossflow velocity fluctuation. Therefore, both the pressure and velocity fluctuations at 190 Hz appear to play a complimentary role in the jet dynamics. Additionally, it is interesting to note that the two simultaneous crossflow frequencies (190 Hz and 385 Hz) appear very much in synchronization in regards to tending to cause the jet to either instantaneously bend more or penetrate further into the crossflow.

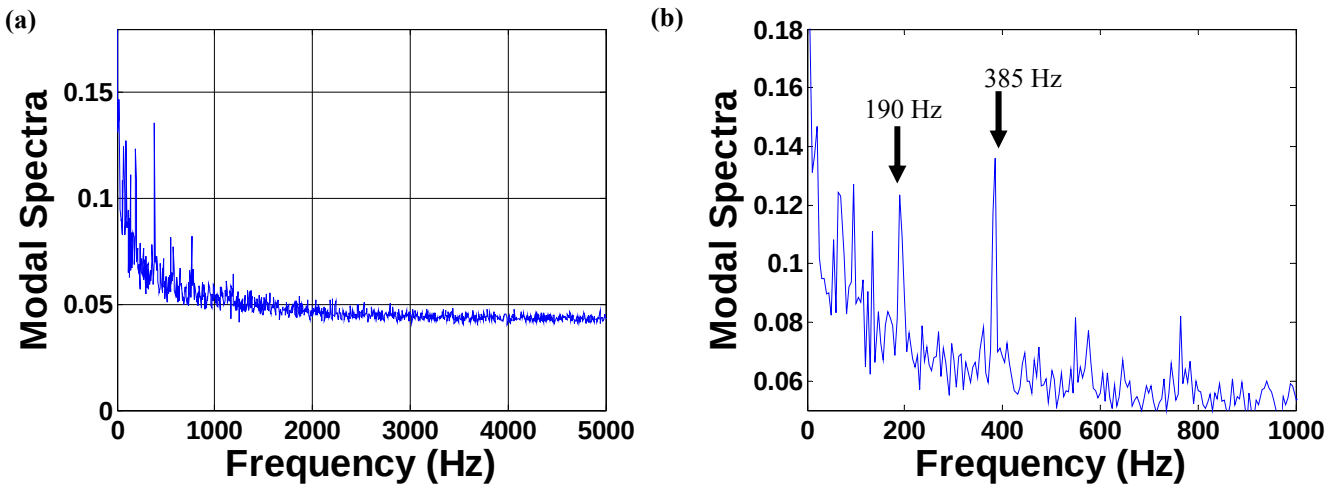

Figure 6.15. Dynamic mode decomposition power spectra for case A for 2000 consecutive frames. (a) Plot highlighting the absence of frequency content above 1 kHz. (b) Shows dominant frequency content present over the given period.

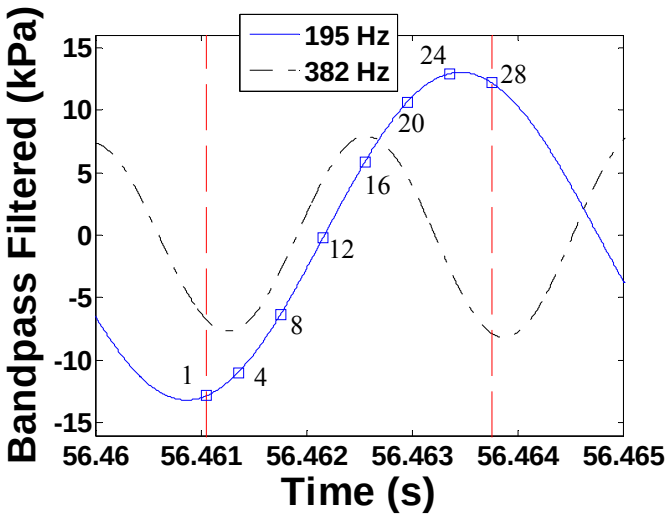

Figure 6.19. Bandpass filtered pressure near pressure anti-node of both 195 Hz and 382 Hz crossflow acoustic modes. Red vertical lines demarcate the time period of frame 1 – 28 of Figure 6.16 and Figure 6.17. The pressure measurement is in the crossflow location 70 mm upstream of exit nozzle and square data points are only drawn on one curve for clarity.

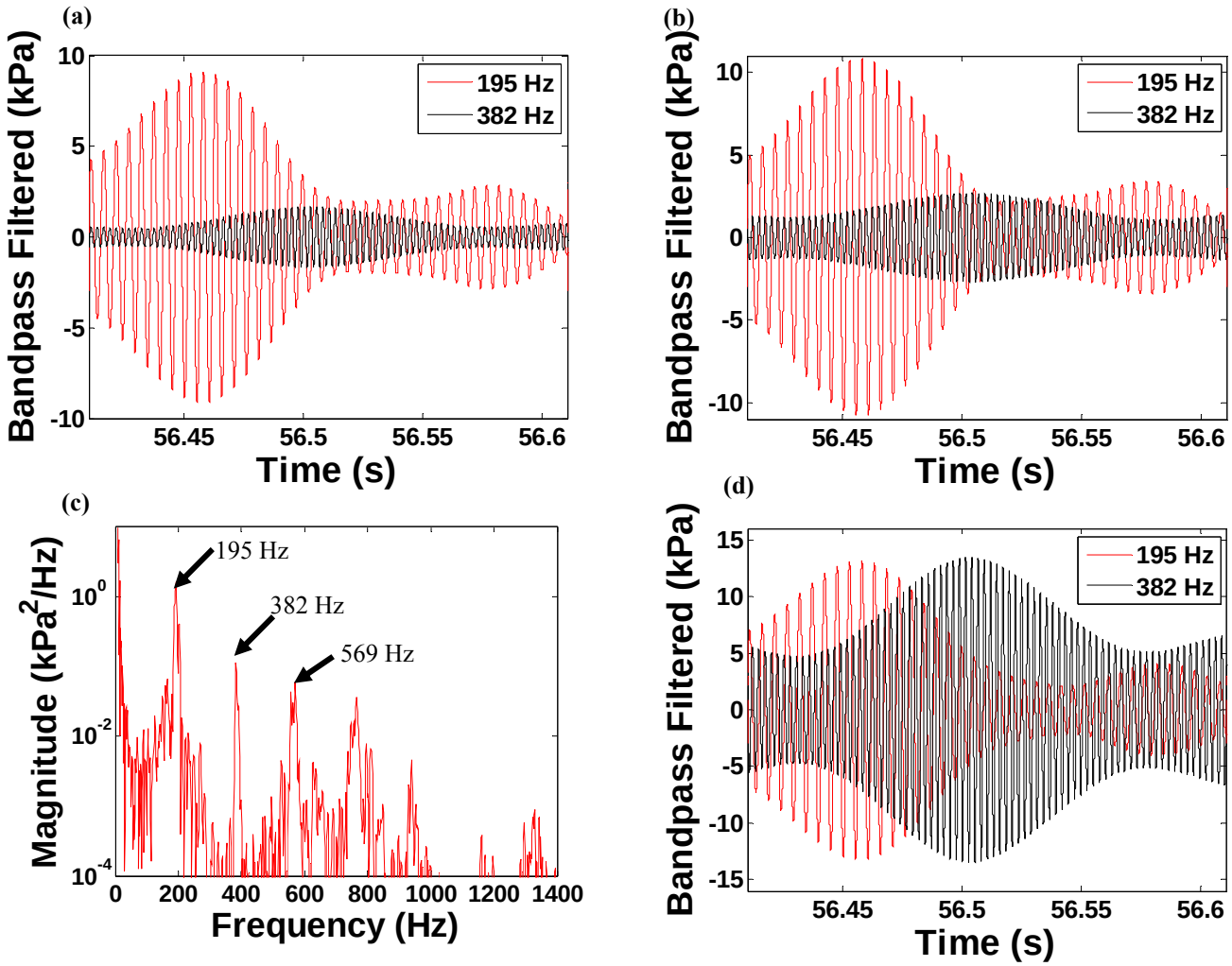

Figure 6.16. Bandpass filtered pressure at 195 Hz and 382 Hz for pressure transducers located in the crossflow 89 mm upstream of jet injection (a), inside the transverse injector (b), and at the exit nozzle of the combustion chamber (d). Plot (c) shows a PSD of the pressure at the 85 mm location upstream of the injector.

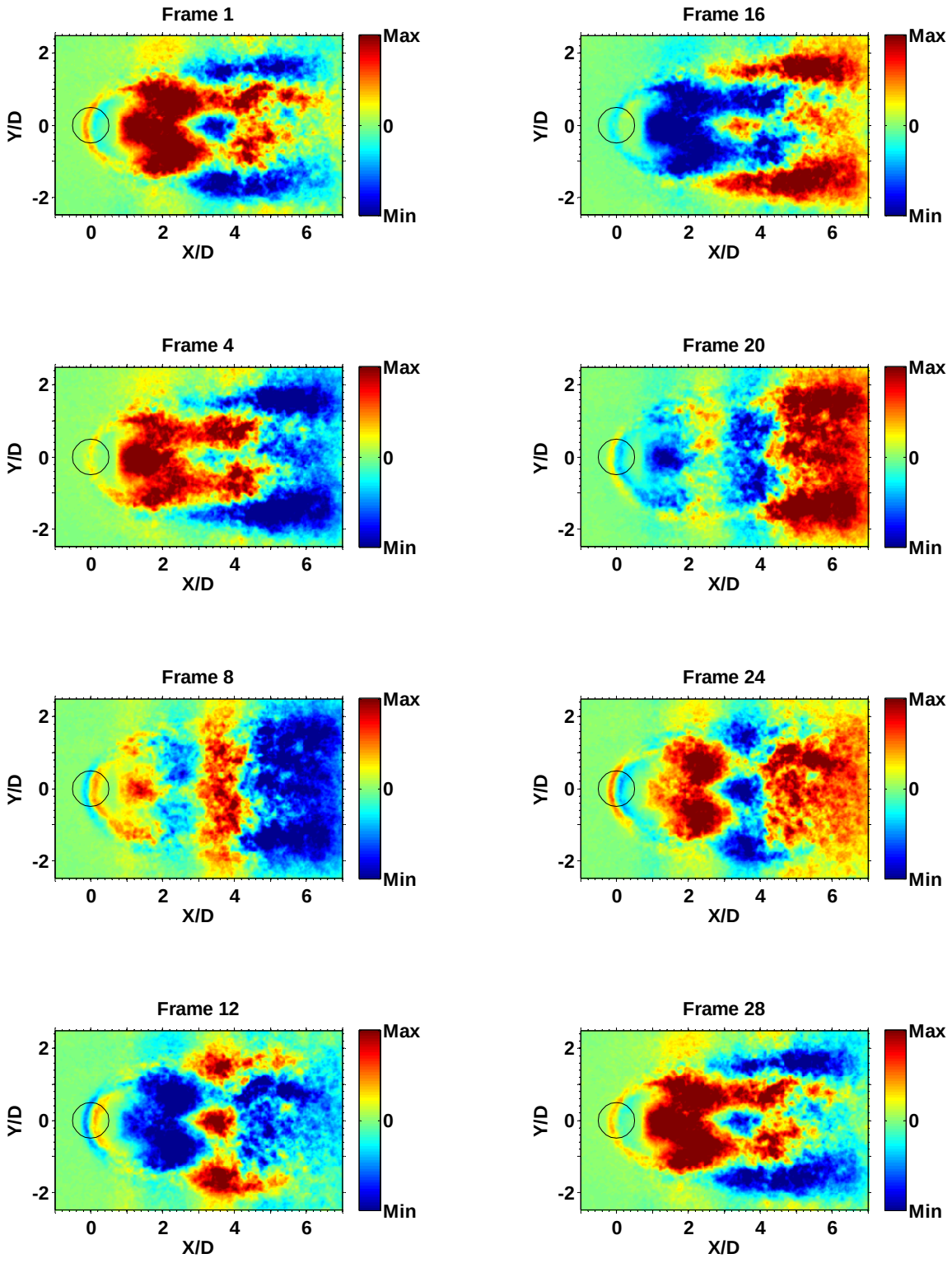

Figure 6.17. DMD spatial mode for 385 Hz corresponding to frames in Figure 6.11.

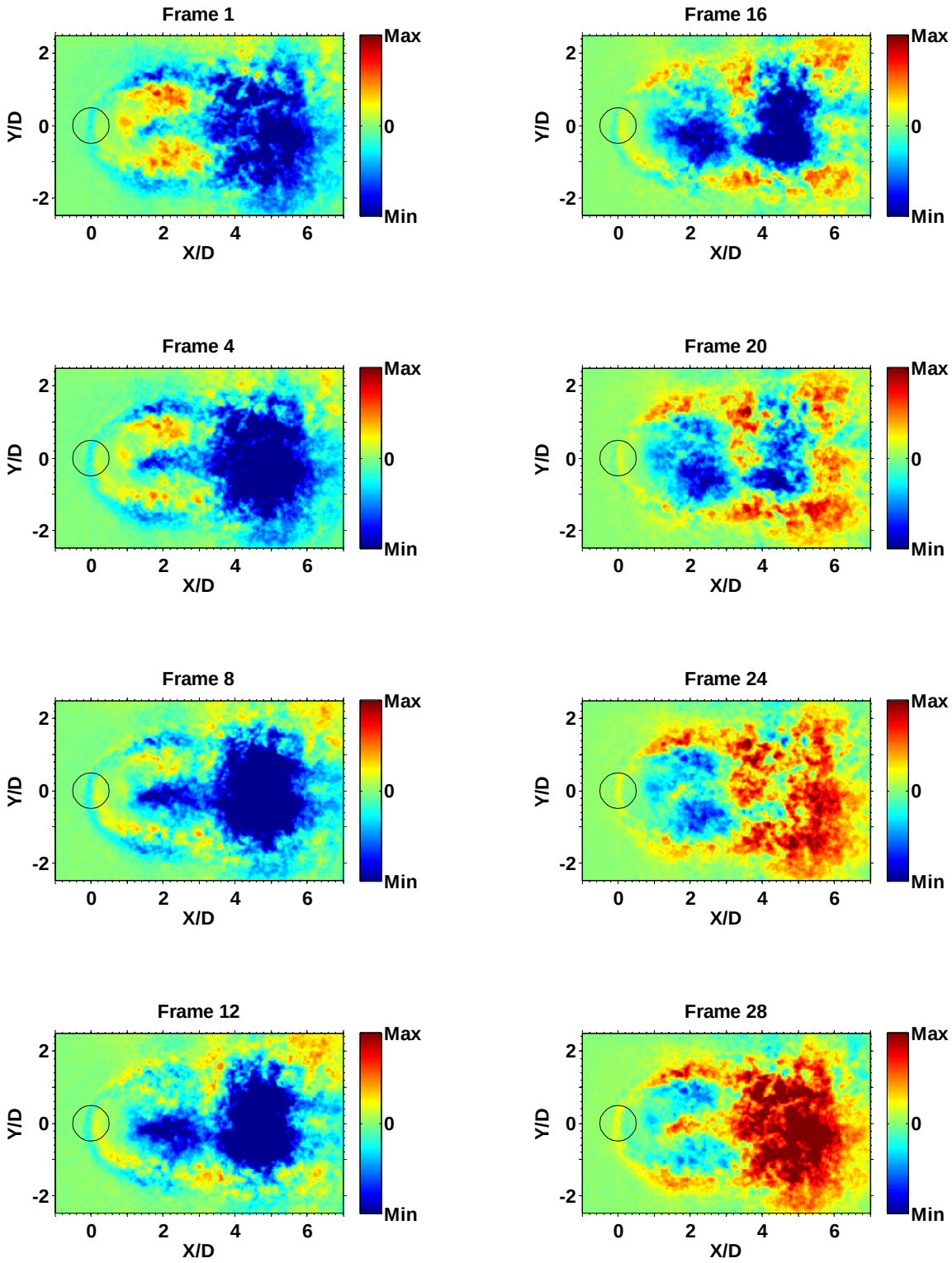

Figure 6.18. DMD spatial mode for 190 Hz corresponding to frames in Figure 6.11.

Test Case B

For the second test case, test case B, the crossflow dump plane equivalence ratio is 0.66 and corresponds to an adiabatic flame temperature of 2024 K as determined using Chemical Equilibrium with Applications (CEA) for a 634 K preheated natural gas and air mixture. Test case B corresponds to combustor configuration B in Figure 6.4. Figure 6.20 shows a sequence of unfiltered OH PLIF images for the cross sectional plane Z = 14.8 mm, where every third image in a consecutive sequence is shown in order to capture one cycle of the ~200 Hz crossflow acoustic. At this plane, the flame front location tends to be much wider in Y/D at a given X/D location, e.g. see Figure 6.20 frame 116 arrow, and the flame front leading edge is always further downstream in X/D as compared to plane Z = 4.8 mm. The wider jet plume and axially displaced windward flame front is not unexpected since the jet expands along its trajectory and is displaced as it bends into the crossflow, respectively. This can also be seen in the average for plane Z = 14.8 mm, see Figure 6.21, where the kidney shaped structure at plane Z = 4.8 mm (see Figure 6.14) has now moved downstream and grown in size. Additionally, there are no longer separated upper and lower frame front regions as observed at plane Z = 4.8 mm (see Figure 6.11 frame 1 to frame 8), instead plane Z = 14.8 mm is most similar in appearance to frame 12 to frame 18 in Figure 6.11. Much of the cyclical sinusoidal movement is observed in the windward edge flame front, e.g. following Figure 6.20 from frame 116 to frame 128, the flame front leading edge at X/D ~2 moves upstream to near X/D ~0. Figure 6.22 (c) and (a) shows frequency content and the corresponding bandpass filtered pressure at 194 Hz and 384 Hz for the time sequence for the frames in Figure 6.20. Both 194 Hz and 384 Hz have non-negligible crossflow acoustic pressure amplitudes at the anti-node, which is similar to the results for test case A. Figure 6.22 (b) shows the DMD calculated spectra using 2000 consecutive frames covering and surrounding the frames in Figure 6.20. Comparing the DMD spectra and the corresponding pressure spectra, the PLIF images contain frequency content identically at the crossflow acoustic frequencies, 194 Hz and 384 Hz. Figures 6.23 and 6.24 show sequences of the DMD spatial mode shapes constructed for the dominant frequencies in the DMD spectrum in Figure 6.22 (b). Both DMD mode shapes show coherent dynamic structures moving between an upstream position and a downstream position, closer to and further from the jet exit, respectively. The 195 Hz and 385 Hz DMD modes are capturing the movement of the jet flame front dynamics observed in Figure 6.20 frames. The dynamics of the 385 Hz DMD mode appear strongly linked to the local velocity fluctuations surrounding the point of jet injection. Figure 6.24 frame 101 to frame 110 shows a upstream moving structure which simultaneously occurs during a compression to rarefaction at the crossflow 384 Hz anti node downstream of the jet injection. As the compression becomes a rarefaction, the local flowfield velocity begins decreasing at the injection location, where the velocity perturbation at 384 Hz is against the mean vitiated flow. Oppositely, from frames 113 to frame 122, the 384 Hz DMD structure moves in the downstream direction, which follows a velocity perturbation adding to the mean vitiated flow as the rarefaction transitions into a compression at the 384 Hz anti node downstream of jet injection. The DMD 195 Hz spatial mode appears correlated to the local velocity perturbation field: Figure 6.23 frames 101 to 119 correspond to a rarefaction to compression where the structure is further downstream as compared to frames 125 to 143, where intensification in the downstream horseshoe structure between frames 107 and 113 appears closely in phase with the crossflow velocity fluctuation (at its maxima ¼ period after the rarefaction). The opposite is observed for the back half of the cycle from a compression to a rarefaction. Also, from Figure 6.20 at frame 140 and following the

DMD 195 Hz cycle in Figure 6.23, the burned gas wake-like region centered on (Y/D,X/D) = (0,5.5) appears to flap into and out of plane at the crossflow 194 Hz frequency. This highlights the highly three dimensionality of the reacting jet and different time scales present for this flowfield, suggesting that the 195 Hz slower mode is transporting the bulk of the jet into and out of plane, while the relatively faster 385 Hz mode is interacting with a moving jet such that the as the 385 Hz cycle repeats, a new compression at 385 Hz effectively interacts with a different jet.

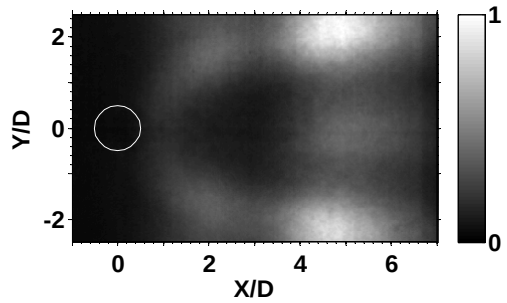

Figure 6.21. OH PLIF average at plane Z = 14.8 mm.

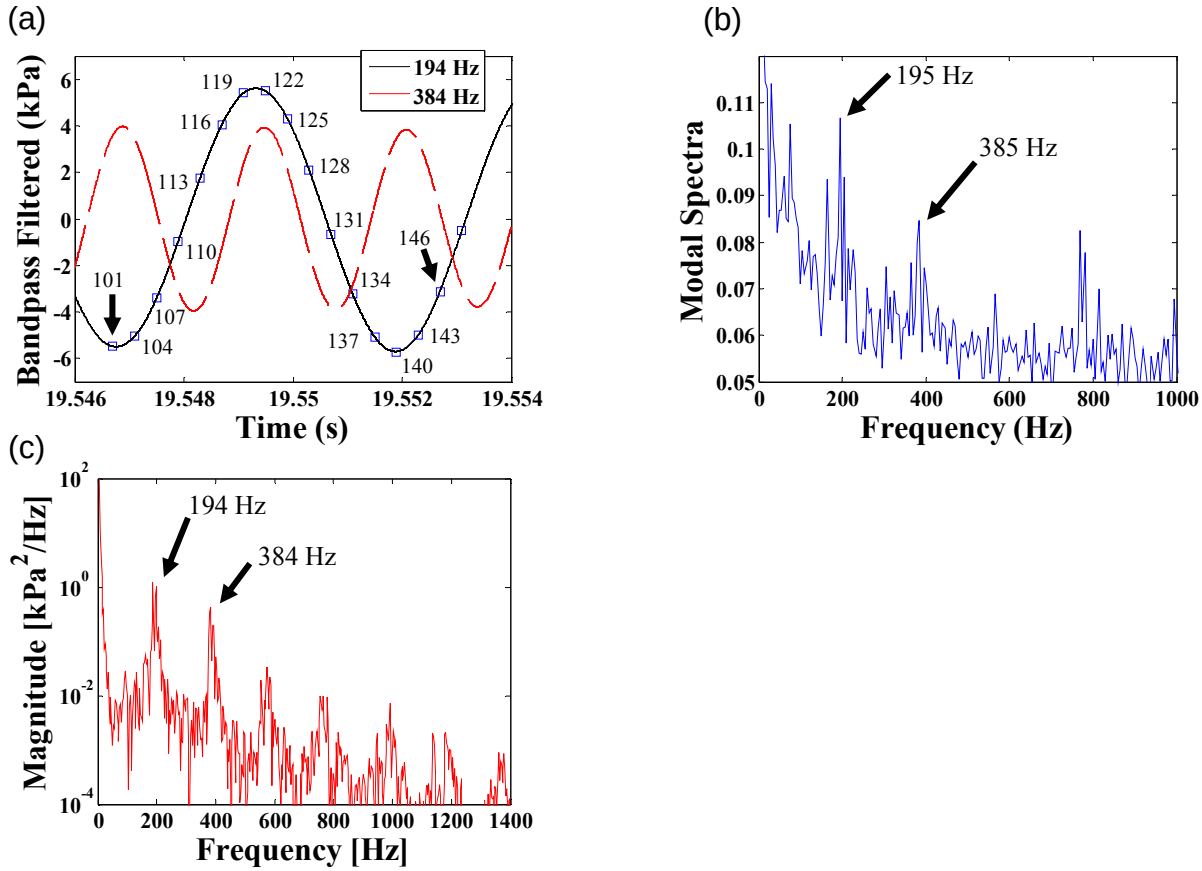

Figure 6.22. (a) Bandpass filtered pressure at antinode of 194 Hz and 384 Hz acoustic pressure mode. Numbered data points correspond to Figure 6.20 frame numbers and are shown on 194 Hz data line only for clarity. (b) DMD power spectra for test case B. (c) Pressure PSD covering data in (a) and located at anti-node of both 194 Hz and 384 Hz.

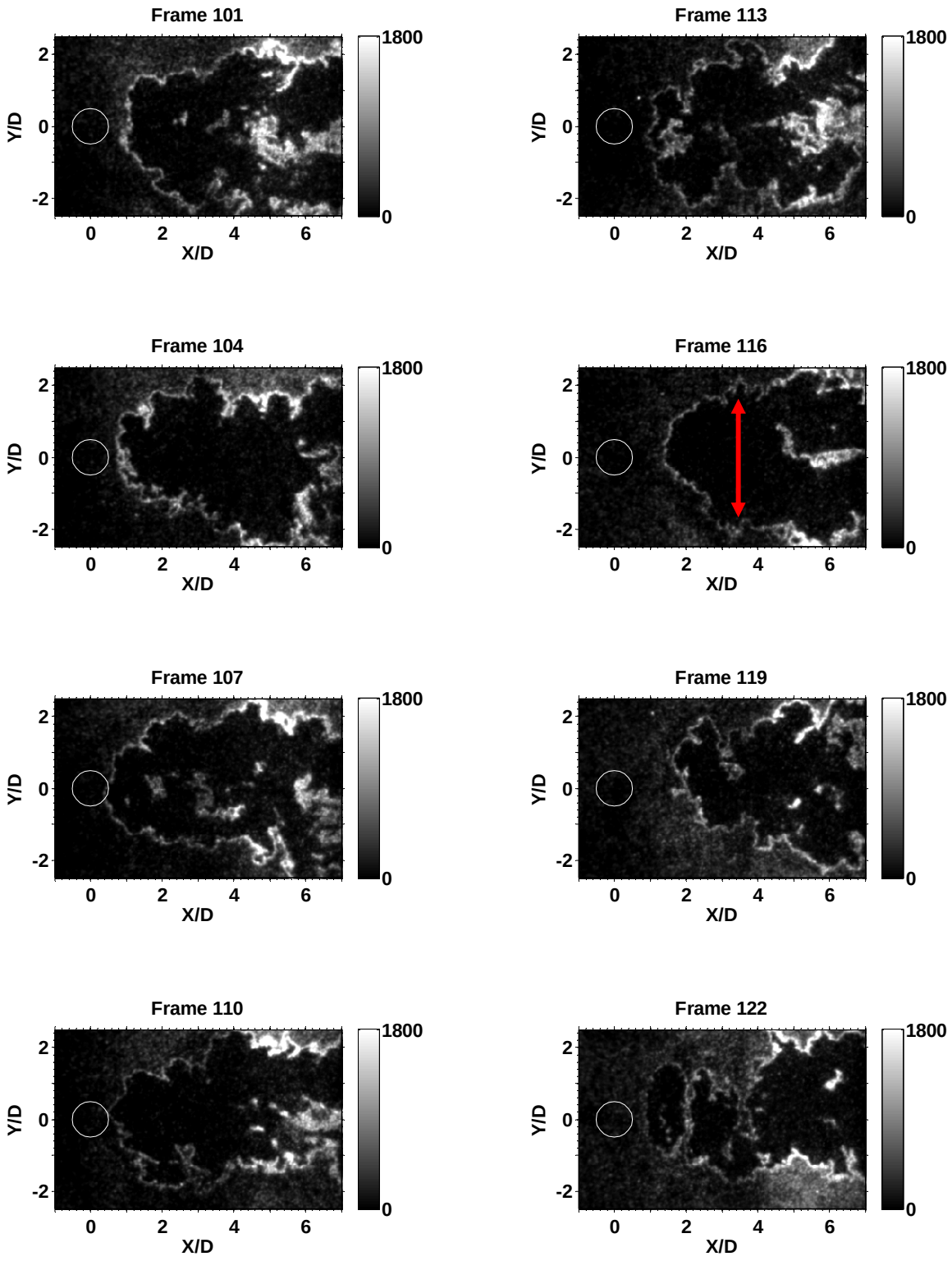
Frame 101
Frame 113
Frame 104
Frame 116
Frame 107
Frame 119
Frame 110
Frame 122
Y/D
X/D
2
0
-2
0
2
4
6
1800
0

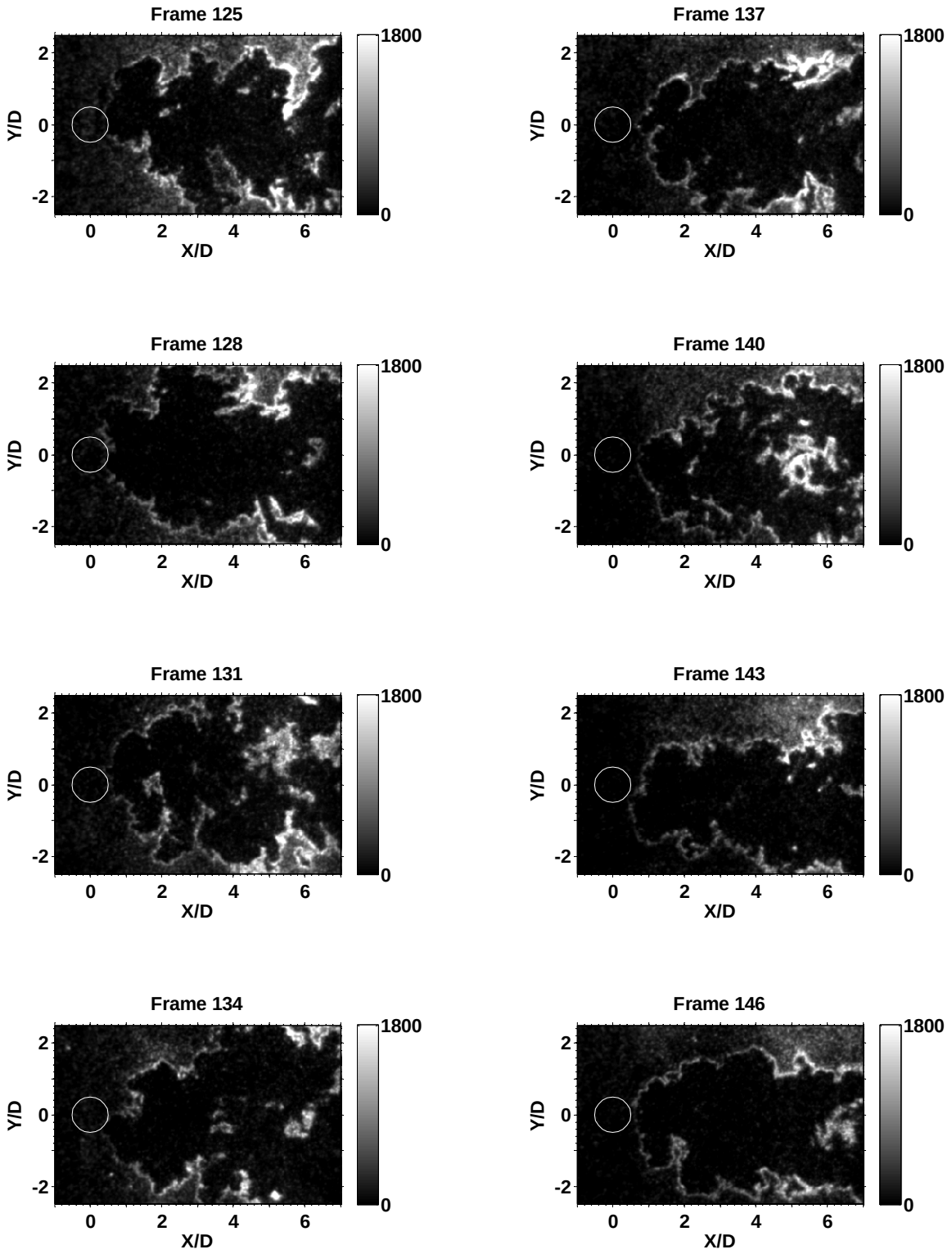

Figure 6.20. Plane z = 14.8 mm unfiltered OH PLIF images. Every third image shown to capture a full period for the 194 Hz acoustic mode.

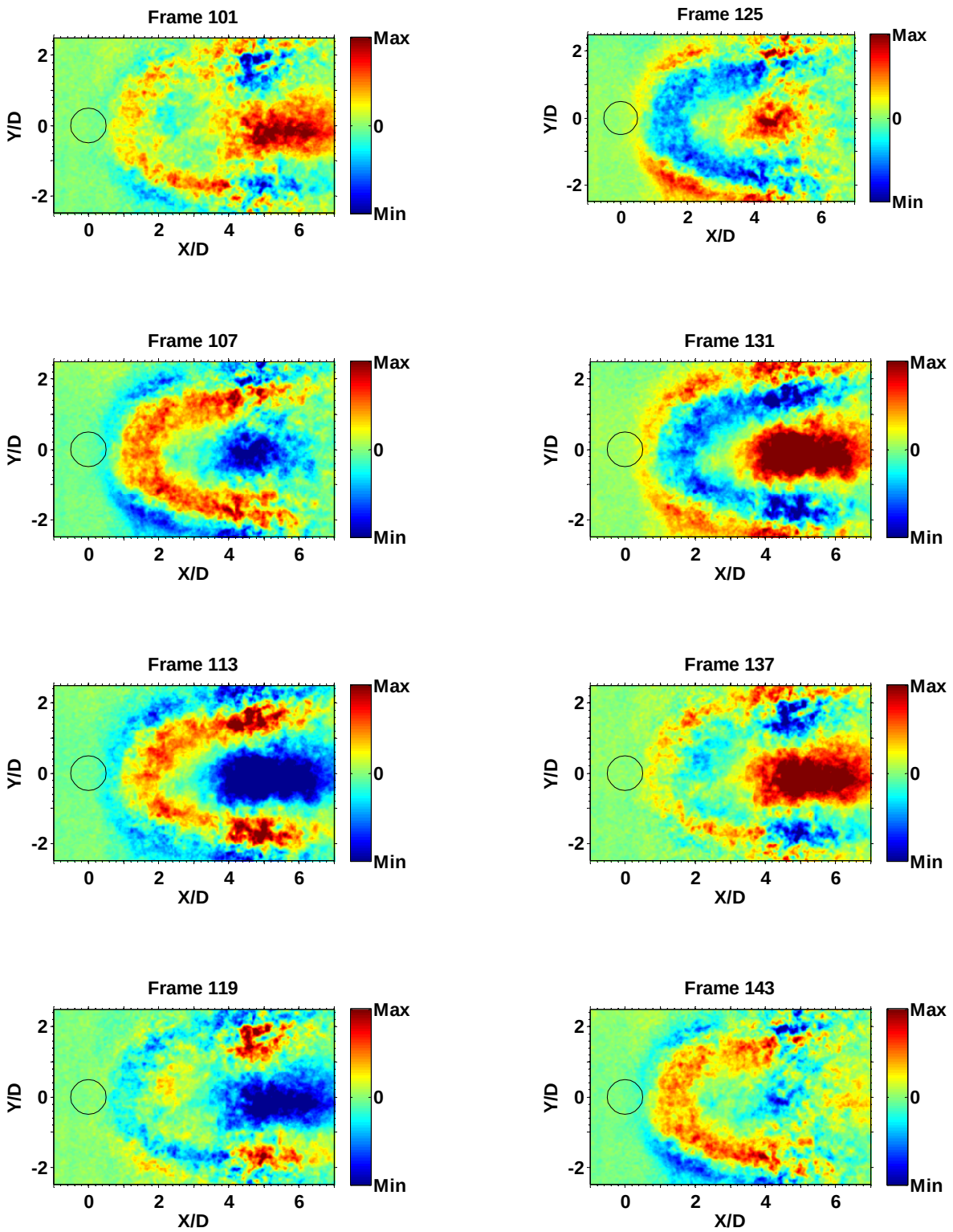

Figure 6.23. Test case B DMD mode for 194 Hz. The frame numbers correspond to those in Figure 6.22(a) and Figure 6.20. Every sixth image is shown to capture one period of the 194 Hz cycle.

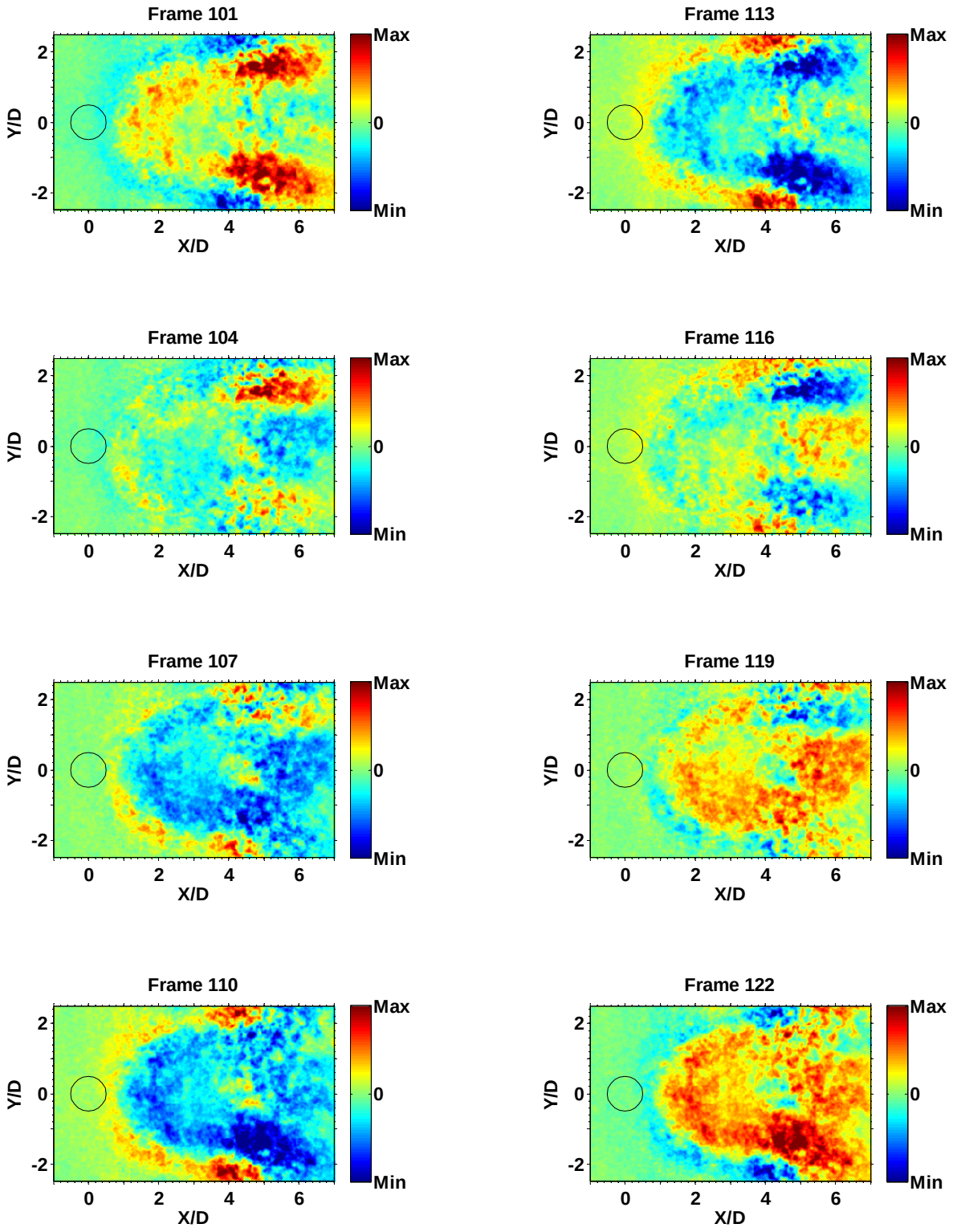

Figure 6.24. Test case B DMD spatial mode for 384 Hz. The frame numbers correspond to those in Figure 6.22(a) and Figure 6.20. Every third image is shown to capture one period of the 384 Hz cycle.

Test Case C

For the third test case, test case C, the crossflow dump plane equivalence ratio is 0.68 and corresponds to an adiabatic flame temperature of 2040 K as determined using Chemical Equilibrium with Applications (CEA) for a 615 K preheated natural gas and air mixture. Test case C corresponds to combustor configuration B in Figure 6.4. Figure 6.25 shows a sequence of unfiltered OH PLIF images of the X-Z cross sectional plane located at Y/D = 0 mm, i.e. the PLIF sheet is centered on Y/D = 0 and extends in the Z direction (see Figure 6.10). The crossflow is from left to right, the jet exit is located at Z = 0, the jet orifice center is still located at X/D = 0, and the rectangle at the upper left of each figure represents the jet exit location. Full view of the jet injection wall and flush mounted jet orifice is afforded at this viewing angle. The unfiltered Figure 6.25 images cover one cycle of the 192 Hz crossflow frequency and contain interesting features not directly observable in the X-Y cross section. Most notable is a jet trajectory based on the apparent location of unburned fluid in between the windward and leeward flame fronts. Figure 6.25 frame 204 highlights the location of the windward leading edge of the flame front, the leeward downstream edge of the flame front, and an approximate location of the jet trajectory between these two edges. The trajectory line is not calculated and is drawn in for clarity. Unsteady burned gas regions are also observed downstream of the jet exit (see frame 231), display fluctuations along with the jet, and appear to be a recirculation region of the reacting jet.
The images also show a significant crossflow background upstream of the jet windward flame front which has not been subtracted from the images (see Figure 6.25 frame 219). This background is due to OH fluorescence of the vitiated crossflow and not the vitiated crossflow chemiluminescence (determined using the same procedure outlined for the X-Y cross sectional plane results). The crossflow fluorescence intensity magnitude relative to the jet flame front is large for this particular test case and is attributed to test day fluctuations in the dye laser UV power output, in which higher intensifications of the high speed UV intensifier was used to resolve the flame front. This challenge was not present for X-Y cross section test days. Large scale structure evolution at 10 kHz is possible (not shown here) and every third frame in Figure 6.25 shows considerable jet fluctuations in the Z and X directions: jet penetration based on the windward flame front fluctuates between Z/D = 3 (frame 246) to greater than Z/D = 5 (frame 207) for the X/D length shown. Additionally, the jet displays fluctuations in the X/D direction at a given Z/D (see frame 207 and 210). Figure 6.25 also shows a range of jet rollup structure sizes. Frame 213 shows windward edge structure sizes close to the jet exit on the order of half the jet diameter, while frame 216 shows a structure further from the jet exit and larger than the jet diameter. Both of these coherent structures are likely a combination of the rollup up of the jet shear layer into the jet shear layer vortices, pairing of the jet shear layer vortices, and the jet fluctuations in the Z and X directions. A DMD analysis will prove useful in identifying and sorting the dominant coherent structures in the highly unsteady reacting jet.

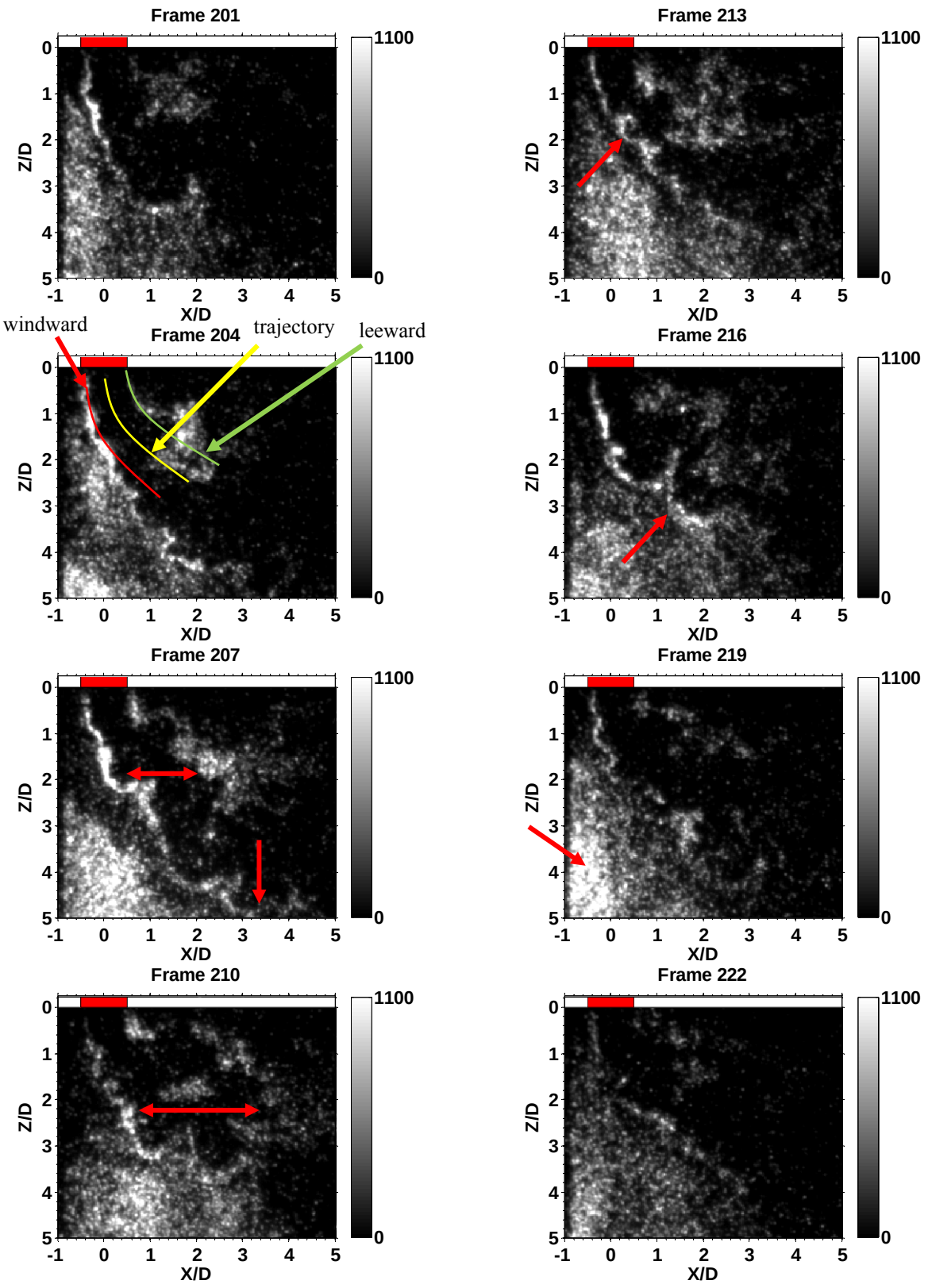
Frame 201
Frame 213
Frame 204
Frame 216
Frame 207
Frame 219
Frame 210
Frame 222
windward
trajectory
leeward
Z/D
X/D
1100
0

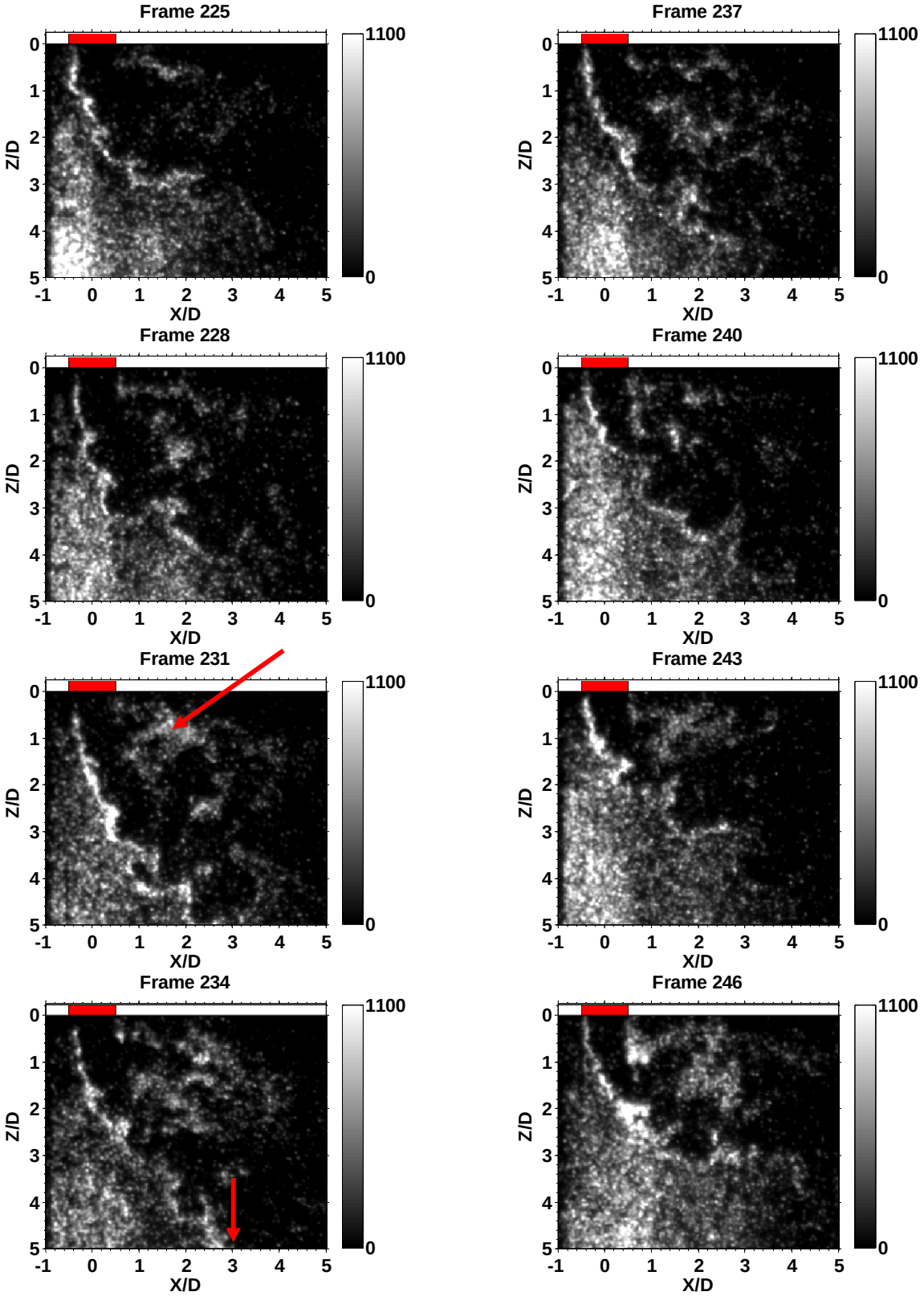

Figure 6.25. Unfiltered OH PLIF images of the X-Z cross section. Every third image shown to capture a full period for the 194 Hz acoustic mode.

Figure 6.26 shows an average taken for 2000 consecutive frames containing the images in Figure 6.25. The relatively large magnitude crossflow intensity is evident for Z/D > 2 and X/D <1. The windward jet flame front is evident by following the unburned injected reactants on the upstream jet edge. There is also a lower magnitude region directly downstream of the jet that appears attached at the injector, therefore making both the windward and leeward sides of the jet flame anchored at the point of jet injection, at least in the mean. In the instantaneous, however, Figure 6.25 shows instances where the jet windward (e.g. frame 234) and leeward (e.g. frame 216) edges appear to detach for portions of the crossflow acoustic cycle. Figure 6.27 shows spectra and filtered results for a 2000 frame time duration (0.2 sec). Figure 6.27 (a) shows frequency content of the pressure located at the antinode of both the 192 Hz and 387 Hz modes (downstream of the jet injection), (c) DMD spectra of the OH PLIF images for plane X-Z, and (b) the corresponding bandpass filtered pressure at the location in (a) at 192 Hz and 387 Hz for the time sequence for the frames in Figure 6.25, 6.28 and 6.29, and contained in the spectra in (a) and (c). Both 192 Hz and 387 Hz have non-negligible crossflow acoustic pressure amplitudes at the anti-node, which is similar to the results for test case A and B. Although there is an additional acoustic 582 Hz component contained in the 0.2 s duration used to calculate the DMD and pressure spectra, the following analysis will only focus on the 192 Hz and 387 Hz frequencies. For the 4.6 ms time period covering the images and results contained in Figures 6.25, 6.28 and 6.29, the acoustic amplitude of the 582 Hz frequency was attenuated and is an order of magnitude lower than either the 192 Hz or 387 Hz acoustic frequencies. _In addition to the frequencies near those in the crossflow (192 Hz, 387 Hz, 582 Hz), the DMD spectra in Figure 6.27 (c) shows additional frequency content at 455 Hz and 495 Hz. These frequencies are not part of the dump combustor crossflow acoustic standing waves and rather appear to be frequencies associated with jet coherent structures. An analysis of the 455 Hz DMD mode will precede the analysis of the 192 Hz and 387 Hz DMD modes.

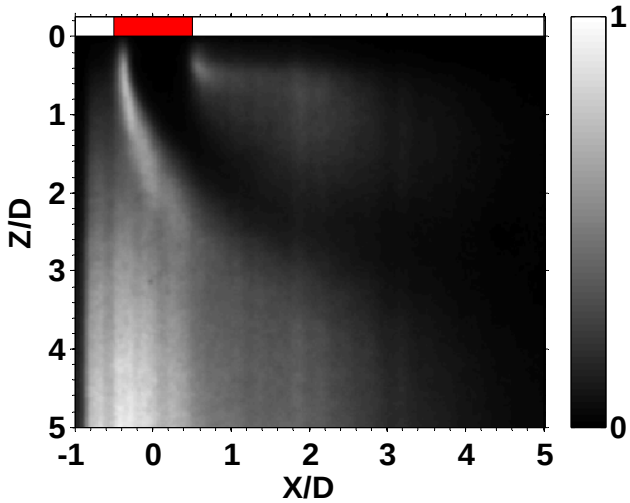

Figure 6.26. OH PLIF average for X-Z cross section. Rectangle at upper left represents injector orifice and is centered at (Z/D, X/D) = (0,0). Crossflow is from left to right.

Figures 6.28 and 6.29 show sequences of the DMD spatial mode shapes constructed for the 195 Hz and 365 Hz frequencies in the DMD spectrum in Figure 6.27 (c). Every sixth (third) frame is shown for the 195 Hz (365 Hz) DMD calculated frequency to cover one complete crossflow acoustic cycle. It should be noted, though, that while for X-Y cross sections the frequencies in the pressure spectra and in the DMD spectra are within 5 Hz of each other, the 365 Hz frequency in the DMD spectra is 22 Hz from the 387 Hz pressure peak. For both the 195 Hz and 365 Hz frequencies, however, the DMD mode shapes show coherent dynamic structures that are different relative to one another. The DMD 195 Hz describes a large scale flapping of the whole jet, where Figure 6.28 frame 231 shows deeper penetration into the crossflow as compared to frame 201. Frame 219, 225, and 231 correspond to a compression moving toward a rarefaction at the crossflow 192 Hz pressure anti node downstream of the jet. As the compression begins to relieve itself and move toward a rarefaction, the crossflow velocity at the point of jet injection begins to decrease with a maximum decrease occurring at ¼ of a period following the compression (between frame 231 and 237). The DMD spatial mode shows minor changes between frame 231 and 237 and signifies that the jet flapping is in phase with the crossflow velocity oscillations. This is in agreement with the DMD results of test case A and B where the jet displays strong coherence with the fluctuating crossflow velocity field. The DMD 365 Hz results in Figure 6.29 are more challenging to interpret due to what appears to be a large crossflow contribution inside the computed spatial mode shape (e.g. see oval drawn in frame 201). However, it appears this jet response is in phase with the crossflow velocity perturbations at the crossflow 387 Hz frequency. At frame 201, the windward jet edge is nearly parallel with the Z axis up to one jet diameter away from the jet exit (see arrow in frame 201). This corresponds to approximately one half of a period after a compression at the pressure anti node located downstream of the jet injection and signifies that the crossflow acoustic velocity at 387 Hz is at its minima at the crossflow momentum flux is low at the point of injection and allowing for increased nearfield jet penetration. Figure 6.29 frame 213 and 216 are both near the maxima in crossflow velocity and agree with a decreased initial penetration due to increased crossflow momentum flux. Figure 6.30 show results for the 455 Hz DMD spatial mode. As in the case of the 365 Hz DMD mode, there is a strong crossflow background and makes it challenging to discern the actual jet dynamics. However, focusing on a region within one jet diameter outside of the injector, the windward and leeward jet edges are out of phase with each other. This is seen in Figure 6.30 (a) – (d) where arrows identify the jet shear layer dynamics out of phase with each other. Figure 6.30 (e) shows the pressure spectra of the transducer inside the jet injector and was calculated using 0.6 s of data in order to elucidate the weak minor peak observed at 461 Hz (very close to the DMD 455 Hz frequency). Aliasing of the images due to any frequencies found in the crossflow or injector pressure spectra due to the low 10 kHz image sampling was also considered, but ruled out since there are no frequencies in the flowfield that would produce a 455 Hz aliased signal at a sample rate of 10 kHz (Aliased Frequency = Sample Rate*integer – Actual Sampled Frequency). Since the X-Y cross sectional DMD spectrums do not contain a prominent frequency near 455 Hz and since it is so prominent in DMD spectrum, it appears then that 455 Hz is a real frequency present and is associated predominantly with the initial jet shear layer. Future work will investigate this frequency.

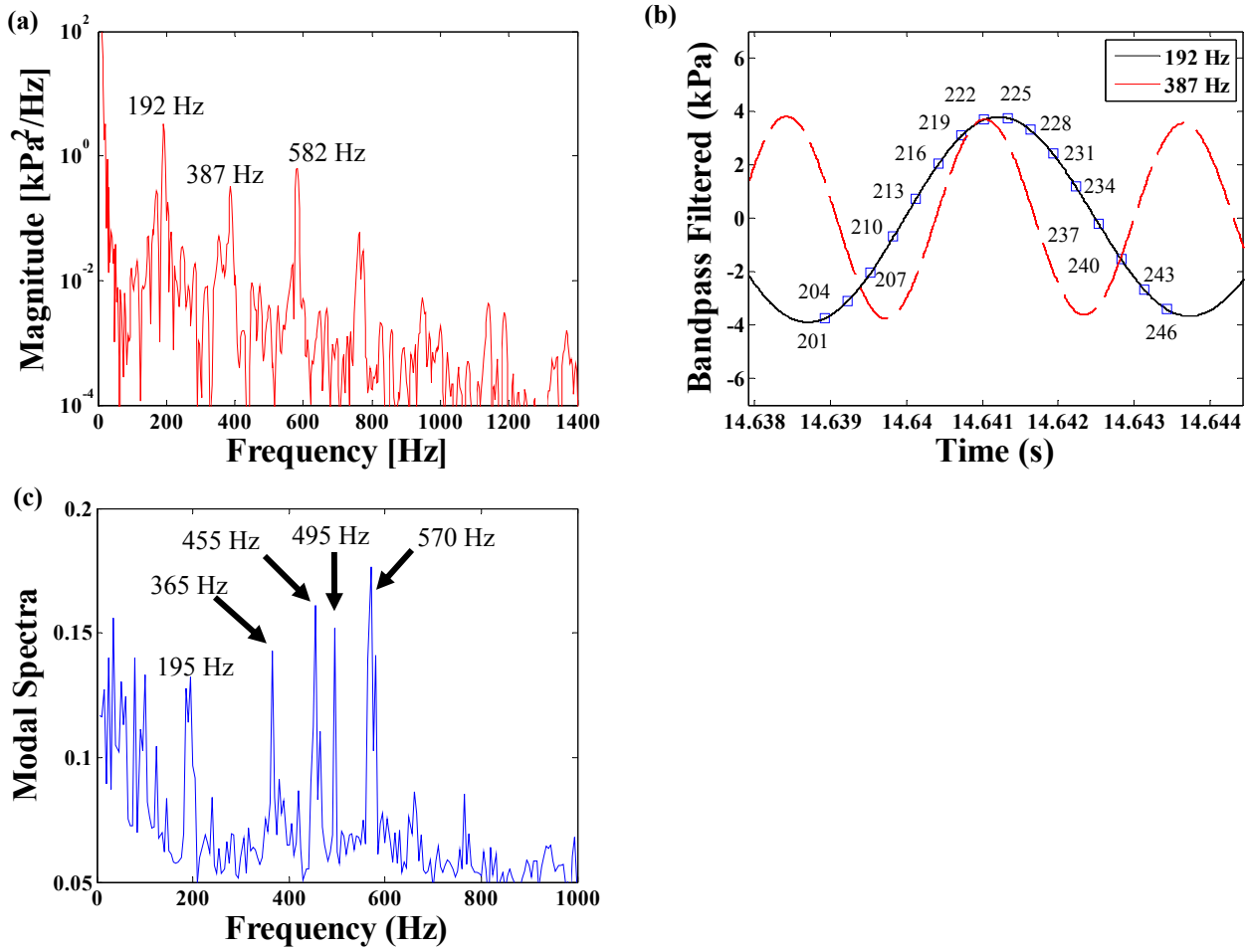

Figure 6.27. (a) Pressure PSD covering 2000 frame time duration for which DMD was applied. Pressure is located at anti-node of both 192 Hz and 387 Hz. (b) Bandpass filtered pressure at antinode of 194 Hz and 384 Hz acoustic pressure mode. Numbered data points correspond to Figure 6.26 frame numbers and are shown on 194 Hz data line only for clarity. (c) DMD power spectra for test case C.

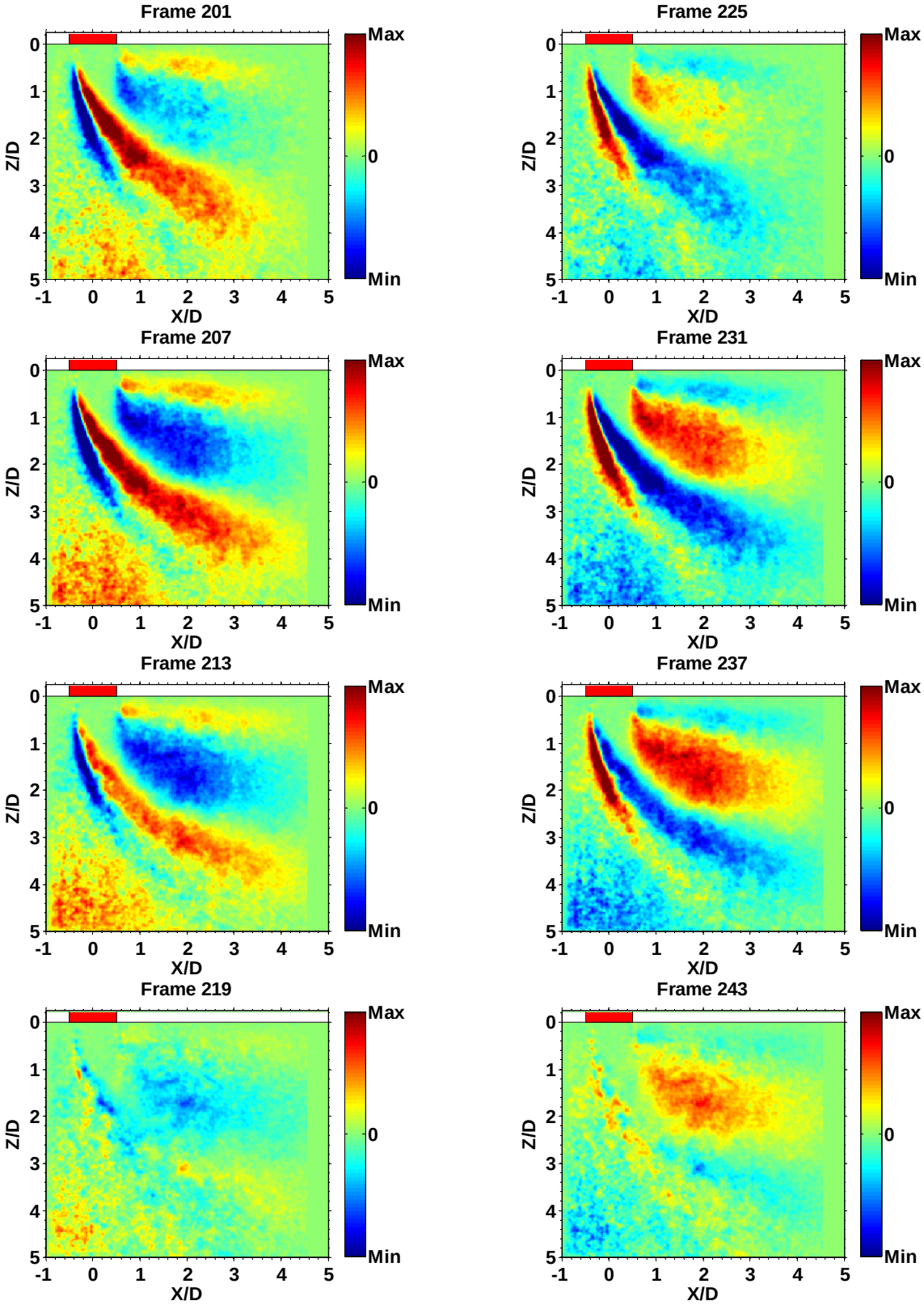

Figure 6.28. Test case C DMD spatial mode for 195 Hz. The frame numbers correspond to those in Figure 6.25 and Figure 6.27 (b).

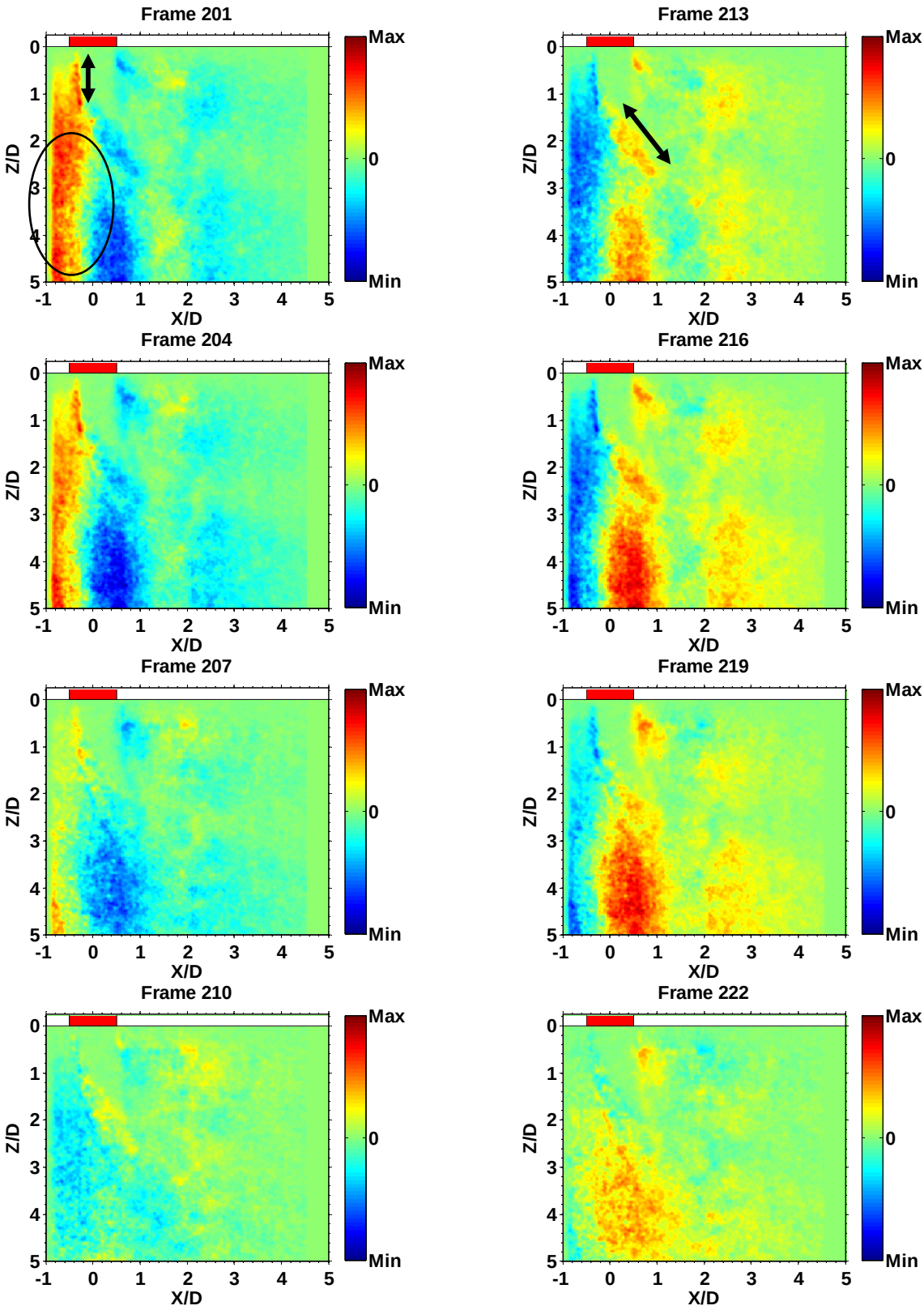

Figure 6.29. Test case C DMD spatial mode for 365 Hz. The frame numbers correspond to those in Figure 6.25 and Figure 6.27 (b).

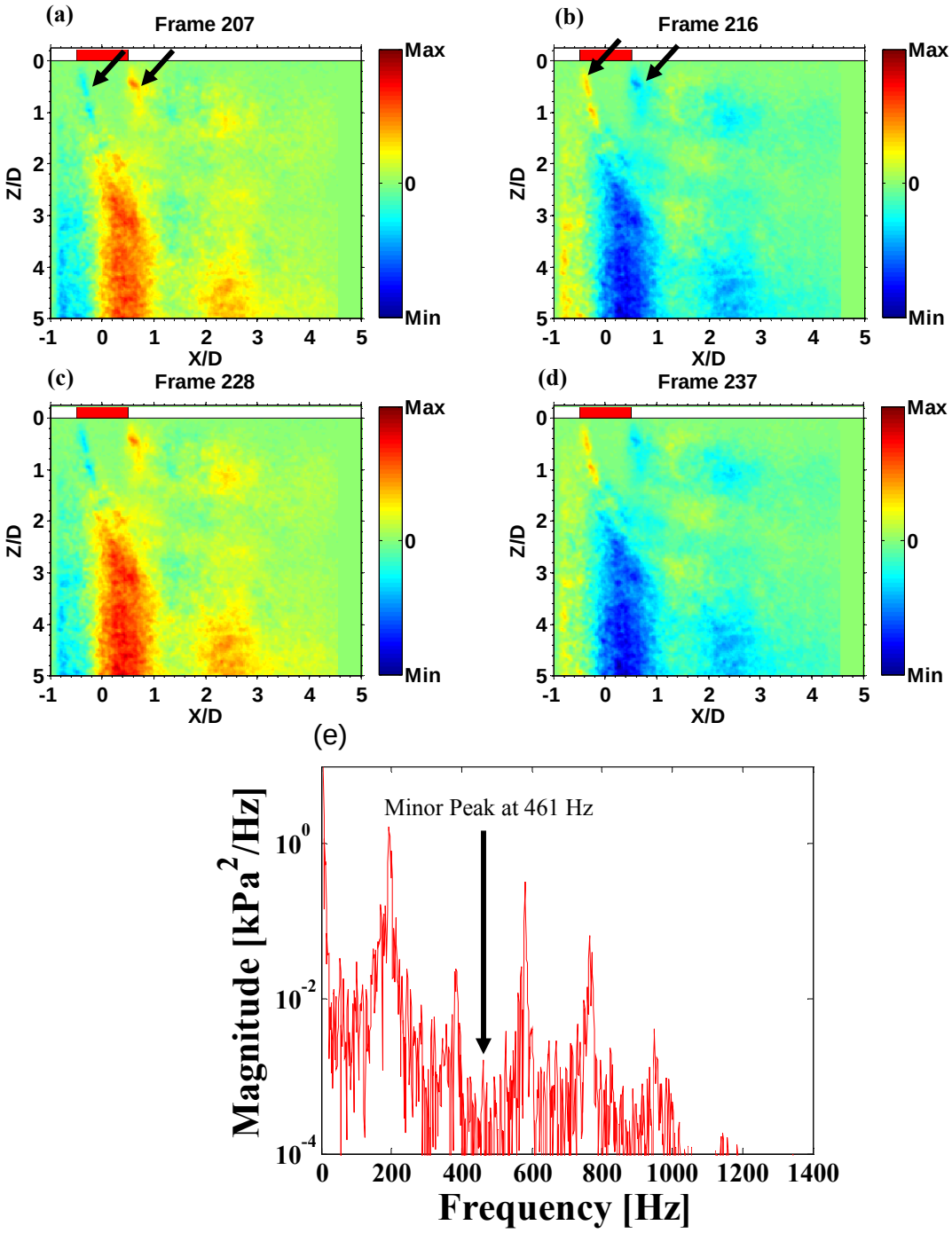

Figure 6.30. (a)-(d) Test case C DMD spatial mode for 455 Hz. The frame numbers correspond to those in Figure 6.25 and Figure 6.27 (b). (e) spectra of the pressure transducer inside the injector calculated for a 0.6 s duration.

SubTask 6.2: Simultaneous High-Speed PIV/OH PLIF Measurements of Combustion Instabilities for Natural Gas Jets Injected Into Vitiated and Nonvitiated Crossflows

This subtask has not yet been completed. We have just started to perform PIV measurements in the RJIC instability rig. It will be completed later this spring with funding from Siemens Energy.

SubTask 6.3: Simultaneous High-Speed PIV/OH PLIF Measurements of Combustion Instabilities for HHC Gas Jets Injected Into Vitiated and Nonvitiated Crossflows

This subtask has not yet been completed. We have just started to perform PIV measurements in the RJIC instability rig. It will be completed later this spring with funding from Siemens Energy.

TASK 7.0: CARS STUDIES

Dual-pump CARS was used to determine the temperature and H_2/N_2 concentration ratio profiles in a point-wise fashion. Dual-pump CARS (Lucht 1987) as a technique to simultaneously obtain CARS spectra from two species at nearly the same frequency using the same three laser beams. Two different pump laser beams at frequencies ω_1 and ω_2 and a Stokes laser beam at ω_{st} were used to access Raman resonances at frequencies ω_1, ω_{st} and ω_2 for N_2 and H_2. The CARS signals were then generated by overlapping the three laser beams in a volume which produced athe CARS signal. Using a broadband dye laser (BBDL) for the Stokes beam allowed for single pulse measurements by simultaneously accessing all the Raman resonances in a given spectral band, thereby generating the entire CARS spectrum.

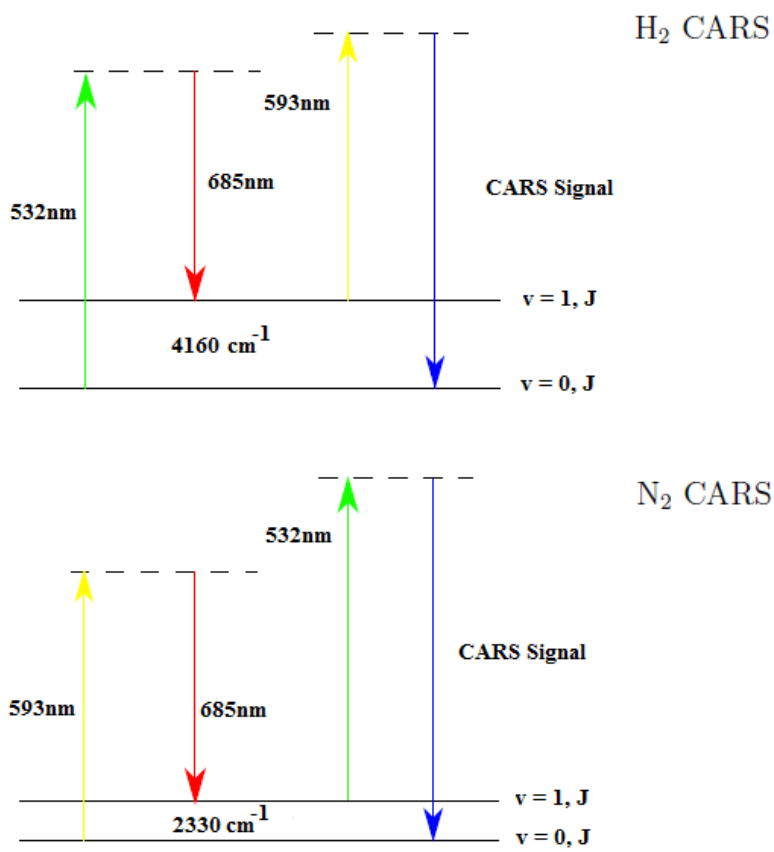

Figure 7.1 Energy level diagram for the H2/N2 dual pump CARS system employed (Lucht 1987).

Dual pump H_2/N_2 CARS measurements were performed on the same operating condition as the OH-PLIF study. The laser beams for the CARS measurements were generated in the High Pressure laser lab. The CARS measurements were performed using a 10 Hz laser system. Figure 7.2 shows a schematic of the how the three laser beams were generated in the High Pressure laser lab. The laser beam of 532 nm, generated by a Nd:YAG laser (Spectra-Physics Model PRO 290-10), pumped two dye lasers, a narrow band laser beam centered at 593 nm (Continuum Model ND60) and a broadband Stokes (BBDL) beam centered at 685 nm with a 37 nm pulse width (FWHM) built in house. The narrow band laser beam was generated using Rodamine 610

dissolved in methanol, while the Stokes beam was generated using a mixture of LDS 698 and DCM dissolved in ethanol.The three laser beams where then temporally overlapped and sent to the test.

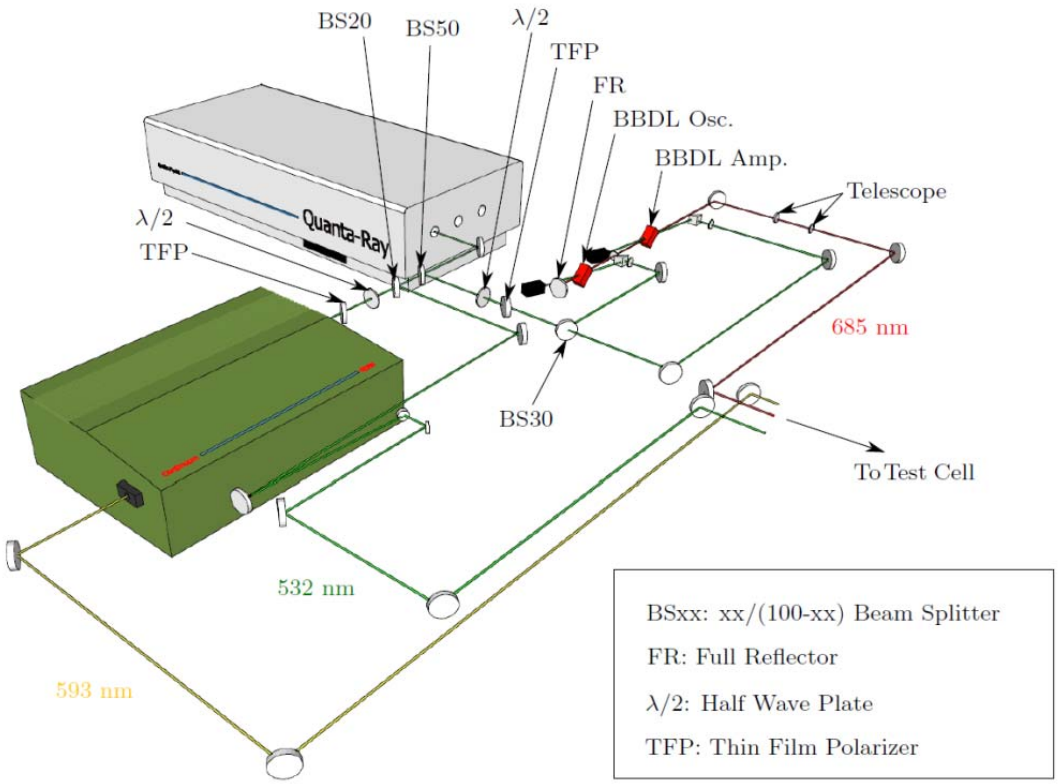

Figure 7.2 Schematic of the CARS laser system inside the laser lab.

Figure 7.2 shows the optical arrangement of the three CARS laser beams within the test. The energies and the polarization were controlled with the use of half wave plates and thin film polarizers. The all three beams were set to an energy of 27 mJ/pulse and were horizontally polarized. The three CARS beams were arranged in a BOXCARS configuration. The three beams were then directed to towards horizontal and vertical translation stages and then focused using a plano-convex lens with a focal length of 250 mm. The horizontal and vertical translation stages were used to move the CARS probe volume in a grid pattern of 10 row and 14 columns within the combusting flow field. The three beams and the CARS signal were re-collimated on the far side of the window combustor with another 250 mm plano-convex lens. The CARS signal was then directed towards onto the entrance slit of 1 m spectrometer (SPEX model 1000M) while the other three laser beams were directed to beam dumps. A neutral density filter attenuated the CARS signal and an interference filter (Semrock Model FF01-470/22), centered at 470 nm with a bandwidth of 22 nm FWHM), was used to reduce the interference from scattered light.

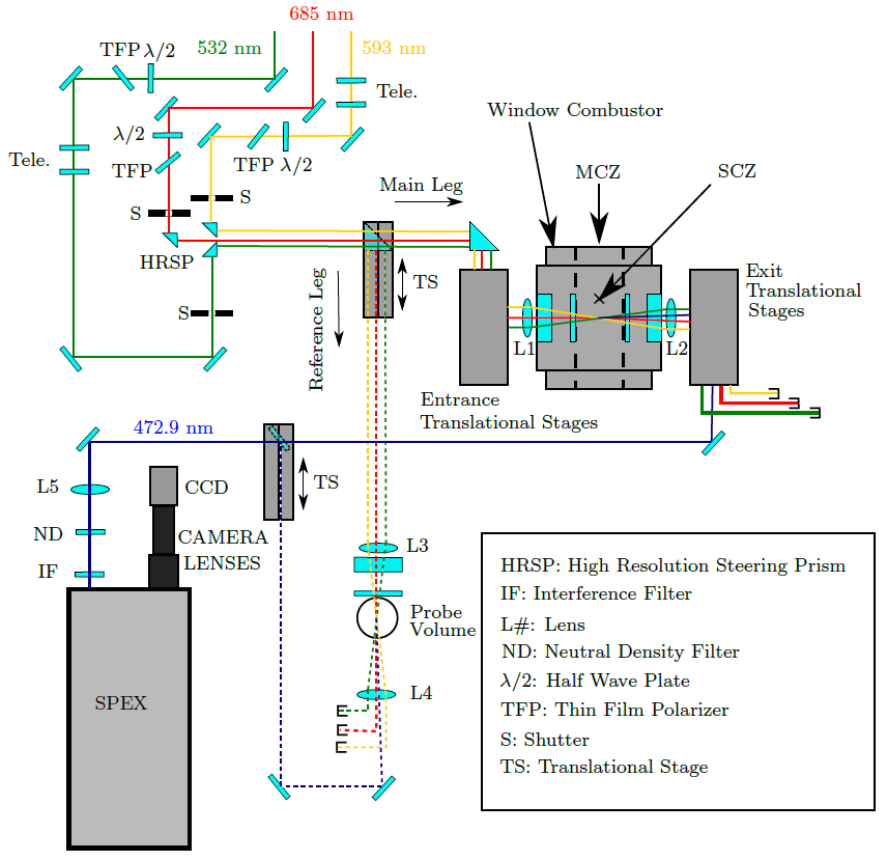

Figure 7.3 Schematic of the CARS laser system inside the test cell.

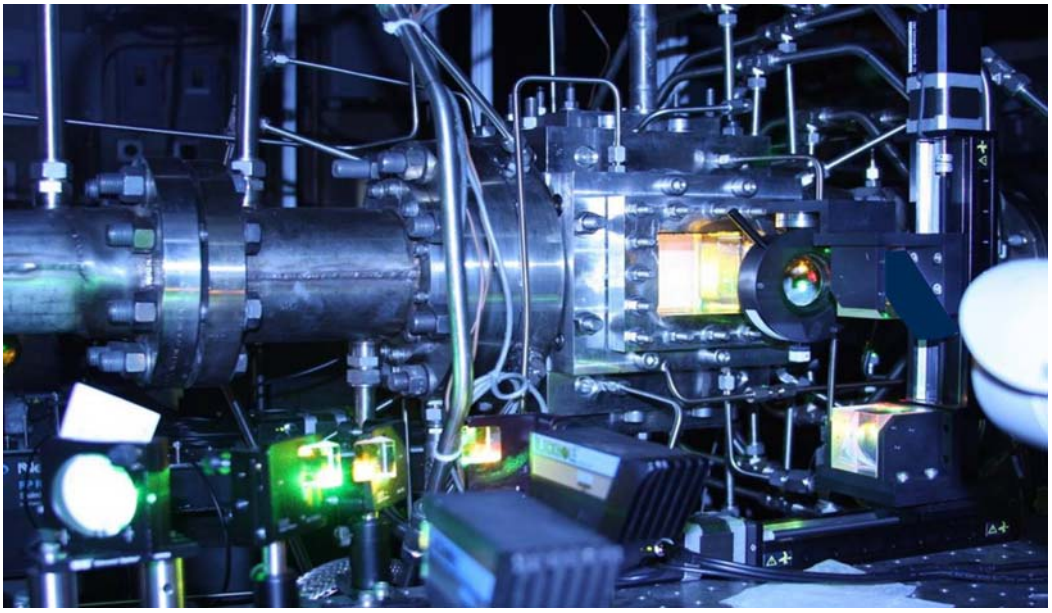

Figure 7.4 Photograph of test rig under operation, with the pump, stokes and probe beams going through the window of the SCZ.

CARS Processing

For the N_2/H_2 dual pump CARS was used to compare where the highest temperatures of the reacting jet occur and where the hydrogen to nitrogen ratio is the highest. Since there is no diatomic hydrogen present in natural gas, CARS system was used to detect the location of where the hydrogen was present and hence hydrogen serves as indicator on the location of the flame front, just like the OH fluorescence in the PLIF study. The processing of the dual-pump CARS spectra followed a similar procedure outlined by (Thariyan *et al*. 2010) At each spatial location, 300 CARS spectra were captured by the CCD camera. The raw spectra were first subtracted by the mean background spectra and then divided by non-resonant background collected using the reference leg, as shown in figure Z. The square root was taken afterwards and the data was filtered to remove some of the noise the excess noise. The processed CARS signal and was then compared to the theoretical CARS spectra using a least-squared fit procedure of the Sandia CARSFT code.

By comparing the experimental spectra with the theoretical CARS spectra, a temperature and a H_2/N_2 ratio can be determined for each spatial point. The temperature for each spectrum was obtained by analyzing the N_2 part of the spectrum. An average temperature was calculated using the 300 spectra collected for each spatial point. The H_2 concentration ratio was determined by fixing the temperature for previously determined N_2 spectra and reprocessing the spectrum. All 300 experimental spectra from each spatial point were analyzed in a batch mode running the CARSFT code. Due to the turbulent, unsteady nature of the reacting jet, H_2 was not present in every CARS spectrum collected. At each spatial position that was probed with CARS volume, the spectra collected was used to create a temperature distribution and H_2/N_2 distribution. Not all 300 spectra at each spatial point were able to be used in the post analysis probably due to the turbulent beam steering, dust in the flow field, or other interferences in the flow field.

SubTask 7.1: CARS Measurements of Temperature and Species for Natural Gas Jets Injected Into Vitiated and Nonvitiated Crossflows

Analysis of the CARS data has been completed. Three premixed, natural gas jets were investigated. The jets investigated were two jets with momentum flux ratios of eight, at equivalence ratios of 0.9 and 3, and one jet with a momentum flux ratio of three with an equivalence ration of 0.9.The dual pump CARS system was operated remotely with LabView. The LabView program incorporated Picard Shutters, six translational stages, and an Andor CCD camera used to collect the CARS data at the streamwise midplane of the reacting jet and it's trajectory. Prior to each test, the CARS signal strength was optimized in the reference leg by turning the high precision optical mount, verifying high N_2 CARS signal on the CCD camera. This procedure was done with no argon gas flowing through the reference leg. The N_2 in air served for verifying CARS signal strength. After the CARS signal was optimized in the reference leg, the CARS signal and strength was verified at the four corners of the windowed combustor. The translational stages were programmed to move the three laser beams in a grid pattern a 140 points. At each point 300 laser shots were collected, along with 50 background. For each spatial point, 30 seconds of steady state data was collected.

The CARS spectra was processed using Sandia CARSFT code. Temperature and species concentration data is determined by the Sandia CARSFT code by comparing experiemental data with theory and performing a least square fit. This was accomplished by allowing the CARSFT program to freely vary parameters like temperature, H_2/N_2 concentraion ratios, horizontal and vertical shifts, and several other input parameters needed to calculate the spectra. The temperature for each spectrum was obtained by analyzing the N_2 part of the spectrum. The H_2 concentration was then determined by fixing the temperature at the value previously determined from the N_2 spectrum and re-processing the parts of the spectrum where H_2 was present. The spectra were processed in a batch mode.

Of the thousands of CARS spectra collected (around 40000), the H_2 CARS signal was only observed for the richer jet cases, $\phi = 3$. When H2 was present, however, the signal was quite strong as shown in Fig. 7.5. The six individual peaks to the left of the nitrogen CARS signal is the hydrogen CARS signal. The five peaks correspond (from left to right) to the Q(6), Q(5), Q(4), Q(3), Q(2) and Q(1) transitions. In this study the H_2 molecule is used to indidcate zones of high reactivity.

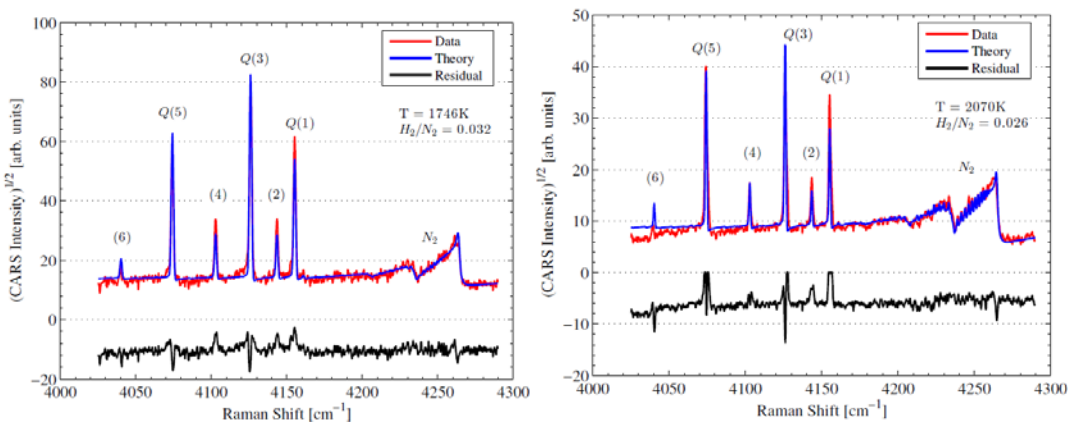

Figure 7.5 Comparison between experimental and theoretical dual-pump CARS spectra for various spatial positions with H_2 CARS signal present.

From the CARS spectra a time averaged temperature contour map was generated for the reacting jet case of J=8 $\phi = 0.9$ at the mid-plane of the reacting jet trajectory, as shown in Fig. 7.6. Due to the window damage, only 122 out of the 140 spatial location could be processed. So, the holes in the temperature plot indicates the regions where the obtained signal could not be processed. The black line indicates the jet centerline obtained from the Holdeman correlation and it approximately tracks the core of the jet. The colder jet core penetrates into the SCZ before reacting, as indicated by the blue region below the nozzle exit. The highest temperature is evident just downstream of the jet core within the near wake region of the jet. In the previous sections the high repetition rate OH-PLIF and PIV measurements have already indicated that the near wake region of the jet helps stabilizing the reaction zone. The highest temperature region within the same spatial region further confirms the observation. The standard deviation is significantly high with the core of the jet which could be attributed to the in plane flapping of the jet flame. This phenomena was tracked in the HRR OH-PLIF imaging of the jet flame.

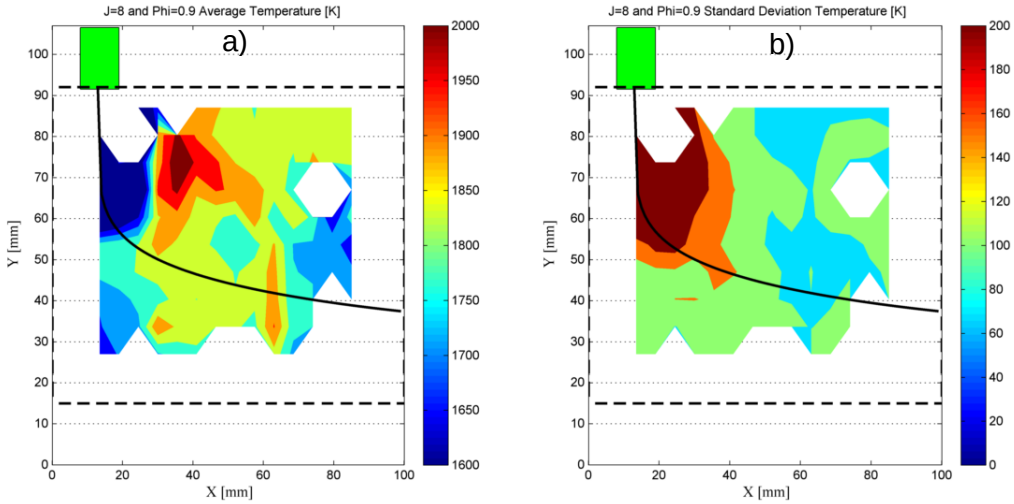

Figure 7.6 a) Average temperature contour plot and b) standard deviation in the measured temperature for the reacting jet case of J = 8;ϕ_{jet} = 0.9.

Figure 7.7, shows several histograms from spatial locations near the zone of influence of the jet. The spatial locations are indicated in the temperature contour plot by black and white circles. As shown in Fig. 7.7, some of the spatial points have a unimodal behavior, but majority of the points near the jet zone of influence have a broad variation in temperature.

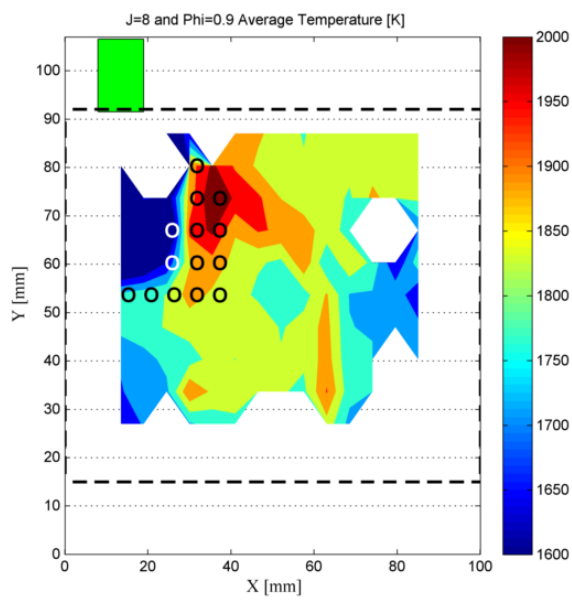

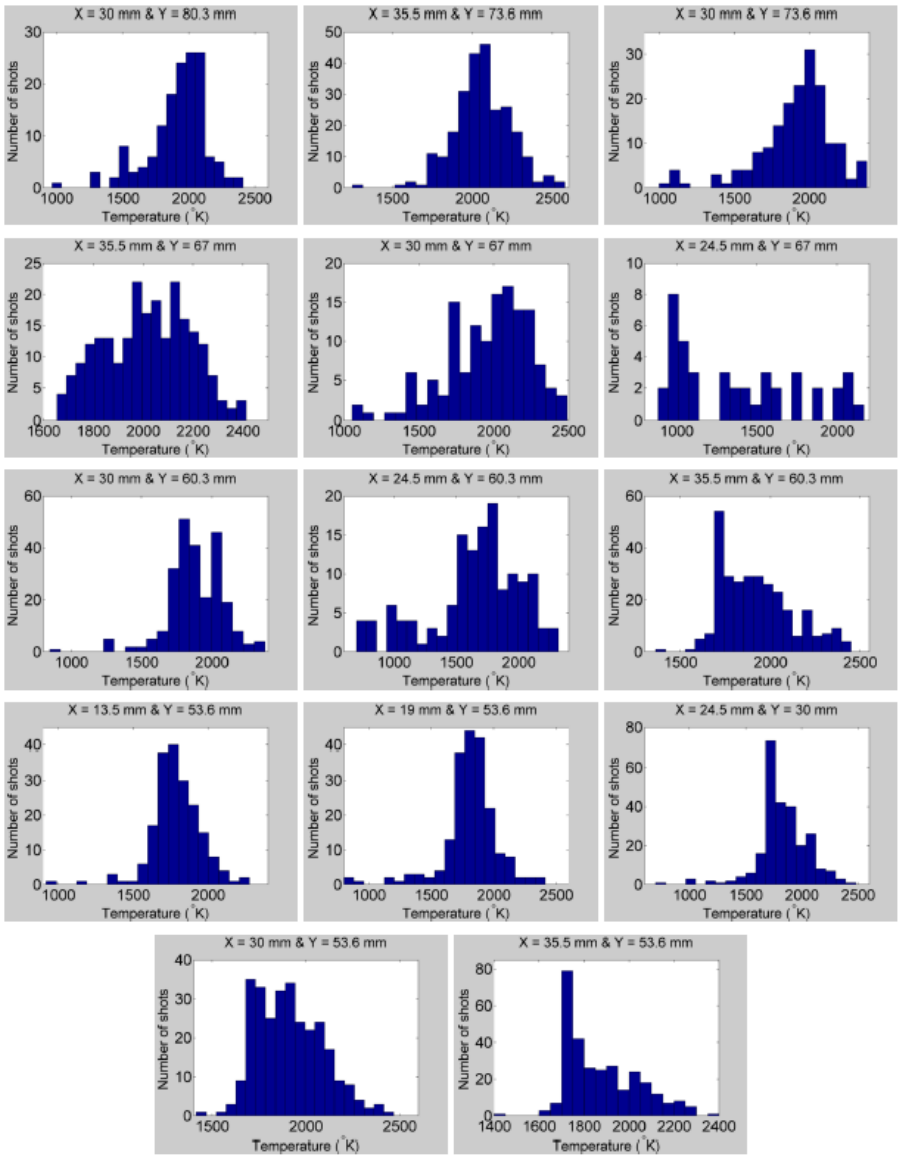

Figure 7.7 Temperature histograms extracted from the locations marked is circles on average temperature plots for reacting jet case of J=8;ϕ_{jet} = 0.9.

The streamwise variation of the average temperature and the temperature standard deviation across vertical lines (Y = constant) are shown in Fig. 7.8. The temperature levels off further downstream or away from the zone of influence of the reacting jet. The standard deviation also narrows to within 100 K further downstream away from the jet. The temperature reaches a steady state value roughly 4 nozzle exit diameters or 40 mm downstream the nozzle exit. For this lean jet condition, complete combustion occurs within a few nozzle diameters.

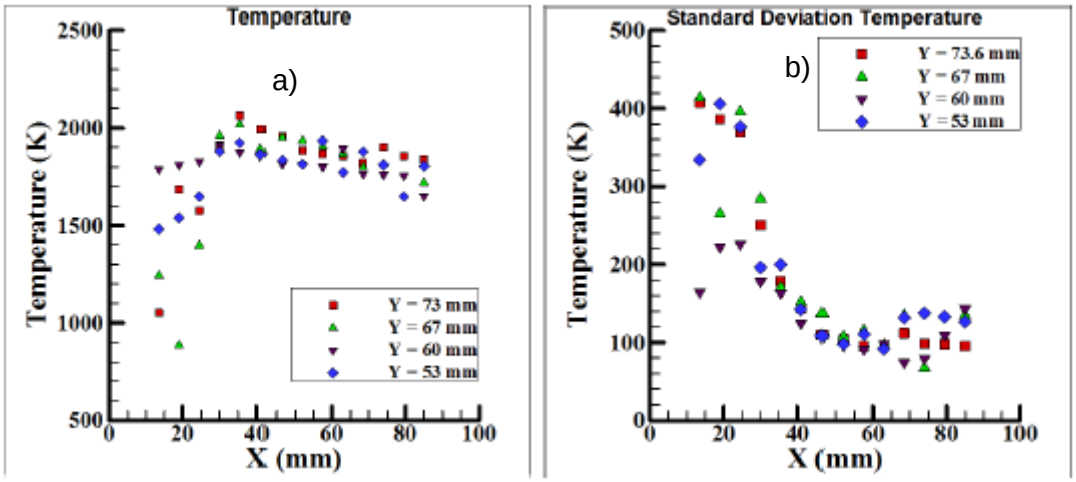

Figure 7.8 The streamwise variation of a) average temperature and b) temperature standard deviation extracted from the four y-locations for reacting jet case of J=8;ϕ_{jet} = 0.9.

It is looking more and more unlikely that we will be able to perform femtosecond CARS in the high-pressure test rig before the current three-year project period ends; the ultrafast laser system that we use for the femtosecond CARS requires much better temperature and humidity control than is available in the Laser Laboratory at the High-Pressure Laboratory. We recently were granted permission by Purdue Univeristy to begin the detailed design of a new gas turbine test cell complex with five hardened test cells and with a 2000 square foot laser laboratory adjacent to these test cells; the new laser laboratory will have excellent temperature and humidity control.

In view of the anticipated two-year time frame for the design and construction of the new test facility, we would like to formally request that we be granted permission to use nanosecond CARS instead of femtosecond CARS for Tasks 7.1 and 7.2.

SubTask 7.2: CARS Measurements of Temperature and Species for HHC Gas Jets Injected Into Vitiated and Nonvitiated Crossflows

This subtask has not yet been started.

Conclusion

Secondary injection of the fuel, also referred to as staged combustion, is being studied by gas turbine manufacturers as a means of increasing the power output of the gas turbine systems with minimal contribution to NOx emission. A reacting jet issuing into a swirling, vitiated cross flow operating at gas turbine relevant conditions was investigated as a means of secondary injection.

An optically accessible test rig was designed and fabricated for the study of a staged combustion system at gas turbine relevant conditions.Three laser based diagnostic techniques were used to study the structure and dynamics of the reacting jet in a vitiated crossflow. HRR particle imaging velocimetry (PIV) and planar laser-induced fluorescence (PLIF) were used to measure the velocity field and visualize fuel/air mixing and combustion at data rates of 5-10 kHz. Dual pump Coherent anti-Stokes Raman scattering (DP-CARS) was employed for temperature measurements at a repetition rate of 10 Hz. Two different fuels, viz. natural gas (NG), as baseline, and a high-hydrogen-content (HHC) fuels were investigated. Accurate high-resolution spatial and temporal measurements of the resulting turbulent flame structure significantly improved our understanding of the complex processes of fuel/air mixing and turbulence-chemistry interaction with attendant impact on operability when using HHC fuels. Additionally, a unique experimental capability forcing the representative crossflow into a stationary, oscillatory condition to simulate an unstable condition, was designed and fabricated. A proven means for producing combustion dynamics has been used for performing combustion instability studies on a reacting jet in crossflow configuration. The method used to provide an unsteady flowfield into which the transverse jet is injected is a unique and novel approach that permits elevated temperature and pressure conditions. A model dump combustor is used to generate and sustain an acoustically oscillating vitiated flow that serves as the crossflow for transverse jet injection studies. A fully optically accessible combustor test section affords full access surrounding the point of jet injection. High speed 10 kHz planar measurements OH PLIF and high frequency 180 kHz wall pressure measurements were performed on the injected reacting J = 6 transverse jet and surrounding flowfield, respectively, under simulated unstable conditions.

There have been several studies involving flow velocity measurements of a reacting jet in crossflow reported in literature but the unique aspect of this work is a detailed study on the flow structure and dynamics of wake of the jet and its influence on stabilizing a reaction zone. The PIV measurements clearly indicate the influence of the swirl component in the crossflow on the jet. The time resolved velocity field measurements successfully captured the wake structure. The wake vortices were observed clearly at the z = 5 mm and 15 mm planes for the J =3 cases and at z = 5 mm, 15 mm and 25 mm planes for the J = 8 cases, indicating a larger wake and longer upright wake vortices for the higher momentum flux ratio. The measured velocity field was further analyzed to extract the wake vortex shedding frequency for the RJICFs. The main finding from this analysis was the range of wake Strouhal number computed for the RJICFs were found to be at least 25% less than the wake Strouhal number of a cylindrical bluff body under similar crossflow Reynolds number. The OH-PLIF based flame front imaging provides strong evidence of a stabilized reaction zone within the wake field. Thus, the wake Strouhal numbers are useful in understanding the rate of mixing of the fuel jet with the high temperature vitiated crossflow within the wake of the jet. However, we need to understand the impact of the third component of velocity in this analysis before deriving to any further conclusions. Due to limited

optical access to the windowed combustor stereo-PIV based measurement to obtain all three components of velocity could not be applied.

In order to quantify the turbulence-chemistry interaction high repetition rate simultaneous PIV/OH-PLIF experiments were performed at these operating conditions. Simultaneous 2D PIV and OH-PLIF measurements were performed at a repetition rate of 10 kHz. The measurements were performed at 3 different planes along the cross-section of the jet at planes z = 5, 10 and 15 mm away from the nozzle exit. Based on the knowledge gained from the HRR PIV and OH-PLIF experiments it was established that the wake of the jet provides a stable reaction zone and thus justifying the focus of the current study The PIV measurements clearly indicate the influence of swirling crossflow on the reacting jet. Multi plane velocity measurement gave an estimate of the extent of penetration of the jet based on the size and vorticity magnitude of the wake structure. As expected J = 8 case had a deeper penetration into the flow field as compared to J = 3 case. A 3 dimensional wake vortex structure was generated out of the time averaged velocity data at three different planes for J = 8 case that gives an approximate size of the upright wake vortices. The flow structure is largest at z = 5 mm and the size decreases further away from the nozzle exit. It can be seen that the highest PLIF intensity region lies between the two wake structures indicating the influence of wake structure on flame stabilization within the wake of the jet. The instantaneous PLIF images were processed to generate an edge of the reaction front by a MATLAB based edge detection algorithm. The instantaneous sequences of velocity vectors overlaid on top of edge of the reaction zone and various other flow variables provided significant insight into the physics behind the transients associated in an RJICF. The wake structure distorted and elongated the reaction front eventually puncturing the flame front causing local extinction due to extremely high rates of scalar dissipation. A combined influence of high vorticity magnitude and the planar compressive strain rate were identified to be critical in causing such an event of flame break-up.

For the combustion dynamics of a fuel jet injected into a vitiated oscillatory crossflow, the structure and dynamics of a J = 6 60/40 H_2/N_2 jet display strong temporal coherence with the crossflow flowfield ~200 Hz and ~400 Hz velocity fluctuations. Results from dynamic mode decomposition show the cross sections of the jet flame front at planes z = 4.8 mm and 14.8 mm to ebb and flow in the crossflow streamwise direction. On account of the large time scales of the crossflow ~200 Hz and ~400 Hz frequencies relative to the jet exit fluid velocity, this suggests the jet trajectory is a function of the crossflow frequency period, e.g. ¼ period following a pressure rarefaction at the point of jet injection for the crossflow ~200 Hz frequency, the crossflow velocity is instantaneoulsy a maximum and leads to decreased jet penetration. This is also supported by data from the cross sections of the jet trajectory: (i) a time dependent jet trajectory synchronized with the crossflow ~200 Hz velocity oscillations and (ii) the crossflow ~400 Hz velocity pertubations oscillating the initial jet shear layer region in the crossflow streamwise direction within 1-2 jet diameters of the jet exit. The cross section of the jet flame trajectory also shows a changing windward and leeward flame anchor location that is a function of the crossflow acoustic cycle, which contrasts an average of the OH PLIF images.

From the DP-CARS measurement of the temperature field of the RJICF it was discovered that the temperature was highest behind the jet or in the wake of the jet and the highest variation in temperature occurred right underneath the nozzle exit or the zone of inuence of the reacting jet. The near wake region of the jet has the highest temperature within the flow field which also corresponds to the region of high OH-PLIF intensity.

RJICF also serves as an important test case for the development of numerical methods for

turbulent reacting flow fields typical of gas turbine combustors. Temporally resolved measurements similar to the one studied in this work will provide significantly improved understanding of the complex processes of fuel/air mixing which is critical in the development of high fidelity turbulence-chemistry interaction models.

References

Bandaru RV and Turns SR (2000) Turbulent jet flames in a crossflow: effects of some jet, crossflow, and pilot-flame parameters on emissions. Comb. Flame 121(1-2):137-151.

Böhm B, Heeger C, Boxx I, Meier W, Dreizler A (2009) Time-resolved conditional flow field statistics in extinguishing turbulent opposed jet flames using simultaneous high speed PIV/OH-PLIF. Proc. Combust. Inst. 32(2):1647–1654.

Boxx I, Carter C, Stohr M, Meier W (2013) Study of the mechanism for flame stabilization in gas turbine model combustors using kHz laser diagnostics. Exp Fluids 54:1532.

Boxx I, Arndt CM, Carter C, Meier W (2012) High-speed laser diagnostics for the study of flame dynamics in a lean premixed gas turbine model combustor. Exp Fluids 52(3):555-567.

Chan W L, Kolla H, Chen J H, Ihme M (2014) Assessment of model assumptions and budget terms of the unsteady flamelet equations for a turbulent reacting jet-in-cross-flow. Comb.Flame 161(10):2601-2613.

Cheng R, Yegian D, Miyasato M, Samuelsen G, Benson CE, Pellizzari R, Loftus P (2000) Scaling and development of low-swirl burners for low-emission furnaces and boilers. Proc. of Combust. Inst. 28:1305-1313.

Cortelezzi L and Karagozian AR (2001) On the formation of the counter-rotating vortex pair in transverse jets. J. Fluid Mech. 446: 347 – 373.

Denev JA, Fröhlich F, Bockhorn H (2009) Large eddy simulation of a swirling transverse jet into a crossflow with investigation of scalar transport. Phys. of Fluids 21(1).

Fric TF., Roshko A (1994) Vortical structure in the wake of a transverse jet. J. Fluid Mech. 279:1-47.

Gollahalli SR and Nanjundappa B (1995) Burner wake stabilized gas jet flames in cross-flow. Comb. Science and Tech. 109:327-346.

Grout RW, Gruber A, Yoo CS, Chen JH (2011) Direct Numerical Simulation of flame stabilization downstream of a transverse fuel jet in cross-flow. Proc. of the Comb. Ins. 33:1629–1637.

Hasselbrink EF and Mungal MG (2001) Transverse jets and jet flames, Part-1: Scaling laws for strong transverse jets. J. Fluid Mech. 443:1-25.

Hasselbrink EF and Mungal MG (2001) Transverse jets and jet flames. Part 2. Velocity and OH field imaging. J. Fluid Mech. 443:27–68.

Huang RF and Chang JM (1994) Coherent structure in a combusting jet in crossflow. AIAA Journal 32(6):1120–1125.

Kolla H, Grout RW, Gruber A, Chen (2012) Mechanisms of flame stabilization and blow-off in a reacting turbulent hydrogen jet in cross-flow. Comb.Flame 159, 2755-2766.

Lamont W, Roa M, Meyer S, Lucht RP (2012) Emission measurements and CH* chemiluminescence of a reactive jet in a vitiated crossflow. J. Eng. Gas Turbines Power 134(8).

Lieuwen TC and Yang V (2013) Gas turbine emissions. Cambridge University Press, 1st edition.

Lucht R.P. Three-laser coherent anti-Stokes Raman scattering measurements of two species. Optics letters, 12(2):78-80, 1987.

Margason RJ (1993) Fifty years of jet in cross flow research In AGARD, Computational and Experimental Assessment of Jets in Cross Flow. SEE N94-28003 07-34: 1-41.

M'Closkey RT, King J, Cortelezzi L, Karagozian AR (2002) The Actively Controlled Jet in Crossflow, J. Fluid Mech. 452:325-335.

Megerian, S., Davitian, J., L.S., DE B. Alves, Karagozian, A.R.. Transverse-Jet Shear-Layer Instabilities. Part 1. Experimental Studies. Journal of Fluid Mechanics. Vol 593. 2007.

Moussa ZM, Trischka JW, Eskinazi S. (1977) The near field in the mixing of a round jet with a cross-stream. J. Fluid Mech. 80:49-80.

Muppidi S and Mahesh K. (2007) Direct numerical simulation of round turbulent jets in crossflow. J. Fluid Mech. 574:59–84.

New TH, Lim TT, Luo SC (2006) Effects of jet velocity profiles on a round jet in cross-flow. Exp. Fluids 40:859 – 875.

Saravanamuttoo HIH, Rogers GFC, Cohen H., and Straznicky PV (2009) Gas turbine theory. Pearson Education Ltd., 6th edition.

Scarano F and Poelma C (2009) Three-dimensional vorticity patterns of cylinder wakes. Exp Fluids 47:69-83.

Su LK and Mungal MG (2004) Simultaneous measurements of velocity and scalar fields: application in crossflowing jets and lifted jet diffusion flames. J. Fluid Mech. 513:1–45.

Schmid, P.J. Dynamic Mode Decomposition of Numerical and Experimental Data. Journal of Fluid Mechanics. Vol 656. 2010.

Sullivan R, Benjamin W, Noble DR, Seitzman JM, Lieuwen T (2013) Unsteady flame-wall interactions in a reacting jet injected into a vitiated cross-flow. Proc. of the Comb. Ins. 34:3203–3210.

Sullivan R, Benjamin W, Noble DR, Seitzman JM, Lieuwen T (2014) Time-averaged characteristics of a reacting fuel jet in vitiated cross-flow.Comb.Flame 161 (7):1792-1803.

Steinberg AM, Sadanandan R, Dem C, Kutne P, Meier W (2013) Structure and stabilization of hydrogen jet flames in cross-flows. Proc. Combust. Inst.34(1):1499–1507.

Stohr M, Sadanandan R, Meier W (2011) Phase-resolved characterization of vortex-flame interaction in a turbulent swirl flame. Exp Fluids 51:1153-1167.

Thariyan M.P., Ananthanarayanan V., Bhuiyan A.H., Naik S.V., Gore J.P., and Lucht R.P. Dual-pump CARS temperature and major species concentration measurements in counter-flow methane flames using narrowband pump and broadband Stokes lasers. Comb.Flame, 2010

Westerweel J, Elsinga G, Adrian RJ (2013) Particle image velocimetry for complex and turbulent flows. Annual Rev. Fluid Mech 45:409-436.

Wooler PT (1969) Flow of a circular jet into a cross flow. Journal of Aircraft 6 (3): 283-284.

Yu, Y.C., Sisco, J.C., Sankaran, V., Anderson, W.E., Effects of Mean Flow, Entropy Waves, and Boundary Conditions on Longituindal Combustion Instability. Combustion Science and Technology. Vol 182. 2010.

Table 1: FY 2012 Project Milestone Log

FY 2012 Milestone	Planned Completion Date	Actual Completion Date	Verification Method	Milestone Status, Comments
M1Y1: Development and modification of Project Management Plan (PMP) in collaboration with NETL Project Manager.	1/15/2012	1/15/2012	The PMP document to will be delivered electronically to the NETL Project Manager.	Completed
M2Y1: Modification of the test rig for the reacting jet in crossflow (RJIC) studies. Design and fabrication of test rig components for the RJIC study. The test rig that has been used for previous secondary jet injection studies will be modified for the DOE jet in crossflow studies.	3/1/2012	3/31/2012	The Project Manager will be informed of the progress of the design and fabrication process. The fabricated parts will be photographed. The data from the first operational tests of the modified rig will be communicated to the NETL Project Manager.	Completed
M3Y1: Development of test matrix for FY2012 experiments. A matrix of test operating conditions including but not limited to pressure, composition of the jet fluid, vitiated versus non-vitiated crossflow, temperature of the crossflow, jet-to-crossflow momentum ratio J, and jet-to-crossflow velocity ratio R will be developed.	3/1/2012		The test matrix will be presented during a webex meeting with Purdue and NETL personnel.	Completed
M4Y1: Development of PIV particle seeder for the high-pressure test rig. A PIV particle seeder capable of injecting a stream of particles into the high-pressure test rig will be designed and	6/30/2012		The design of the seeder will be discussed on an ongoing basis with NETL personnel. The fabrication process will be documented with photographs and	Completed.

fabricated. It will be tested under nonreacting conditions (heated air flow only) in the high-pressure test rig.			machining drawings.	
M5Y1: Successful implementation of high-data-rate OH PLIF in the high-pressure combustion test rig.*	9/30/2012		The implementation of high-data-rate OH PLIF will be verified by the delivery of high-data-rate images to the Project Manager.	Completed

Table 2: FY 2013 Project Milestone Log

FY 2013 Milestone	Planned Completion Date	Verification Method	Milestone Status
M1Y2: Successful implementation of high-data-rate PIV in the high-pressure combustion test rig.	12/31/2012	The implementation of high-data-rate PIV will be verified within a report documenting the results.	Completed
M2Y2: Completion of high-data-rate OH PLIF studies for natural gas jets.	6/30/2013	The completion of the high-data-rate OH PLIF studies for natural gas jets will be verified within a report documenting the results.	Completed
M3Y2: Completion of high-data-rate OH PLIF studies for HHC fuel jets.	6/30/2013	The completion of the high-data-rate OH PLIF studies for HHC fuel jets will be verified within a report documenting the results.	Completed
M4Y2: Completion of high-data-rate PIV studies for natural gas jets.	9/30/2013	The completion of the high-data-rate PIV studies for natural gas jets will be verified within a report documenting the results.	Completed
M5Y2: Completion of high-data-rate PIV studies for HHC fuel jets. *	9/30/2013	The completion of the high-data-rate PIV studies for HHC fuel jets will be verified	Completed

		within a report documenting the results.	
M6Y2: Initiation of combustion dynamics coupling experiments measuring combustion response under simulated unstable conditions.	9/30/2013	The initiation of the combustion dynamics coupling experiments will be verified within a report documenting the results.	Completed

FY 2014 Milestone	Planned Completion Date	Verification Method	Milestone Status
M1Y3: Successful implementation of simultaneous high-data-rate PIV and OH PLIF in the high-pressure combustion test rig.	12/31/2013	The implementation of simultaneous high-data-rate PIV and OH PLIF will be verified within a report documenting the results.	Completed
M2Y3: Completion of simultaneous high-data-rate PIV and OH PLIF studies for natural gas jets.	6/30/2014	The completion of the simultaneous high-data-rate PIV and OH PLIF studies for natural gas jets will be verified within a report documenting the results.	Completed
M3Y3: Completion of simultaneous high-data-rate PIV and OH PLIF studies for HHC fuel jets.	6/30/2014	The completion of the simultaneous high-data-rate PIV and OH PLIF studies for HHC fuel jets will be verified within a report documenting the results.	Completed
M4Y3: Completion of high-speed simultaneous PIV/OH PLIF studies of combustion dynamic coupling under simulated unstable conditions.	9/30/2014	The completion of the studies of combustion dynamic coupling under simulated unstable conditions will be verified within a report documenting the results.	In Progress
M5Y3: Demonstration of high-data-rate femtosecond CARS temperature measurements in the RJIC test rig.*	9/30/2014	The demonstration of high-data-rate femtosecond CARS temperature measurements	Nanosecond CARS measurements completed.

		will be verified within a report documenting the results.	

***Indicates yearly milestones to be tracked in M1**

3. PRODUCTS

3.1 Publications, conference papers, and presentations

R. P. Lucht, "Advanced Laser Diagnostics for Reactive Mixing Flows", presentation at the 2012 American Institute of Chemical Engineers Annual Meeting, Pittsburgh, PA, 29 October, 2012. (Invited Lecture)

Panda, P., Roa, M., Lucht, R.P., Szedlacsek, P., Laster,W.R., "Structure and dynamics of the wake of a reacting jet injected into a swirling vitiated crossflow," *Experiments in Fluids*, DOI: 10.1007/s00348-014-1885-3 (*Accepted for Publication*).

Panda, P., Roa, M., Lucht, R.P., "Time Resolved Planar Measurements in the wake of a Reacting Jet Injected into a Swirling, Vitiated Crossflow at High Pressure", *Journal of Power and Propulsion* (In Preparation)

Panda, P., Roa, M., Slabaugh, C., Peltier, S., Carter, C., Lucht, R.P., Laster,W.R., "Time resolved planar measurement in the wake of a hydrogen jet injected into a swirling vitiated crossflow," *Combustion and Flame* (In Preparation).

Roa, M., Lamont, W., Panda, P., Lucht, R.P, Szedlacsek, P., Laster,W.R., "High repetition rate OH-PLIF and DP-CARS measurements to investigate a reacting jet injected into a swirling vitiated crossflow," *Combustion and Flame* (In Preparation).

Fugger, C., Anderson, W.,Lucht, R.P., "Model Combustor for Transverse Jet Injection Unsteady Crossflow Forcing Studies and LES validation," *Experiments in Fluids* (In Preparation).

Fugger, C., Anderson, W.,Lucht, R.P., "Structure and Dynamics of a Fuel Jet Injected into a Vitiated Oscillatory Crossflow using High Repetition Rate Optical Diagnostics," *Combustion and Flame* (In Preparation).

3.2 Website(s) or other Internet site(s)

None so far.

3.3 Technologies or techniques

None so far.

3.4 Inventions, patent applications, and/or licenses

None so far.

3.5 Other products

None so far.

4. PARTICIPANTS & OTHER COLLABORATING ORGANIZATIONS

What individuals have worked on the project?

Name:	**Robert P. Lucht**
Project Role:	Principal Investigator
Nearest person month worked:	3

Prof. Lucht is the principal investigator.

Funding Support:	
Collaborated with individual in foreign country:	No
Country(ies) of foreign collaborator:	N/A
Travelled to foreign country:	No
If traveled to foreign country(ies), duration of stay:	N/A

Name:	**William E. Anderson**
Project Role:	Co-Principal Investigator
Nearest person month worked:	3

Prof. Anderson is the co-principal investigator.

Funding Support:	
Collaborated with individual in foreign country:	No
Country(ies) of foreign collaborator:	N/A
Travelled to foreign country:	No
If traveled to foreign country(ies), duration of stay:	N/A

Name:	**Mario Roa**
Project Role:	Graduate Student
Nearest person month worked:	3

Mr. Roa is the lead experimentalist on the project. He is chiefly responsible for the high-speed OH PLIF imaging and the CARS measurements.
He is funded this year by Purdue cost sharing funds

Collaborated with individual in foreign country:	No
Country(ies) of foreign collaborator:	N/A
Travelled to foreign country:	No
If traveled to foreign country(ies), duration of stay:	N/A

Name:	**Pratikash Panda**
Project Role:	Graduate Student
Nearest person month worked:	3

Mr. Panda designed the particle seeder. He also performed an extensive literature review and has started work on the development of the test matrix for the reacting jet in crossflow studies.

He has also assisted Mario Roa with the operation of the test rig. He will be principally responsible for the high-speed PIV measurements.
He is funded half-time on the UTSR project and is also supported half-time on a project funded by NASA Glenn.

Collaborated with individual in foreign country:	No
Country(ies) of foreign collaborator:	N/A
Travelled to foreign country:	No
If traveled to foreign country(ies), duration of stay:	N/A

Name:	**Chris Fugger**
Project Role:	Graduate Student
Nearest person month worked:	3

Mr. Fugger is working on the combustion instability measurements.
He is supported full-time on the UTSR project.

Collaborated with individual in foreign country:	No
Country(ies) of foreign collaborator:	N/A
Travelled to foreign country:	No
If traveled to foreign country(ies), duration of stay:	N/A

Name:	**Sameer Naik**
Project Role:	Visiting Assistant Professor
Nearest person month worked:	3

Dr. Naik is assisting with the development of the laser diagnostics.
He is supported 20% on the DOE UTSR project, he is also supported by a teaching assignment, and by projects with Cummins, with the Office of Basic Energy Sciences, US Dept. of Energy, and with NASA Glenn.

Collaborated with individual in foreign country:	No
Country(ies) of foreign collaborator:	N/A
Travelled to foreign country:	No
If traveled to foreign country(ies), duration of stay:	N/A

What other organizations have been involved as partners?
Organization Name: Siemens Power Systems
Location of Organization: Orlando, Florida
Partner's contribution to the project (identify one or more)

- Financial support: Siemens Energy is funding work on the same test rig that we are using for the DOE UTSR work. The test rig was developed with funds from Siemens Power Systems. We are testing some proprietary nozzle designs for Siemens.
- In-kind support: None.
- Facilities: None.

- Collaborative research: We collaborate on papers resulting from analysis of results from our test rig.
- Personnel exchanges: Project meetings and teleconferences. No long-term personnel exchange.

Organization Name: Professor Venkat Raman, University of Texas at Austin, Department of Aerospace Engineering and Engineering Mechanics
Location of Organization: Austin, Texas
Partner's contribution to the project (identify one or more)

- Financial support: None
- In-kind support: None.
- Facilities: None.
- Collaborative research: Prof. Raman and a PhD will be working on a CFD model of our experiments with the extended nozzle. He will be comparing his model results with our data for the Φ=3.0, J=8 and Φ=3.0, J=3 cases. Siemens Energy has been apprised of and approves the collaborative research interaction. The first step will be sending CAD files of our test rig to Prof. Raman.
- Personnel exchanges: Project meetings and teleconferences. No long-term personnel exchange.

5. IMPACT

What is the impact on the development of the principal discipline(s) of the project?

The primary objective of the proposed work is to investigate the structure of the reacting flow field for jets injected into a subsonic crossflow. The jet fluid will consist of a fuel species such as natural gas or a high-hydrogen-content (HHC) fuel. In some cases, diluents such as CO_2 or will be mixed with the fuel in the jet fluid. The jet in crossflow study has both practical applications and serves as an important test case for the development of numerical methods for turbulent reacting flow fields typical of gas turbine combustors. Secondary injection of the fuel, also referred to as distributed combustion, is being studied by gas turbine manufacturers as a means of reducing NOx emissions while increasing the power output of the gas turbine systems. Numerical simulation of the reacting jet in crossflow is challenging because of the complex vortical structure of the flow field. However, it is a tractable problem and the flow field can be investigated in detail using laser diagnostics, including the latest wave of high-data-rate diagnostic techniques.

High-speed particle imaging velocimetry (PIV) and planar laser-induced fluorescence (PLIF) will be used to visualize fuel/air mixing and combustion at data rates of 5-10 kHz. "1 kHz" coherent anti-Stokes Raman scattering (CARS) will be employed for temperature measurements using femtosecond lasers. Three different fuels, viz. natural gas (NG), as baseline, and two high-hydrogen-content (HHC) fuels will be investigated. Accurate high-resolution spatial and temporal measurements of the resulting turbulent flame structure will provide significantly improved understanding of the complex processes of fuel/air mixing and turbulence-chemistry interaction with attendant impact on operability when using HHC fuels. The resulting benchmark quality data sets will include comprehensive, accurate measurements of mean and fluctuating components of velocity, temperature, and species at high pressure and with crossflow conditions representative of modern gas turbine engines.

The results of this research will help technologists gain deeper scientific insight which in turn will improve the technology and design development process capabilities for developing the promising "distributed or late-lean" combustion technology for the next-generation of higher-efficiency, ultra-clean engines burning HHC fuels.

The results of this research will be used by combustion modeling community to validate next-generation combustion models with emphasis on complex turbulent vortical structure including modern advanced models on chemical kinetics, turbulence and turbulence/chemistry interaction.

What is the impact on other disciplines?

The results of this research may have impact on other disciplines through the demonstration of advanced laser diagnostic methods for measurements in reacting flows.

What is the impact on the development of human resources?

This project represents a tremendous training opportunity for graduate and undergraduate students who are interested in the gas turbine field. Their working experience with sophisticated laser diagnostics and with a practical, high-pressure combustion test rig will be of great interest to potential employers.

What is the impact on physical, institutional, and information resources that form infrastructure?

This project will have a very positive impact on the further development of the infrastructure for high-pressure combustion rig testing at Purdue University. Ours is one of the few facilities in the nation equipped and able to perform such testing. It is very expensive and requires significant infrastructure and experience to perform in a safe and productive fashion. The demonstration of the high-data-rate diagnostic techniques, a principal goal of the UTSR project, is a major step forward in the infrastructure development at our facility.

What is the impact on technology transfer?

The impact on technology transfer is likely to be greatest in terms of producing talented graduate students to work in the gas turbine industry.

What is the impact on society beyond science and technology?

The long-term goal of the project is to enhance fundamental understanding of the combustion process so that gas turbine power systems are more efficient and produce lower levels of pollutants.

What dollar amount of the award's budget is being spent in foreign country(ies)?

None.

6. CHANGES/PROBLEMS

As discussed in Section 7, we will not be able to perform the femtosecond CARS measurements discussed in the PMP. We did perform nanosecond CARS measurements in the RJIC test rig.

7. SPECIAL REPORTING REQUIREMENTS

None.

8. BUDGETARY INFORMATION

Baseline Cost Plan	**FY2014**							
	Q1		**Q2**		**Q3**		**Q4**	
	Q1	Cumulative	Q2	Cumulative	Q3	Cumulative	Q4	Cumulative
Federal	$19,342	$19,342	$19,342	$38,684	$19,343	$58,027	$19,343	$77,370
Recipient	$11,628	$11,628	$11,628	$23,256	$11,628	$34,884	$11,628	$46,512
Total	$30,970	$30,970	$30,970	$61,940	$30,971	$92,911	$30,971	$123,882
Actual Costs								
Federal	$29,587	$29,587	$33,895	$63,482	$10,732	$74,214	$3,156	$77,370
Recipient	$17,203	$17,203	$14,732	$31,934	$2,212	$34,146	$12,366	$46,512
Total	$46,789	$46,789	$48,627	$95,416	$12,944	$108,360	$15,522	$123,882
Variance								
Federal	($10,245)	($10,245)	($14,553)	($24,798)	$8,611	($16,187)	$16,187	$0
Recipient	($5,575)	($5,575)	($3,104)	($8,678)	$9,416	$738	($738)	($0)
Total	($15,819)	($15,819)	($17,657)	($33,476)	$18,027	($15,449)	$15,449	$0